Eindhoven University of Technology
Department of Applied Physics
Science and Technology of Nuclear Fusion

ECE for NTM control on ITER

Hugo van den Brand

February 2012 Fusion

Under the supervision of:
dr. E. Westerhof (FOM Institute Differ – Dutch Institute for Fundamental Energy Research)
prof. dr. N.J. Lopes Cardozo (Eindhoven University of Technology)

Abstract

The technical viability of fusion power, to be demonstrated with the ITER tokamak, requires a prevention of core temperature degrading instabilities, such as the Neoclassical Tearing Mode (NTM). NTMs are global magnetic perturbations that result in reconnection of magnetic field lines. This forms a so-called magnetic island, characterized by an island width w. NTMs are a meta stable instability that require a seed island to form a rotating magnetic island. Using Electron Cyclotron Current Drive (ECCD) the current deficiency that drives the instability can be counteracted. In this work, the role ECE could play in an NTM control on ITER loop is investigated. This is addressed by first deriving the requirements for NTM control on the basis of a combined model for island growth and rotation. Secondly, the detection capabilities of ECE are compared with these requirements.

In this work, the control objective is to achieve full suppression of NTMs using ECCD before the mode locks, i.e. stops rotating. For a locked mode, suppression cannot be guaranteed in all situations. Using a combined model for island growth and rotation, the spatial accuracy and the maximum allowed latency between the seeding of the mode and the start of the stabilizing ECCD are determined. Based on the derivation, it can be concluded that the detection of the island location within the determined accuracy is crucial for NTM control.

Using the NOn-Thermal ECE Code (NOTEC), ECE from the ITER plasma is simulated, using a realistic temperature perturbation from the magnetic island. ECE is both simulated for the foreseen equatorial ECE diagnostic and for an ECE diagnostic looking along the line-of-sight of the ECCD launcher. Based on the accuracy requirements, ECE channel layouts are determined, which are used in assessing the detection latency. The detection latency remains below 500 ms for the equatorial ECE and below 1 s for the line-of-sight ECE system. Detection capabilities are limited for larger islands, due to a decreased anti-correlation resulting from the detection of the flattened temperature profile inside the island.

In conclusion, with a proper choice of channel layout, an ECE diagnostic could serve as a timely and accurate sensor for island location in the ECE spectrum.

Contents

1. Introduction

As a result of an increasing and increasingly prosperous world population, future energy demands will be higher than ever before.[1] Depletion of fossil fuels and their inherent effect on the environment call for different means of energy production.

Nuclear fusion of small nuclei, like hydrogen, into larger nuclei, like helium, could fulfill a large part of mankind's energy needs. The temperature, density and energy confinement required to make fusion viable for energy production, related to each other by the Lawson criterion[2], renders a plasma an inescapable feature of today's promising fusion concepts.

A tokamak confines the fusion plasma to a torus using a toroidal magnetic field and current along the plasma loop. The toroidal current induces a magnetic field in poloidal direction, circling the toroidal field. The resulting helical magnetic field confines the fusion plasma to nested surfaces on which the temperature and density is constant. The transport between the nested surfaces is small, creating an ideal situation to sustain a high core temperature of 100 million kelvin required for sufficient fusion yield.[3]

Neoclassical transport theory describes the bootstrap current arising from a radial pressure gradient, a lack of which drives the Neoclassical Tearing Mode (NTM) instability. This meta stable instability is induced by a small perturbation of the magnetic field, provided by other instabilities.[4] An NTM forces a reconnection of the field into a magnetic island in which radial transport is increased, thus decreasing the pressure gradient and consequently reducing the bootstrap current. This decreases the local magnetic field and thereby reinforces the growth of the mode.

An NTM has two negative effects on fusion plasmas. Firstly, the increased radial transport in the island reduces the core temperature by 15 % to 25 %.[5] Secondly, large islands induce wall currents that slow down the island until it stops rotating, an event known as mode locking. A locked mode grows faster and has a high likelihood of leading to a sudden loss of the entire plasma.[4] This event, a disruption, not only stops the fusion process, but also exerts large forces on the plasma vessel capable of inflicting permanent damage on the tokamak structure.

It is clear that an uncontrolled NTM is a problem for tokamaks and tokamak-based fusion power plants. Fortunately, there is a vast amount of theory and experiments on NTMs and their control. Electron Cyclotron Current Drive (ECCD) has already established itself as the best way

to stabilize a NTM, by compensating the local bootstrap current deficiency. No final decision has been made on the detection diagnostics for NTMs and the control strategy that is to be used. However, several promising diagnostics have been put forward. For instance, there have been reports on the successful real-time detection of NTMs using Electron Cyclotron Emission (ECE).[6][7][8][9]

1.1. Aim of this work

This work focuses on ECE as a diagnostic for NTMs and ECCD as a means to suppress them on ITER, the next generation tokamak that is under construction at Cadarache, France. Suppression by ECCD has been studied extensively and is still the subject of thorough scientific investigation. The attention paid to NTM detection on ITER is however quite limited. The collaboration between the FOM Institute DIFFER and the Eindhoven University of Technology combines expertise on NTM physics, ECE radiation simulation and real-time NTM control expertise. Building on this body of knowledge, this work strives to answer the following question:
What role could ECE play in an NTM control loop on ITER?

To answer this question, the goals of the NTM control loop need to be specified. The ITER design requirements prescribe the stabilization of NTMs using ECCD.[10] Experiments show that the probability of a disruption increases if the rotation of the magnetic island is stopped, a process known as mode locking. Because the NTM could lock in an unfavorable position for ECCD access, it is beneficial to stabilize the mode before it locks. This work focuses on full suppression before locking of the NTM.

NTMs occur at rational flux surfaces, where the helicity of the magnetic field lines is such that they close on themselves. This can be expressed by the rational safety factor $q = \frac{m}{n}$, where m and n are respectively the number of toroidal and poloidal rotations after which a particle travelling along the field line returns to its starting position. The $q = 2/1$ and $q = 3/2$ have the largest influence on the plasma confinement and the $q = 2/1$ is known to cause disruptions.[5] Both NTMs are subject of this study.

In this work, control of 2/1 and 3/2 NTMs using ECE for full suppression using ECCD is investigated. This requires the following sub questions to be answered:

1. What are the current specifications of the ITER ECE and ECCD systems?
2. How can ECE be incorporated in NTM control loops on ITER?
3. What are the requirements for full suppression of NTMs on ITER?
4. Which algorithm could be used to detect magnetic islands in ECE measurements?

5. Are magnetic islands accurately detectable within a sufficiently small time for NTM control?

The NOn-Thermal ECE Code (NOTEC) is used to simulate thermal ECE spectra for an ITER plasma with magnetic islands. This code provides an accurate simulation of the EC wave propagation, the ECE antenna pattern and the EC emission region. Non-thermal ECE routines are not used. Simulations of island growth and island rotation are combined with NOTEC simulations into synthetic ECE measurements.

1.2. Outline

The next chapter starts by summarizing the relevant theory, starting with a short introduction of basic tokamak concepts, followed by the physics of NTMs and ECE, including the expected noise levels. Chapter 3 gives an overview of the ITER ECE and ECCD systems and presents three possible control loops for NTM control on ITER. The NOn Thermal ECE Code (NOTEC) is presented in chapter 4. Requirements for full suppression of NTMs are derived in chapter 5. Island position detection using ECE is shown and compared with the requirements in chapter 6. Conclusions about the viability of ECE for an NTM control loop are the subject of chapter 7. The last chapter provides recommendations for further research.

2. Theory

This chapter summarizes the theory used in this work. First a few basic tokamak concepts are introduced. This is followed by theory on Neoclassical Tearing Modes (NTMs) and Electron Cyclotron Emission (ECE).

2.1. Tokamak concepts

Figure 2.1 shows a tokamak, which consists of a torus shaped fully ionized plasma and a set of magnetic coils. This section introduces a coordinate system and gives an overview of magnetic fields and dimensionless parameters used to describe the plasma.

First of all the toroidal and poloidal angle can be defined. Looking at the vessel from above, the toroidal angle ϕ is the angle between two lines projected on the horizontal plane connecting two points to the vertical axis of rotation. The poloidal angle θ is the angle between two lines connected to the core of the plasma in a cross section which includes the vertical axis. Based on these two angles, the toroidal and poloidal direction can be defined as the direction of increasing toroidal and poloidal angle respectively. The direction of increasing toroidal angle describes a counter-clockwise circle when looking at the the tokamak from above. Taking a poloidal cross section, for which the toroidal angle is constant, the poloidal direction describes a counterclockwise rotation, looking along the toroidal direction. The major radius R is the shortest distance from a point in the plasma to the axis of rotation. The plasma major radius R_0 determines the location of the plasma column center in a poloidal cross section. The equatorial plane is the midplane of the toroidal field coils, which are used to generate a magnetic field in the toroidal direction. Tokamaks exhibit a toroidal symmetry.

The plasma is confined using a magnetic field B_T in toroidal direction and a magnetic field B_p in poloidal direction, created by the toroidal plasma current. At the center of the tokamak, the external coils that create B_T are closer together. This results in a scaling of the magnetic field $B_T \propto \frac{1}{R}$ and allows for the distinction between the low field side ($R > R_0$) and the high field side ($R < R_0$). The toroidal magnetic field B_T has a magnitude of a few tesla at R_0, the poloidal field B_p has a ten times lower field and additional magnetic field used for plasma shaping have

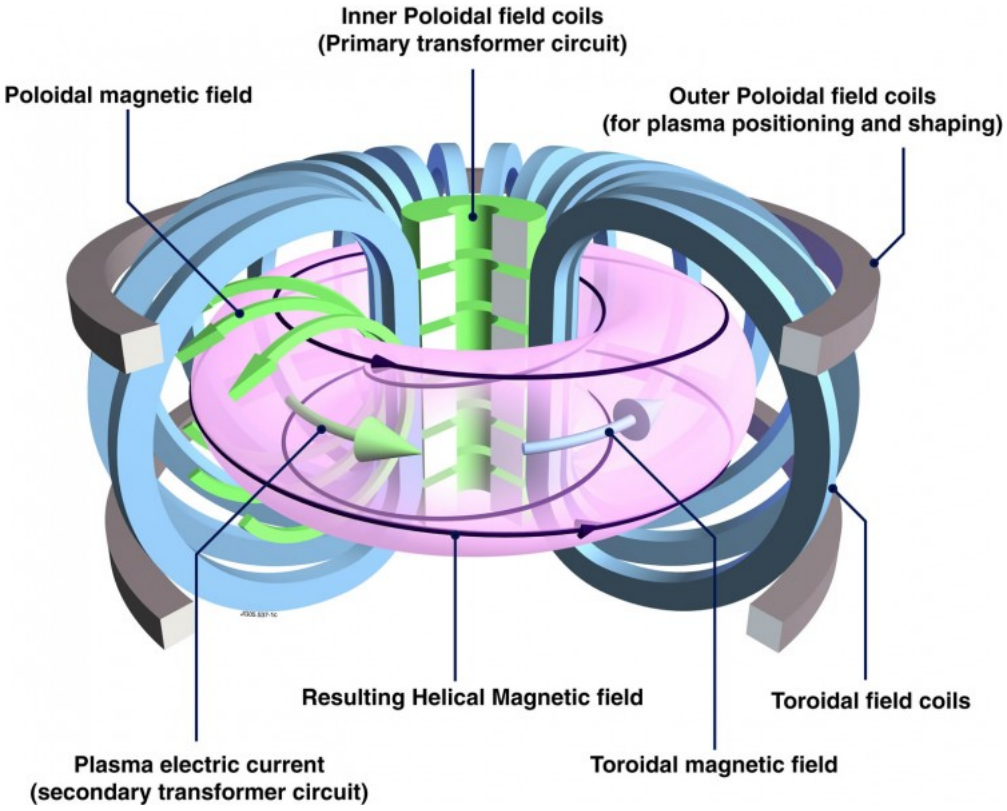

Figure 2.1.: *Schematic picture of a tokamak. The figure shows a plasma, the toroidal field coils and the plasma current, induced by the poloidal field coils. The helical magnetic field, resulting from the toroidal and poloidal fields is indicated by purple arrows. Additional shaping are depicted as well. Picture courtesy of EFDA (http://www.efda.org/).*

even lower magnitudes. Consequently, the toroidal and poloidal magnetic field have the largest influence on the plasma.

From Magnetohydrodynamic (MHD) theory, it can be derived that in steady state the current and magnetic field lines lie on nested flux surfaces in the plasma, on which the temperature and density are constant.[11] Therefore the core plasma equilibrium can be fully defined by a single radial coordinate. For a circular shaped plasma in the poloidal cross section the radial coordinate can be defined independent of the poloidal angle. However, D-shaped plasmas are preferred, thereby requiring a definition that takes into account the change in distance of the flux surface boundary to the plasma center with poloidal angle.

Throughout this work two definitions are used. The first definition is based on the width d of the flux surface in the the equatorial plane, resulting in the minor radius $r = d/2$. The second definition is based on the enclosed flux surface area S in a poloidal cross section. The cylindrical

radius is defined as $r_c = \sqrt{S/\pi}$. The plasma radius in the vertical direction $r_v = \kappa r$ is related to the minor radius by the elongation κ. By approximation of the flux surface by an ellipse with surface $S = \pi r r_v$, the cylindrical radius can be related to the minor radius using $r_c = \sqrt{\kappa} r$.

The dimensionless figure $\beta = \frac{2\mu_0 p}{B^2}$ gives the ratio of plasma pressure divided by magnetic pressure, used to confine the plasma. High β corresponds to higher plasma pressure and therefore higher fusion yields, but also increases the chance of instabilities occurring in the plasma due to larger free energy. The normalized $\beta_N = \frac{\beta[\%] a[\mathrm{m}] B_T[\mathrm{T}]}{I_p[\mathrm{MA}]}$ scales the β with the plasma current I_p in MA, the minor radius of the plasma boundary a in m and the toroidal magnetic field in T.[12]

The safety factor $q = \frac{r B_T}{R_0 B_p}$ expresses the helicity of the magnetic field lines. Rational safety factor values $q = \frac{m}{n}$ indicate the the number of toroidal turns m and the number of poloidal turns n before the helical magnetic field lines close.

2.2. Neoclassical Tearing Modes

A tearing mode is an instability resulting from the reconnection of magnetic field lines, occurring for β_N higher than 0.5.[4] This results in a region with closed magnetic field, which is referred to as a magnetic island. The separatrices are the boundaries between the magnetic field lines enclosed in the island and the field lines outside the island. Based on the radius r_s at which the tearing mode occurs, a distinction is made between the inner and outer separatrix, which are respectively the separatrix at $r < r_s$ and $r > r_s$. Tearing modes occur at rational values of the safety factor, for instance near the $q = 2/1$ or $q = 3/2$ surface. Figure 2.2 shows a quarter of a tokamak cross section with a $q = 2/1$ magnetic island. The O-point, at the center of the island, and the X-point, where the two separatrices cross, are indicated in the poloidal cross section in the figure. Note that in a three dimensional geometry, the X-point and the O-point both represent unperturbed magnetic field lines. The magnetic island can be described with the helical coordinate ξ, which relates to the toroidal and poloidal angles $m\xi = m\theta + n\phi$. Generally, magnetic islands show a toroidal rotation.

The Neoclassical Tearing Mode (NTM) is driven unstable by a lack of local bootstrap current. The bootstrap current, arising from a radial pressure gradient, is described by neoclassical theory, which takes into account effects arising when a cylindrical plasma column is bent into a torus. Large NTMs can result in a sudden loss of the plasma, an event known as a disruption.[4] During a disruption the plasma current reroutes through the conducting wall of the tokamak, which in combination with the magnetic fields results in large forces on the tokamak structure.[11] The occurrence of a disruption is more likely if the NTM stopped rotating, an event known as mode-locking. A combined model for island growth and rotation is presented in chapter 5.

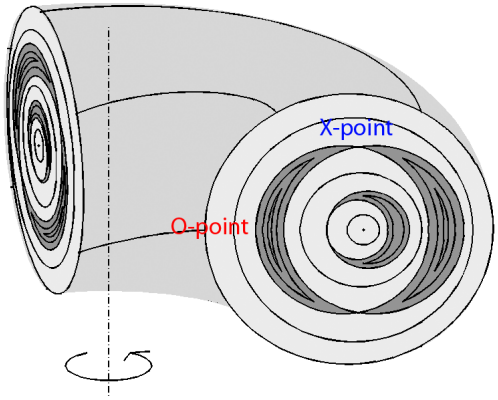

Figure 2.2.: *A $q = 2/1$ magnetic island shown in a cut-through of a tokamak. The X-point and O-point are indicated. Note the periodicity of the island in the poloidal plane. The figure is adapted from Classen.*[13] *A $q = 1$ sawtooth instability is also shown in the figure, but is not discussed further in this work.*

The NTM leads to a region with increased transport, resulting in a perturbation of the equilibrium temperature profile in a tokamak. Subsection 2.2.1 presents a model for the perturbed temperature profile.

2.2.1. Temperature profile perturbation

The increased radial transport in the island results in a flat temperature profile in the island and a reduction of the core temperature. The extent of the flat temperature region in a radial cross section depends on the island phase. As a consequence, the temperature at a small distance from the resonant surface shows an oscillation, imposed by the rotating island. For radii larger than the resonant surface position r_s, the temperature is higher when the O-point passes and decreases towards a minimum at the passing of the X-point. For radii smaller than the resonant surface position, the temperature is at a minimum when the O-point passes and has a maximum when the X-point passes. This is schematically depicted in figure 2.3. An important consequence that can be derived from this figure is an anti-phase between two temperature oscillations at opposite sides of the island.

A realistic description of the temperature perturbation associated with a magnetic island should take into account the asymmetries observed in various experiments.[15][16][17] The islands are seen to have a larger extent at radii smaller than the resonant surface r_s than on larger radii, leading to an O-point shift to smaller radii. A second effect is the larger temperature fluctuations outside the island at smaller minor radii, resulting from an asymmetry in the helical flux perturbation consistent with theoretical considerations. The effect of inclusion of higher order

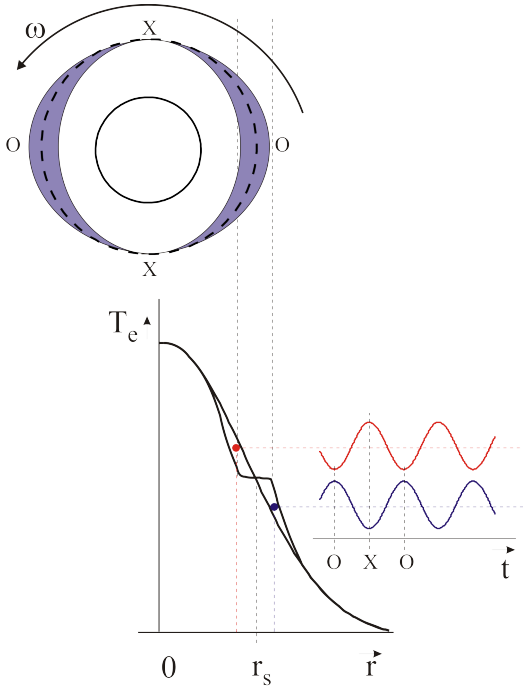

Figure 2.3.: *Schematic representation of the temperature fluctuation associated with a magnetic island, courtesy of Oosterbeek.*[14] *A $q = 2/1$ magnetic island is shown, rotating in a poloidal projection. The temperature measured on opposite sides of the resonant flux surface shows an oscillation at the island rotation frequency ω that is in anti-phase. The temperature at $r > r_s$ is always higher than the temperature at $r < r_s$. The difference is minimal for the O-point and maximum for the X-point.*

asymmetric terms in the Generalized Rutherford Equation is evaluated by De Lazzari *et al.*[18] In general, ECCD suppression is unchanged as long as it is deposited on the, possibly shifted, island O-point.

The calculation of a realistic temperature perturbation by a magnetic island is based on the perturbation of the magnetic equilibrium. As a result of magnetic islands, the temperature profile no longer depends only on the flux coordinate, but on all three coordinates (r_c, θ, ϕ). The cylindrical radius $r_c = \sqrt{\frac{S(\psi_0,\sigma)}{\pi}}$ is determined by the surface S enclosed by the equilibrium helical flux ψ_0, where σ indicates the position relative to the rational flux surface with $\sigma = -1$ for $r_c < r_{c,s}$ and $\sigma = +1$ for $r_c > r_{c,s}$, with $r_{c,s}$ the minor radius in cylindrical coordinates of the NTM rational surface. The helical flux is defined in such a way that it has a minimum at $r_{c,s}$.

The presence of a magnetic island results in a perturbation of the helical flux given by

$$\widetilde{\psi} = \widetilde{\psi}(r_{c,s}) \frac{r_c^2}{r_{c,s}^2} \frac{\left(1 - \frac{r_c}{a}\right)^2}{\left(1 - \frac{r_{c,s}}{a}\right)^2} \cos\left(m\theta + n\phi + \xi_0\right), \tag{2.1}$$

with ξ_0 the phase of the island. Using the perturbation at the resonant surface $\widetilde{\psi}(r_{c,s})$, the extent of the mode is set to correspond with an island of width w, determined as an average of the width of the island on the low and high field side in the equatorial plane.

As a result of the incompressibility of the flux surfaces the temperature can be related to the equilibrium temperature profile $T_0(r_c)$. Inside the island, the temperature T_{isl} is constant and equal to the temperature at the outer separatrix. A temperature difference ΔT results from temperature equilibration in the island. The temperature $T(r_c, \theta, \phi)$ at a position (r_c, θ, ϕ) outside the island is related to the equilibrium temperature profile by the helical flux. The temperature profile is therefore given by

$$\begin{aligned}
\psi > \psi_{sep} \text{ and } \sigma = +1 \qquad & T(r_c, \theta, \phi) = T_0\left(\sqrt{\frac{S\left(\psi(r_c,\theta,\phi),\sigma\right)}{\pi}}\right) \\
\psi < \psi_{sep} \qquad & T_{isl} = T_0\left(\sqrt{\frac{S\left(\psi_{sep},+1\right)}{\pi}}\right) \\
\psi > \psi_{sep} \text{ and } \sigma = -1 \qquad & T(r_c, \theta, \phi) = T_0\left(\sqrt{\frac{S\left(\psi(r_c,\theta,\phi),\sigma\right)}{\pi}}\right) - \Delta T \\
& \Delta T = T_0\left(\sqrt{\frac{S\left(\psi_{sep},-1\right)}{\pi}}\right) - T_0\left(\sqrt{\frac{S\left(\psi_{sep},+1\right)}{\pi}}\right)
\end{aligned}, \tag{2.2}$$

with ψ_{sep} the helical flux at the island separatrices and $S\left(\psi, \sigma\right)$ the enclosed area in the poloidal cross section by the flux surface defined by ψ and σ. The effect of a 2/1 magnetic island on the temperature profile is shown in figure 2.4.

2.3. Electron Cyclotron Emission

A charged particle moving along a magnetic field line, with a velocity component perpendicular to the magnetic field line, experiences a Lorentz force that results in a gyrating motion of the particle. The rotation of electrons around the magnetic field lines in a tokamak results in Electron Cyclotron Emission (ECE). This section is devoted to the physical background of ECE and its detection using radiometry.

Subsection 2.3.1 presents the most important relations between temperature and intensity for thermal ECE. Measurement of ECE intensity using radiometry is introduced in subsection 2.3.2.

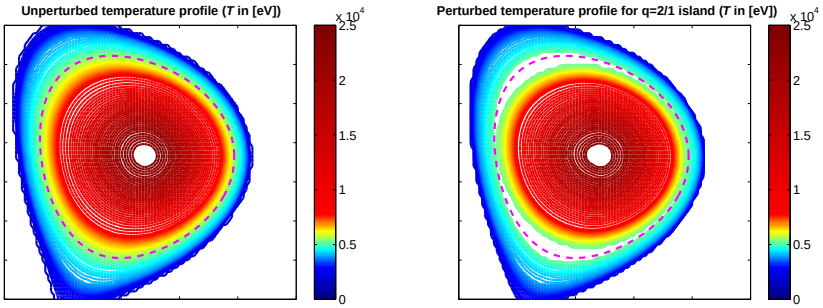

(a) Unperturbed temperature profile **(b)** Perturbed temperature profile

Figure 2.4.: *Contours of equal temperature are shown. A dashed magenta line indicates the position of the q=2/1 flux surface. The temperature in the island is constant. The temperature drop due to the island produces a lower core temperature, compared to the unperturbed profile.*

The relation between the detected power and the temperature of the plasma is discussed in subsection 2.3.3. An expression for the radiometer noise is derived in subsection 2.3.4.

The theory presented in this section is for the largest part based on the discussion of ECE physics in a book on plasma diagnostics by Hutchinson and a review paper on heterodyne radiometry by Hartfuss *et al.*[19][20]

2.3.1. Temperature and ECE intensity

The ECE intensity is described by the radiation transport equation

$$\frac{d}{ds}I(f) = j(f) - I(f)\alpha(f), \tag{2.3}$$

where s is the path length, f the ECE frequency, j the emissivity and α the absorption coefficient. The position of the EC resonant frequency $f_{res} = m\frac{eB}{2\pi m_{r,e}}$, where m is the harmonic number, B the spatially dependent magnetic field magnitude and $m_{r,e}$ the relativistic electron mass, determines the position of emission and absorption peaks of EC waves.

If there is local thermal equilibrium, the local absorption coefficient and local emissivity are related to the black body intensity via Kirchof's law

$$\frac{j(f)}{\alpha(f)} = B(f) = \frac{f^2}{c^2}\frac{hf}{e^{\frac{hf}{k_B T_e}} - 1} \overset{hf \ll k_B T_e}{=} \frac{f^2 k_B T_e}{c^2}, \tag{2.4}$$

where the black body radiation $B(f)$ is given by Plank's radiation formula, which simplifies to the classical Rayleigh-Jeans approximation when $hf \ll k_B T_e$, which holds for tokamak plasmas.

In this equation, c is the speed of light, h is Planck's constant, k_B the Boltzmann constant and T_e the local electron temperature.

For optically thick plasmas, for which the ECE originates from a narrow spatial region, the intensity

$$I(f) = \frac{j(f)}{\alpha(f)} = \frac{f^2 k_B T_e}{c^2} \tag{2.5}$$

scales with the electron temperature T_e and provides a local temperature measurement. In practice, due to the relativistic electron mass and the Doppler shift, an offset is seen between the actual emission position and the position expected based on the resonance f_{res}. As a result of the spatial dependence of the magnetic field, ECE provides a spatially resolved intensity $I(f)$ related to the electron temperature.

A more elaborate discussion of ECE theory is found in appendix A.

2.3.2. ECE radiometry

In tokamaks, ECE is commonly measured using a radiometer. This device mixes ECE with additional radiation from a local oscillator at frequency f_{LO}, shifting down the frequency spectrum to the intermediate frequency (IF) range $f_{IF} = f_{ECE,cent} - f_{LO}$, where $f_{ECE,cent}$ is the central frequencies in the measured ECE spectrum.

The IF signal is amplified and divided over multiple channels using either power dividers or frequency selective couplers. Using filters, different frequency bands in the IF signal are selected, of which the signal is detected using Schottky diodes resulting in a voltage output proportional to the signal intensity. The IF bandwidth B_{IF} limits the radial accuracy of the ECE measurement. The video bandwidth B_v, used in a filter to suppress high frequency noise, determines what fluctuations on the signal intensity can be detected, thereby setting the time resolution.

Diodes typically have a maximum input power of about $5 \cdot 10^{-6}$ W and a voltage sensitivity of 1000-2000 $\frac{\mathrm{V}}{\mathrm{W}}$.[20] The millivolt output signal from the diodes is amplified to arrive at a voltage suitable for the data acquisition system. Figure 2.5 shows a schematic of a radiometer setup with four channels. The power that is detected using the antenna is discussed in the next subsection.

2.3.3. Detected ECE power

An antenna views the ECE coming from the plasma. The sensitivity of the antenna for radiation from different directions, the antenna pattern, can be described by the effective surface $A_e(\Omega_s)$ for which equation 2.6 holds, where Ω_s is the solid angle.[20]

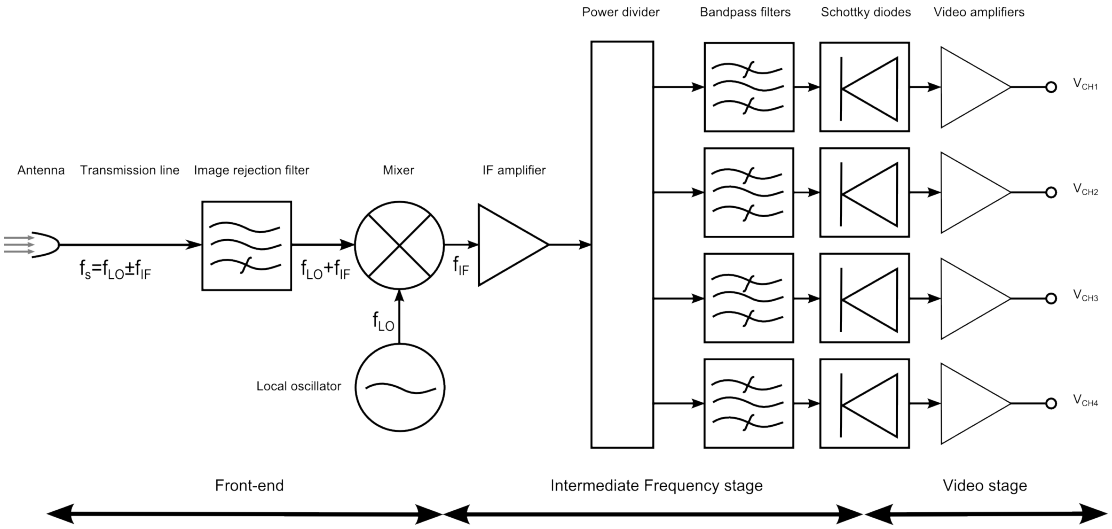

Figure 2.5.: *Schematic figure of a multichannel radiometer setup. ECE, consisting of a range of signal frequencies $f_s = f_{LO} \pm f_{IF}$, is collected with an antenna and transmitted to the image rejection filter, which suppresses frequencies below f_{LO}. The resulting signal at frequency $f_{LO} + f_{IF}$ is mixed with a second microwave signal at frequency f_{LO}. This results in a set of down-converted frequencies f_{IF}, which are amplified. The signal is divided over four channels. Each channel has a different bandpass filter, which filters a specific frequency range, each related to the position in the plasma from which the ECE originated. Using Schottky diodes the radiation intensity is measured. The resulting voltages are amplified and registered with a data acquisition system.*

$$\int_{4\pi} A_e\left(\Omega_s\right) d\Omega_s = \frac{c^2}{f^2} \tag{2.6}$$

The detected power P_f at frequency f is the product of the ECE intensity, described by equation 2.5, and the effective surface:

$$P_f = \int_{4\pi} A_e\left(\Omega_s\right) I(f) d\Omega_s \approx k_B T_e. \tag{2.7}$$

The approximation in equation 2.7 assumes the plasma is optically thick and the antenna pattern is completely filled, i.e. ECE is detected from every direction for which the antenna is sensitive. It is seen that in this assumption the measured power scales linearly with the temperature.

2.3.4. Noise sources

Thermal noise from ECE determines the measurement accuracy that can be reached. For measurements of fusion plasmas, the noise introduced by the radiometer is negligible. Thermal Gaussian white noise originates from the incoherent nature of the ECE.[19]

The IF filters result in a maximum signal frequency B_{IF} and consequently an intensity that fluctuates with twice this frequency. The fluctuating intensity is measured by detectors with a video bandwidth B_v, resulting in an integration time $\tau = 1/(2B_v)$. Therefore every measurement point by a detector is an average over $N = 2B_{IF}\tau$ intensity measurements. The resulting root mean square error of the intensity measurement by the detector is a factor $\sqrt{N}$ lower than the root mean square error of the measured temperature. The root mean square error ΔT_t of the temperature measurement is described by equation 2.8, in which use is made of the linear relation between black body temperature and signal intensity and the root mean square error of a single temperature measurement from a Gaussian distribution using a square law detector is given by its variation $\sqrt{2} < T_t >$.

$$\frac{\Delta T_t}{< T_t >} = \sqrt{\frac{2B_v}{B_{IF}}} \tag{2.8}$$

3. NTM control on ITER

Experiments in current tokamaks have shown the possibilities of control using Electron Cyclotron Current Drive and Resonant Heating (ECCD/ECRH) for NTM suppression and ECE or Mirnov coils for mode detection. Appendix B discusses a few of the NTM control experiments performed on current tokamaks. ITER will be equipped with ECE and ECCD which are discussed in the first section. This chapter concludes with three possible control loops for full suppression of NTMs on ITER.

3.1. ITER EC systems

ITER is the next generation tokamak, which is currently under construction at Cadarache, France. With a major radius of 6.2 m, minor radius of 2.0 m and elongation κ of 1.7, it will be the largest tokamak.[21] Figure 3.1a shows an impression of the ITER tokamak with a plasma in it. Consensus has been reached on application of ECCD as NTM suppression actuator.[22] The choice of a sensor for NTMs has not yet been made. However, ECE is a good candidate, because it allows for simultaneous measurement of the location, width and phase of a magnetic island. In the following two subsections the current ECCD and ECE system designs for ITER are presented. Figure 3.1b shows the position of the ITER ECCD and ECE systems in a poloidal plane.

3.1.1. ECCD

ECCD on ITER will be provided using 24 gyrotrons, each producing 1 MW continuous wave power at 170 GHz.[25] Wave guides transport the radiation to the tokamak, with loss, yielding approximately 20 MW Electron Cyclotron Wave (ECW) power for insertion in the plasma. There is a total of 18 upper ports at the low field side and the ECW launchers for, among others, NTM control are placed in upper ports 12, 13, 15 and 16.[22]

Each Upper Port Launcher (UPL) has a Lower Steering Mirror (LSM) and an Upper Steering Mirror (USM). Both mirrors focus up to 4 beams of up to 1 MW power in the plasma. The angle β, between the initial beam direction and its poloidal projection, will be 18° for the LSM to optimize the current drive density at the $q = 2/1$ flux surfaces, using 13.3 MW maximum power.

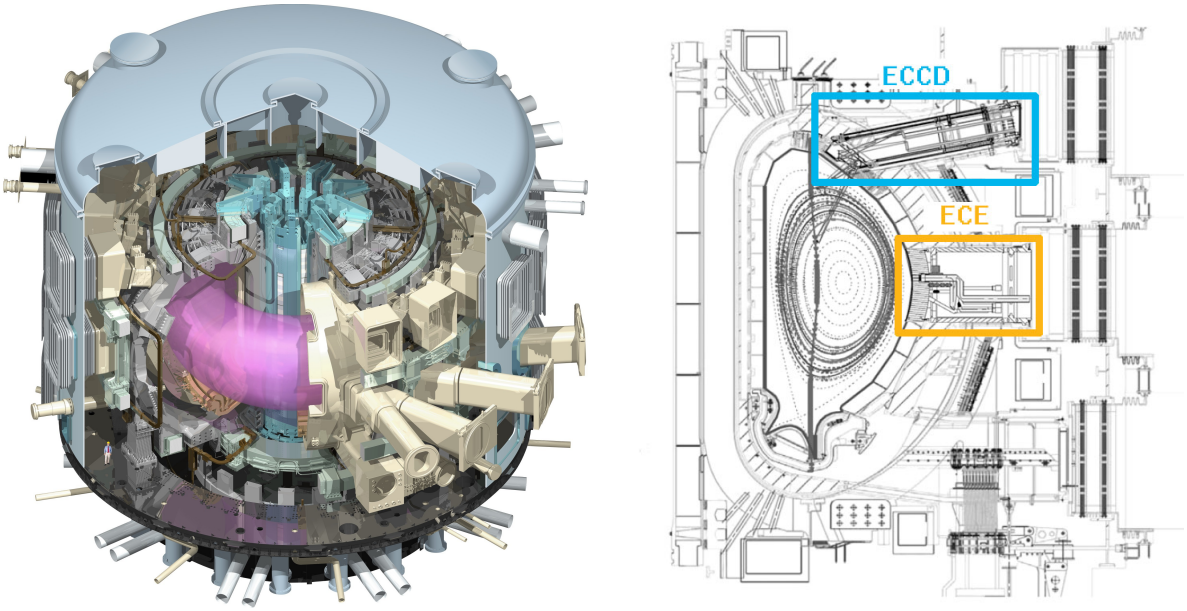

(a) ITER tokamak with plasma

(b) Position of ECE and ECCD

Figure 3.1.: *On the left, an artistic cutaway of the ITER tokamak with a plasma inside it is shown. Note the man standing in the bottom left. On the right, a poloidal cross section of ITER is shown. In this cross section, one of four ECCD launchers is indicated in blue. The equatorial ECE diagnostic is indicated in orange. The magnetic flux surface of the plasma are depicted, as well as rays originating from the ECCD launcher. The left picture is from the ©ITER Organization (http://www.iter.org/). The right picture is a combination of pictures from Henderson et al[23] and Austin et al[24].*

Both mirrors will be equipped with a pneumatic actuator, achieving an accuracy of 0.02° of the angle α, defined as the angle between the horizontal plane and the ECCD beam projected in the poloidal plane.[23] The design requirement for the mirror angle is a variation of the angle from -7° to +7°, resulting in a change of angle α from -14° to +14° from the equilibrium position, within 3 seconds.[26] Prototype tests show a settling time of 1 s going from -5° to 5° mirror angle and a time of 2.5 s going from 5° to -5°, which is slower than the requirement.[27]

3.1.2. ECE

The radiometers, located in equatorial port 9, cover a frequency range of 110-220 GHz for the first harmonic O-mode and 220-320 GHz for the second harmonic X-mode respectively.[24] The first radiometer measures the plasma from the low field side at a major radius of 8.2 m up to the high field side with a radius of 5.1 m, thus encompassing the plasma major radius of 6.2 m. The second radiometer provides only a measurement on the low field side. Both radiometers will be equipped with at least 30-channels. This results in a spatial resolution of 7 cm.[24] Recently a

channel spacing of 2-4 GHz for the first harmonic O-mode and 4-6 GHz for the second harmonic X-mode was proposed, with the smallest spacing on the low field side.[28]

3.2. NTM control loops for ITER

This section presents three possible control strategies for NTMs on ITER. One based on reconstruction of the q-profile and ray tracing to determine the deposition position, a second based on modulated ECCD and a third based on ECE along the ECCD line-of-sight.

General remarks applicable to all three control loops are presented in the next subsection. A control loop based on reconstruction and ray tracing is introduced in subsection 3.2.2. Modulated ECCD forms the basis of the control loop in subsection 3.2.3. A line-of-sight ECE system is included in the control loop in subsection 3.2.4.

3.2.1. General remarks

For each of the four NTM suppressing ECCD launchers, the waves are characterized by the peak power P and a periodic modulation $\rho(t)$ of the peak power. The control loops below provide means to attain a modulated ECCD signal in phase with the island, because this increases the suppression capabilities of ECCD. The angle α of the ECCD launcher determines the deposition location. As a result each ECCD launcher has three input signals: the angle α, the ECCD peak power P and the power modulation $\rho(t)$.

The control loops presented have the aim to fully suppress a magnetic island before it locks. The control loops assume the presence of a rotating magnetic island to fully work. In the control loops the island width w is used as an indicator for the presence of an island. Given sufficient accuracy in the measured island width w, the control loop can be fitted with a peak power controller to maintain a constant island width.[29] The modulation $\rho(t)$ is directly measured from the temperature fluctuation of the island, which is measured with ECE. The control loops differ in the way they provide the angle α.

The aim of the control loops in this work is to give an overview of ways to include ECE in a control loop and briefly address a few advantages and challenges of different control loops as a starting point for further studies.

3.2.2. Reconstruction and ray tracing

A control loop based on reconstruction and ray tracing uses four controllers: a ray tracing routine, an equilibrium reconstruction routine, a controller for power modulation and a controller

for the peak power. Figure 3.2 shows the control loop. Reich *et al* discuss a control loop based on these principles.[30]

The main part of this control loop is a ray tracing routine. This is used to determine the angle α needed to deposit at the right flux surface. The propagation of ECCD depends on the profiles of the electron density n_e and temperature T_e and the magnetic topology provided by the toroidal magnetic flux Ψ and the safety factor q as a function of position. The electron temperature T_e is measured with ECE and the electron density n_e can be determined from interferometry or polarimetry measurements.[19] The radial location of the magnetic island is measured with ECE. The location of the $q = 2/1$ or $q = 3/2$ flux surfaces could also be used as an indication for the location of island, but the accuracy of this estimation depends on the accuracy of the equilibrium fitting routine.

The safety factor q and the magnetic flux Ψ are determined from a reconstruction of the magnetic equilibrium. The EFIT code is commonly used for this reconstruction, using magnetic measurements of the plasma position and shape and the toroidal magnetic field B_t and plasma current I_p as input.[31 32] These global magnetic measurements need to be complemented with local measurements of, for instance, the poloidal magnetic field, measured using polarimetry, or the pitch of the magnetic field, measured with the Motional Stark Effect (MSE).[19] All included measurements constrain EFIT, thus making the reconstructed profile more reliable, at a cost of a larger lag between the calculated situation and the actual situation.

The required modulation and the island width are measured directly using ECE. Mirnov coils could serve as a backup or additional diagnostic in both cases. The coils can provide the phase and the amplitude of the oscillations scales with the island width.[19]

A drawback of this control loop is the two opposing requirements for the ray tracing and reconstruction routines. They should give accurate values for the required launcher angles α and do this as fast as possible. Therefore the launcher angle set points α_s will always lag behind on the best possible position for that time instant, which only works if the lag is small compared to the time scales on which the magnetic equilibrium and magnetic island position change. Alternatively, a lookup table with precalculated angles for a set of deposition positions could be used to ensure smaller delays in the loop.

3.2.3. Frequency modulation of ECCD

Manini *et al* propose to measure the ECCD deposition position with ECE, using a modulation of ECCD at different frequencies for all of the four launchers.[33] By correlation of the modulation input with the measured ECE signals, the deposition position of each individual launcher is found.[7]. The magnetic island and the deposition position are both detected using equatorial ECE. Figure 3.3 shows the control loop.

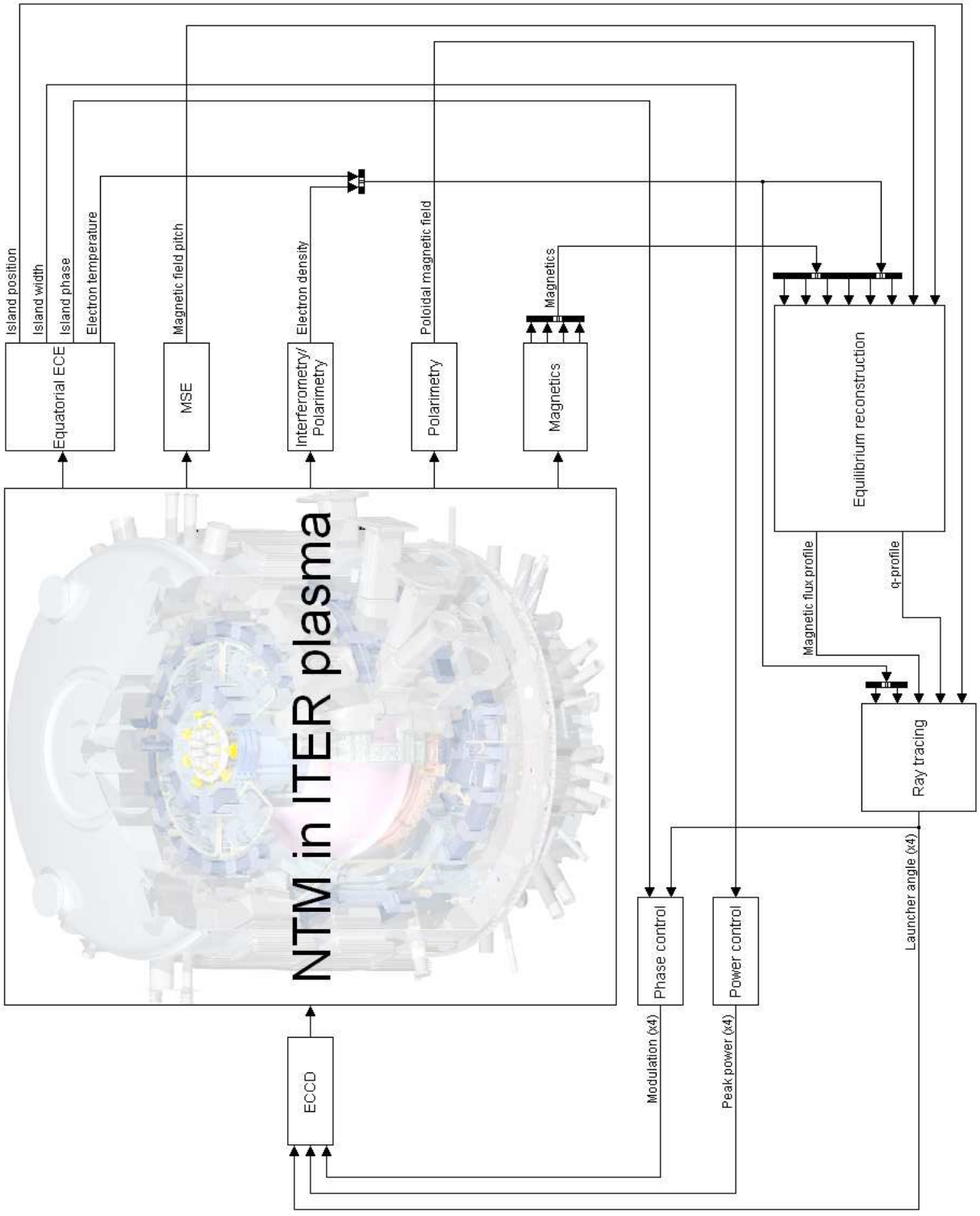

Figure 3.2.: *Schematic representation of a control loop based on an equilibrium reconstruction of the magnetic flux and q-profile. A ray tracing routine calculates launcher angle set point.*

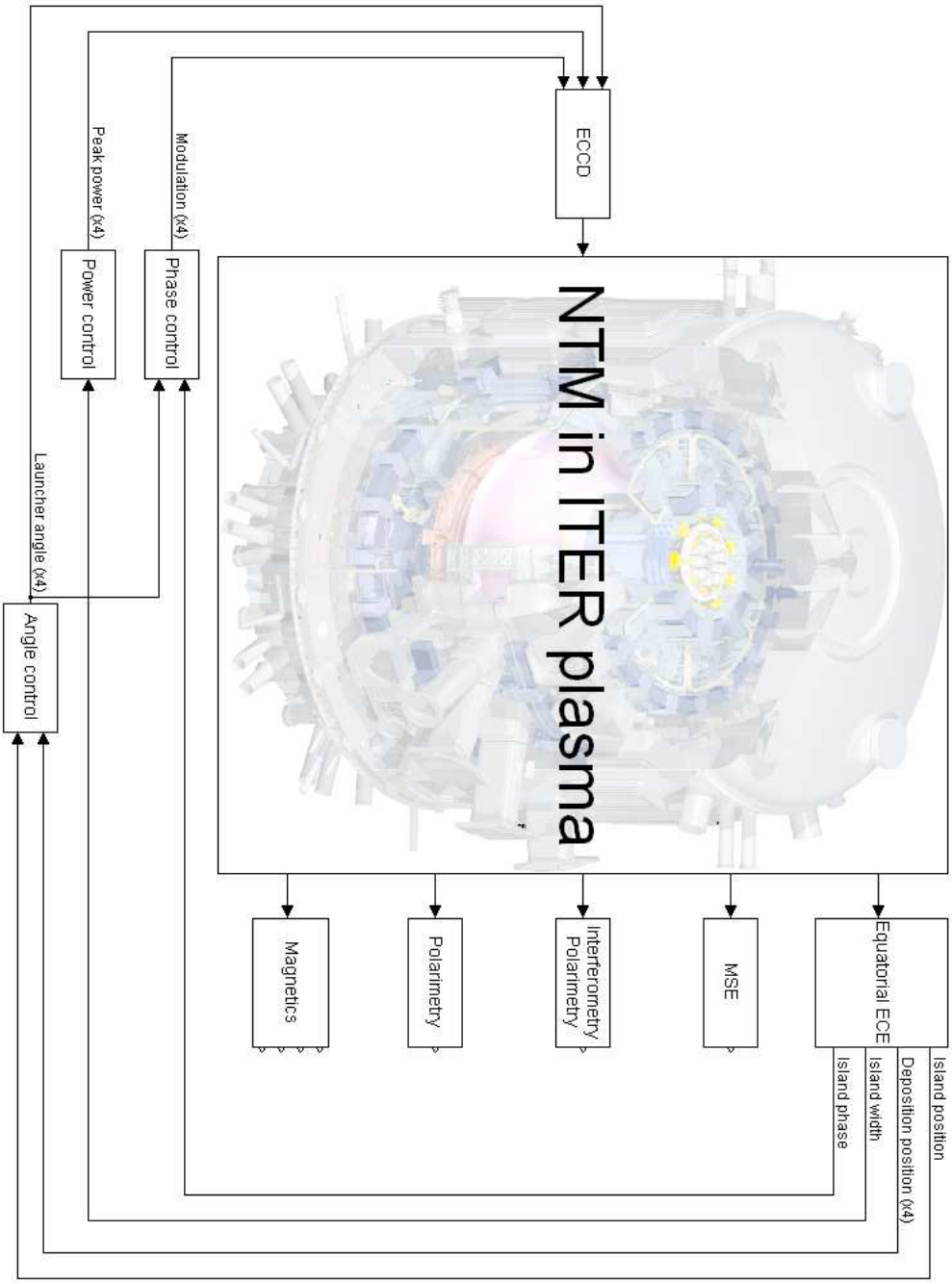

Figure 3.3.: *Schematic representation of a control loop based on frequency modulated ECCD. The four deposition positions are measured with ECE.*

An advantage, compared to the control loop in the previous subsection, is the lack of components that introduce lag as a result of computations. The control loop does require more power, because ECCD should be active before the launchers are focussed on the islands. In this case, the deposited power should be such that the temperature oscillation is clearly visible, but does not produce a significant change of the plasma or increase instability of the tearing mode. The frequencies at which the different launchers are modulated should be distinguishable from each other and from the rotation frequency of the magnetic island. The performance of this control loop is largely determined by the accuracy that can be reached in the measurement of the ECE frequency of the different ECCD beams and the magnetic island.

3.2.4. Line-of-sight ECE system

A line-of-sight ECE system requires the backward propagating EC waves, resulting from the plasma, to be separated from the forward propagating ECCD using, for instance, a FAst DIrectional Switch (FADIS).[34] Using a radiometer, the frequency of the radiation coming from the O-point of the island is determined and feedback on the difference between this frequency and the ECCD frequency controls the angle α. Each ECCD launcher is equipped with its own line-of-sight system. The phase of the island rotation and the island width are determined using the line-of-sight ECE measurements as well. The control loop is depicted in figure 3.4. A line-of-sight system has been used for positioning control on the TEXTOR tokamak.[9]

For the controller to work, the magnetic island should be in view of the ECE system, requiring an initial estimate of the position of the magnetic island, which could be calculated a priori or determined from ray tracing and equilibrium reconstruction. Inclusion of an initial guess of the angle α from measurements should be done with care to ensure the larger delay of a ray tracing and reconstruction routine is not reflected in the overall system performance.

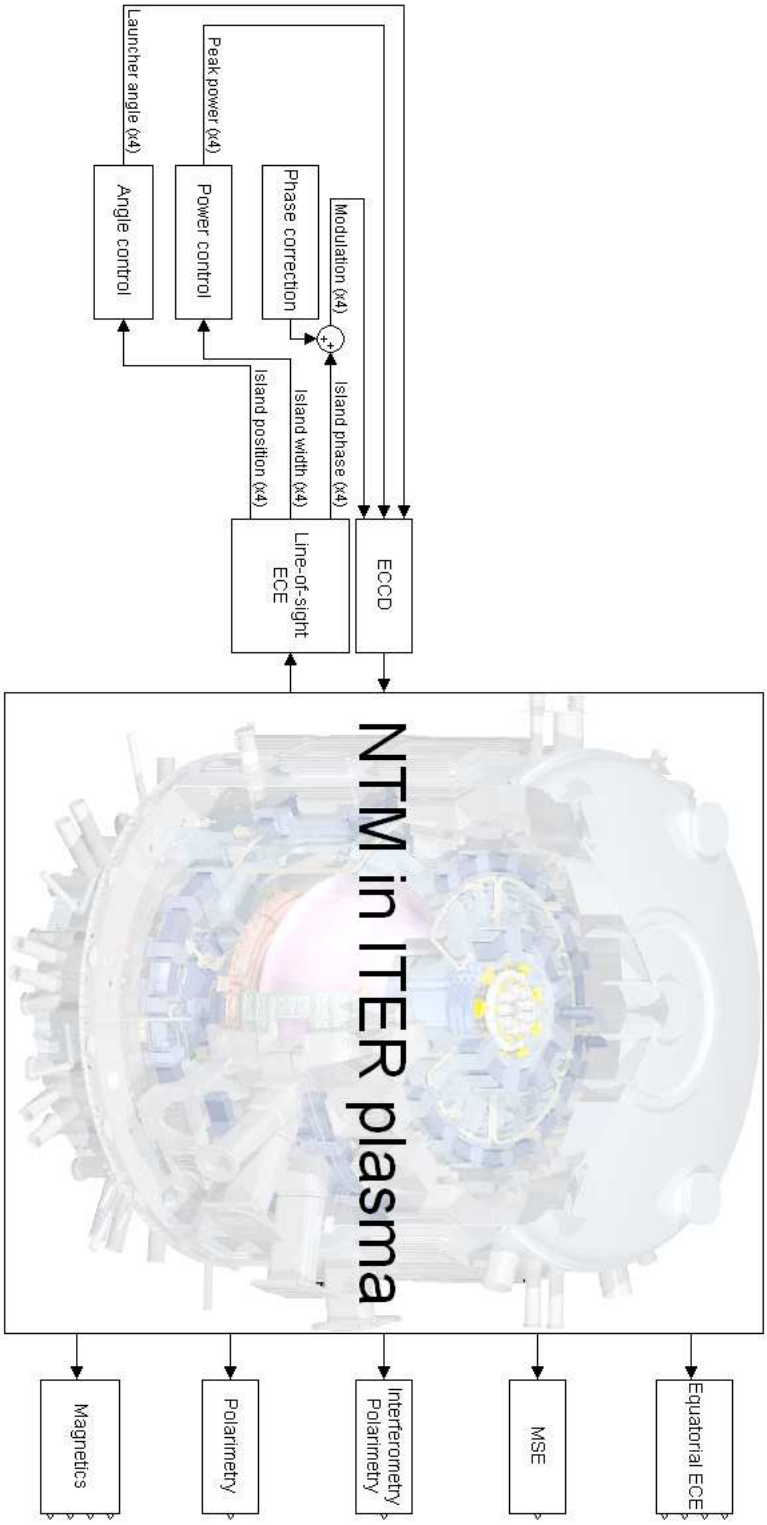

Figure 3.4.: *Schematic representation of a control loop based on line-of-sight ECE measurement.*

4. NOTEC

A reliable simulation of ECE should take into account the wave propagation, the thermal EC resonance, including broadening effects, and the antenna pattern in a realistic way. The NOn-Thermal Ece Code (NOTEC) includes all these effects, making it an appropriate choice for the investigation of the merits of ECE. Its non-thermal routines are not used.

This chapter starts of with a short history of the different parts of the current NOTEC version, which is used in this work. The physics implemented in NOTEC are discussed in section 4.2. Section 4.3 discusses how to produce a close match between NOTEC simulations and ECE measurements. In the last section (section 4.4) simulations of the ECE spectra of the first O-mode and second X-mode are generated and discussed.

4.1. History

The current version of NOTEC, version 2.00, is a Fortran90 version of the original NOTEC code with addition of thermal damping, equilibrium and non-thermal emission routines shared with TORAY and RELAX. The original NOTEC code was created in 1987 and was specifically designed to simulate ECE coming from a non-thermal electron population in the Joint European Torus (JET).[35] Starting from the ECE antenna a cold ray trace is done into the plasma, using the RAYS code by Batchelor and Goldfinger.[36] Along the ray, the radiation transport equations are solved, using (non-)thermal emission/absorption routines.

Over the course of time extra magnetic equilibrium routines have been added. Part of the new routines originated from TORAY, a code for ECRH and ECCD deposition.[37] Notable new additions are a plasma with Shafranov shift and a two-dimensional spline-based equilibrium, able to represent most toroidally symmetric plasma shapes.

The 1987 version of NOTEC only contained an analytical temperature and density profile, which was later extended to also include data-based profiles with cubic spline interpolation. NOTEC does not check the consistency of the provided plasma equilibrium, leaving it to the user to provide consistent temperature, density and magnetic field data.

NOTEC's reliability for thermal ECE has been improved by using thermal absorption routines from TORAY, which are able to calculate ECE using a weak or full relativistic approximation.

A new non-thermal emission and absorption routine based on the RELAX code has been added as well.[38] The original thermal and non-thermal routines can still be used. Temperature perturbations by magnetic islands are added to NOTEC based on an implementation in TORAY.

NOTEC version 2.00 is programmed in Fortran90 style. Most deprecated and obsolescent FORTRAN77 features have been replaced. For instance, NOTEC 2.00 does not contain any COMMON blocks; variables are now exchanged using modules. NOTEC 2.00 also contains inline documentation that can be extracted using Doxygen.[39]

4.2. Physics implementation

In this section, a brief overview of the implemented physics and the assumptions used in NOTEC is given. The plasma equilibrium is discussed first, followed by details about the inclusion of magnetic islands. The cold-plasma ray tracing is introduced next and the section is concluded with the role of the radiation transport equation and different absorption and emission routines.

The NOTEC plasma equilibrium is a static, toroidally symmetric equilibrium. The temperature and density profiles are specified as a function of the magnetic flux coordinate. Using the local values of the magnetic field, temperature and density, NOTEC calculates the plasma dispersion relation, needed for the ray trace, and the absorption and emission, which determine the ECE intensity.

Generally, the presence of a magnetic island disturbs the essentially one dimensional temperature and density profiles, as well as the magnetic equilibrium. The implementation in NOTEC is derived under the assumption that the perturbation of the magnetic and density equilibria are small. It is assumed that temperature is constant inside the island and that the flux surfaces outside the island are perturbed only in their shape. The perturbed flux surfaces retain their temperature, save for a temperature drop for flux surfaces at minor radii smaller than the island position. The method to determine the temperature perturbation resulting from a magnetic island is described in section 2.2.1.

NOTEC is able to determine the radiation collected by an antenna facing the plasma. An antenna pattern is simulated by using multiple rays collected from different angles. A ray is traced for a specified radiation frequency by solving a sixth order time independent derivative of the dispersion relation to the position and wave vector, based on the, cold plasma approximation, RAYS code by Batchelor and Goldfinger.[36]

The level of ECE is found by solving the radiation transport equation (equation 2.3) along the ray trajectory. The absorption and emission between two subsequent points on the ray are integrated using Simpson's rule. If the relative error or the difference with an integration based on the trapezium rule is too large, the ray interval is halved. The (non-)thermal absorption/emission is

calculated for every integration point of the radiation transport equation. The original NOTEC thermal absorption routine is only valid for harmonic of 2 or higher, because this results in a good representation of the thermal ECE contribution in the non-thermal ECE spectra on JET, for which NOTEC was originally used. A weak relativistic routine that calculates only the first two harmonics is also present. The most reliable thermal absorption is calculated using a fully relativistic routine. This routine iteratively solves the biquadratic equation which includes a finite number terms in the finite Larmor radius expansion and evaluates the contributions of a predetermined amount of harmonics. It treats the hermitian and anti-hermitian part of the dielectric tensor separately and employs the equations by Bornatici *et al*[40]. Only the full relativistic routine is used.

4.3. Simulating ECE diagnostics

This section addresses how simulated data that resembles measured data by a radiometer can be produced using NOTEC. First, relevant characteristics of a radiometer are summarized. Based on these characteristics, a method to derive noisy radiometer channel signals from the NOTEC simulated data is presented.

The radiometer is described by a set of characteristics already introduced in section 2.3.2. For ECE simulation, the most relevant once are briefly described below. An antenna collects the ECE using a directional dependency, described by the antenna pattern $A_e(\Omega_s)$. Each radiometer channel has an intermediate frequency bandwidth $B_{IF,i}$ around the channel frequency $f_{CH,i}$ that determines which ECE frequencies are detected in channel i. The signal from channel i equals the sum over all radiation from the ECE frequencies between $f_{CH,i} - B_{IF,i}/2$ and $f_{CH,i} + B_{IF,i}/2$, neglecting other frequency dependent effects.

Gaussian beams with poloidal and toroidal divergence can be simulated. The beam has both a toroidal and poloidal beam width expressed in the standard deviation σ. A beam width specified as the Full Width at Half the Maximum is related to a NOTEC beam width using FWHM = $2\sqrt{2\ln 2}\sigma$. Up to 21 rays can be simulated for a beam, in which case the contribution of a single ray to the beam is determined by a two dimensional Gaussian with the toroidal an poloidal beam widths as standard deviations. The divergence is maximum for the rays at the edge of the antenna and zero for the centre ray. An antenna pattern could also be simulated using a weighted summation of rays starting at user-defined positions.

NOTEC is able to simulate ECE at fixed frequencies. A simulation of a radiometer channel signal is a numerical integration over a set of fixed frequencies. If the channel bandwidth $B_{IF,i}$ is small, ECE intensity will remain nearly constant for all frequencies in the channel. Includ-

ing more frequencies for each channel increases the accuracy. The noise relative to the signal intensity is determined by B_v, B_{IF} and equation 6.4.

The combination of an accurate simulation of the antenna pattern, the integration over the frequencies in a channel and measurement noise results in an intensity spectrum. In this spectrum, the intensity is a relative measurement of the plasma temperature and the frequency is a measure for the position. The radiation position can be approximated by evaluating the magnetic field to determine the cold plasma absorption position.

4.4. ITER spectra simulation

In this section the ECE frequencies suitable for electron temperature measurements are determined for equatorial ECE on ITER. The assessment is performed in two steps. First, the end of the emission region, determined directly from the NOTEC code, is compared with the unshifted EC resonance position, calculated using $f = \frac{e\|\vec{B}\|}{2\pi m_e}$. Secondly, the simulated ECE intensity is compared to an interpolation of the local temperatures. In this case the absorption position is estimated from the unshifted EC resonance position. The frequency ranges, for which the measured intensity corresponds to the electron temperature, are suitable for measurement of the temperature fluctuations resulting from magnetic islands.

The first O-mode ECE intensity detected in the frequency range 110-230 GHz is shown in figure 4.1. The figure shows both the end of the emission region and the intensity as a function of radius, calculated from the unshifted absorption position. The figure shows that the end of the emission position is beyond the EC resonance. The range 120-210 GHz corresponds to the first harmonic O-mode, based on the absorption position. The range 120-180 GHz contains only emission from the first harmonic and shows a good correspondence with the actual temperature. Overlap with the second harmonic is observed for the frequencies 190 GHz to 210 GHz. An outward shift of maximally 18 cm is observed, due to relativistic broadening.

The second X-mode ECE intensity, detected in the frequency range 210-330 GHz, is shown in figure 4.2, for which the end of the emission position is beyond the EC resonance as well. The range 230-280 GHz shows only second harmonic X-mode radiation and has a good correspondence with the actual temperature. An outward shift of maximally 6 cm is observed, due to relativistic broadening.

The ranges that are useful for temperature measurements correspond to the ranges found by Austin *et al.*[24] However, in both spectra a shift of the emission position is observed. This systematic shift results from the relativistic broadening and the large optical thickness in the emission region, which can be corrected using simulations.[41]

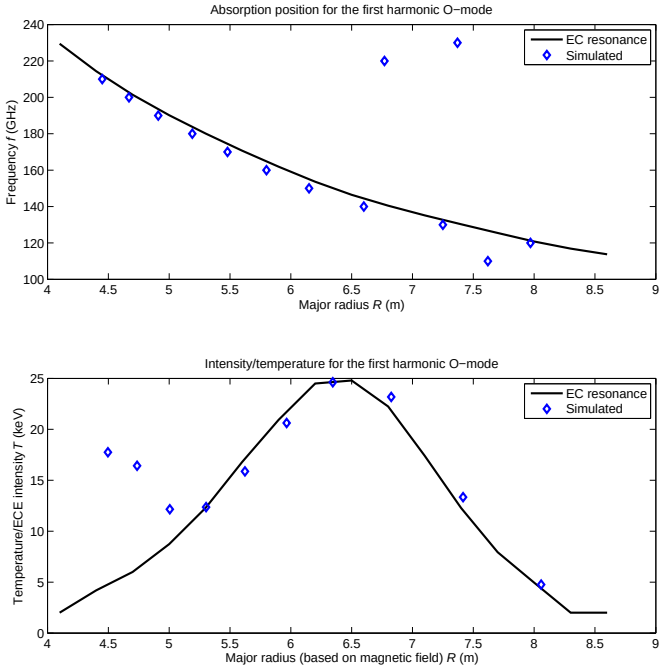

Figure 4.1.: *ECE spectrum for the first harmonic O-mode with the equatorial ECE.*
Top: *End of emission region for 110-230 GHz. The unshifted EC resonance is shown in black. The end of the emission region is beyond the EC resonance position*
Bottom: *Radiation intensity for the frequency range 120-210 GHz for the first harmonic O-mode. The temperature is shown as a black line. Only the first O-mode is measured for frequencies up to 180 GHz (5.4 m), indicated by the good correspondence between measured intensity and actual temperature. A small outward shift of the radiation position compared to the temperature is observed.*

The 2/1 and 3/2 rational flux surfaces are at minor radii r=1.55 m and r=1.3 m respectively.[42] The position of the 2/1 and 3/2 rational surfaces at the high field side are at major radii R=4.65 m and R=4.9 m respectively. Therefore, the NTMs are not measurable on the high field side, where both the first harmonic O-mode and the second harmonic X-mode ECE suffer from harmonic overlap.

Due the larger frequency range covering the low field side, the second harmonic X-mode can attain a higher spatial resolution than the first harmonic O-mode with equal noise levels. Although the absorption and emission coefficient profiles have a similar width, the larger optical thickness results in a narrower emission profile and a decreased relativistic shift for the second harmonic X-mode, making the range 230-280 GHz of this harmonic the preferred range for measuring temperature fluctuations from NTMs.

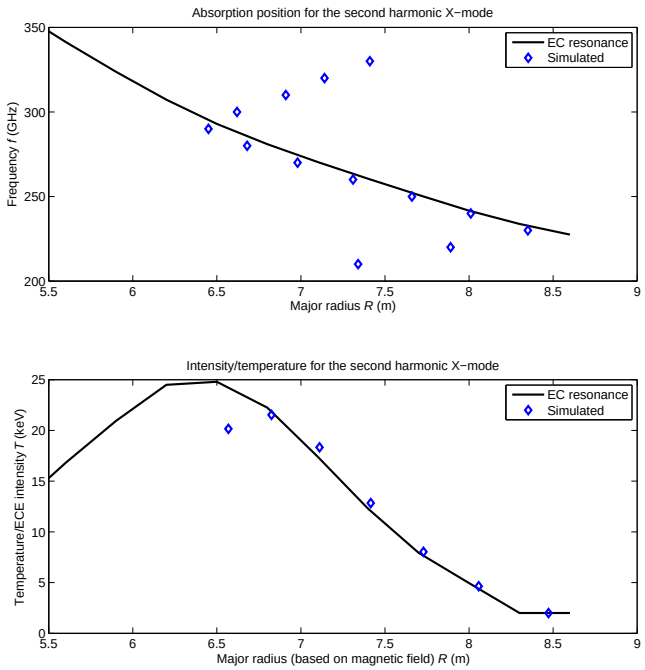

Figure 4.2.: *ECE spectrum for the second harmonic X-mode with the equatorial ECE.*
Top: *End of emission region for 210-330 GHz. The unshifted EC resonance is shown in black. The end of the emission region is beyond the EC resonance position.*
Bottom: *Radiation intensity for the frequency range 230-290 GHz of the second harmonic X-mode. The temperature is shown as a black line. Only the second X-mode is measured for frequencies up to 280 GHz (6.8 m), indicated by the good correspondence between measured intensity and actual temperature. A small outward shift of the radiation position compared to the temperature is observed.*

5. Integrated modelling of island growth, stabilization and mode locking: consequences for NTM control on ITER[1]

H. van den Brand[1a,2], **M. de Baar**[1b,2], **N.J. Lopes Cardozo**[1a] **and E. Westerhof**[2]

[1] (a) Fusion Science and Technology Group (b) Control Systems Technology Group, Eindhoven University of Technology P.O. Box 513, 5600 MB Eindhoven, The Netherlands

[2] FOM Institute for Plasma Physics 'Rijnhuizen', Association EURATOM-FOM, Trilateral Euregio Cluster, P.O. Box 1207, 3430 BE Nieuwegein, The Netherlands

Abstract. Full suppression of Neoclassical Tearing Modes (NTMs) using Electron Cyclotron Current Drive (ECCD) should be reached before mode locking (stop of rotation) makes suppression impossible. For an ITER scenario 2 plasma, the similar time scales for locking and island growth necessitate a combined model, presented in this paper. Using this model, the maximum allowed latency between the seeding of the mode and the start of ECCD deposition and maximum deviation in radial position are determined. The maximum allowed latency is determined for two limiting models for island growth; the polarization model with $w_{marg} = 2$ cm, representing the worst case, and the transport model with $w_{marg} = 6$ cm, representing the best case. NTMs with seed island widths up to 9.5 cm and 12 cm for the 2/1 and the 3/2 NTM, respectively, are suppressible. The maximum allowed latency is 1.05 s and 2.95 s for the 2/1 and 3/2 NTM respectively for the worst case model. Radial misalignment should not exceed 7-10 mm for the 2/1 NTM and 5-16 mm for the 3/2 NTM depending on the model for island growth. As long as the alignment suffices, it does not result in additional latency. Mode locking has serious implications for any real-time NTM control system on ITER that aims to suppress NTMs by ECCD.

[1]This chapter has been submitted as a paper to Plasma Physics and Controlled Fusion. Section 5.6 is added to discuss the results of the paper in relation to this thesis in particular.

5.1. Introduction

In order to prove the technical viability of fusion power, the ITER tokamak (major radius $R_0 = 6.2$ m, minor radius $a = 2$ m and elongation $\kappa = 1.7$) is under construction.[21] Plasmas in ITER should maintain a fusion gain $Q = 10$ for 300 s. In order to achieve these goals, plasma instabilities are to be prevented. A particular example is the Neoclassical Tearing Mode (NTM), an MHD instability, which reduces the core temperature, and therefore the fusion yield and can result in the loss of the entire plasma (a disruption).[4] An NTM is a global magnetic perturbation, with poloidal and toroidal mode numbers m and n respectively, which creates a magnetic island on the resonant flux surface, where the safety factor $q = m/n$. The amplitude of the mode is characterized by the full island width w. The metastable NTM is driven unstable at finite island width due to the loss of local bootstrap current inside the island itself. Electron Cyclotron (EC) waves can provide local current through EC Resonance Heating (ECRH) and Current Drive (ECCD), replacing the missing bootstrap current in the island and thereby stabilizing or suppressing the NTM.[43] In ITER, the NTMs with mode numbers $m/n = 2/1$ and $m/n = 3/2$ will degrade the core temperature the most.[5]

An NTM rotates with the local plasma fluid velocity at the resonant surface. Interaction with the wall results in a slowdown of the rotation. When this interaction becomes strong enough, the mode can come to a standstill, a situation known as mode locking. In that case, the stabilizing effect of the wall is lost and the mode can grow to still larger amplitudes. In particular, for the case of the 2/1 mode this generally results in a disruption.[12]

ECCD stabilizes the NTM if the current is driven near the island O-point, i.e. the center of the magnetic island. Current drive near the island X-point, the crossing of the two separatrices of the magnetic island, has a destabilizing effect.[6] Experiments show that for large phase mismatches between island O-point and ECCD the NTM is not fully suppressed.[6][44][45] In ITER, the four heating and current drive EC Upper Port Launchers are dedicated to the control of NTMs. They are situated in upper ports spanning a range of only 100° in toroidal angle around the ITER torus.[22] When the mode locks in an unfavourable position, in which ECCD cannot be driven close enough to the O-point, ECCD is unable to stabilize the mode. Therefore in order to guarantee suppression by ECCD, modes should be suppressed before locking occurs.

La Haye *et al* investigated for which island widths mode locking occurs, using an induced wall drag model adapted from Nave and Wesson.[46][47] Figure 5.1, produced using this rotation model (for details see section 5.2.2), shows that the time it takes for an NTM to lock varies strongly with the island width. The characteristic timescale for island growth is $w/\frac{dw}{dt}$, where $\frac{dw}{dt}$ is the island growth rate in the absence of ECCD (for details see section 5.2.1 for the polarization model with $w_{marg} = 2$ cm). Figure 5.1 shows that the locking time is comparable to the growth

time for the relevant island width range from 5 to 10 cm. The locking time is neither infinitely fast, which would result in the island width limits by La Haye *et al*, nor is it slow enough to justify neglecting island rotation, as is often done in discussions of the NTM control problem (see for example[5]). Consequently, the derivation of control requirements must be based on a model combining the growth of the mode and the evolution of the mode rotation.

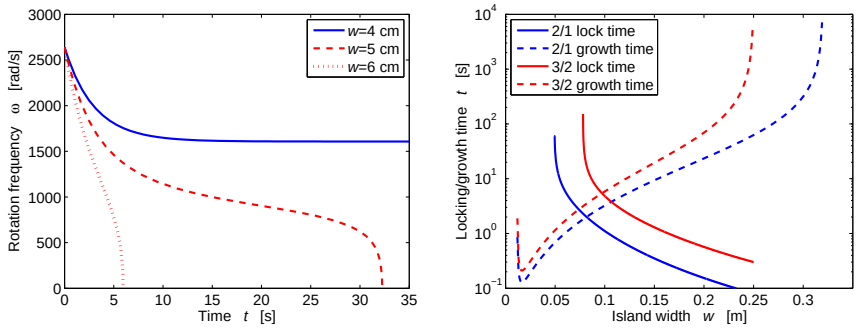

Figure 5.1.: *The left figure shows the evolution of the rotation frequency of a 2/1 mode with a fixed island width w. The solid line shows the rotation frequency for a 4 cm island, which does not lock. The dashed and the dotted lines represent the rotation frequency for a 5 cm and 6 cm island, respectively which both lock. The right figure shows the locking and island growth time as a function of the fixed island width for the 2/1 mode (blue) and 3/2 mode (red). The solid lines are the locking times and the dashed lines are the growth times based on the Generalized Rutherford Equation(for details see section 5.2.1).*

Using a combined model of mode growth and rotation, this paper investigates how the prevention of mode locking, as a control objective, affects the requirements on a real-time NTM control system. In particular, we look at the maximum allowed latency and the maximum allowed deviation in radial deposition position compared to the island O-point. Under latency we understand the time delay between the island seeding and the start of ECCD deposition at the proper location to suppress the mode. During this time, the control system should i) detect the mode and identify its position in the plasma and ii) steer the launcher to position the ECCD at the location of the mode. The maximum allowed latency is the longest time delay that still ensures a full suppression of the island before mode locking and similarly for the maximum allowed deviation in radial deposition position. In section 5.2, the Generalized Rutherford Equation (GRE) and the rotation model are briefly described and the relevant model parameters are specified. In section 5.3, the model combing the GRE and mode rotation is used to calculate the maximum allowed latency and the required accuracy of ECCD positioning. The results are discussed with a focus on the implications for ITER in section 5.4. The conclusions of the work are presented in the final section.

5.2. Model

5.2.1. Generalized Rutherford Equation

The Generalized Rutherford Equation (GRE) describes the island growth rate $\frac{dw}{dt}$ as a function of island width w, averaged over the equatorial plane high field side and low field side, based on an average of the current diffusion equation over the area covering the magnetic island including appropriate corrections in Ohm's Law from non-inductively driven currents.[4,48] Keeping only the most relevant terms within the current context, it can be written as

$$\frac{\tau_r^*}{r_s}\frac{dw}{dt} = r_s\Delta_0' + r_s\Delta_{\mathrm{BS}}' + r_s\Delta_{\mathrm{CD}}', \tag{5.1}$$

where r_s is the island position measured as half the flux surface width in the equatorial plane and $\tau_r^* = 0.82\frac{\mu_0\kappa r_s^2}{\eta_{NC}}$ is the resistive time scale of island growth with μ_0 being the permeability of free space and κ the plasma elongation. The neoclassical resistivity is $\eta_{NC} = 2.8\cdot 10^{-8} Z_{eff}\,(T_e[\mathrm{kev}])^{-3/2}\left(1-\sqrt{\epsilon}\right)^{-2}$, where Z_{eff} is the effective charge of the plasma ions, T_e the electron temperature in keV and ϵ the inverse aspect ratio, defined as $\epsilon = r_s/R$ with R the major radius.[11] The first term on the right hand side represents the classical stability index, which is a result of the boundary conditions provided by matching to the ideal MHD perturbation in the region outside the island.[48] The other two terms originate from the loss of the bootstrap current inside the magnetic island and the non-inductively driven current from ECCD respectively.[4,49,50] A Neoclassical Tearing Mode (NTM) is driven unstable by the bootstrap term and, generally, has a stabilizing classical stability index. As a consequence, NTMs are linearly stable and require a seed island, provided by other MHD instabilities.[4] The negative value of the classical stability index ensures an upper limit for the island width: the saturated island width w_{sat}. At w_{sat} the destabilizing bootstrap growth term is balanced by the classical growth term: $\Delta_0' = -\Delta_{BS}'(w_{sat})$.

The bootstrap term is a consequence of the flattening of the pressure profile inside the island.[4] This results in the loss of the local bootstrap current density j_{BS} inside the magnetic island, such that an island is driven unstable at the rate[51]

$$r_s\Delta_{\mathrm{BS}}' = \frac{16\mu_0 L_q r_s j_{\mathrm{BS}}}{B_p\pi}\frac{4}{3w} f\left(\frac{w}{w_{marg}}\right), \tag{5.2}$$

where $L_q = q\left(\frac{\partial q}{\partial r}\right)^{-1}$ is the q-profile gradient length and B_p the poloidal magnetic field at the rational surface. The function $f\left(\frac{w}{w_{marg}}\right)$ describes the limitation of the bootstrap growth rate at small island sizes. The precise form of $f\left(\frac{w}{w_{marg}}\right)$ is still open to debate, but two forms are commonly used in the literature depending on the main mechanism limiting the mode growth

at small island widths. In the first model, known as the transport model, the limitation is the result of an incomplete flattening of the pressure profile inside the island, as a consequence of a competition between the finite parallel transport time scale and the perpendicular transport time scale across the island.[52] In this case f is written as

$$f_{tra}\left(\frac{w}{w_{marg}}\right) = \frac{w^2}{w^2 + w_{marg}^2}, \tag{5.3}$$

where w_{marg} is the island width at which the growth rate has a maximum. In the second model, the polarization model, the limitation of the growth rate at small island widths is a consequence of the so-called ion polarization current, which is a result of the difference between the ion and electron response to island rotation.[53 54] For the polarization model f is written as

$$f_{pol}\left(\frac{w}{w_{marg}}\right) = 1 - \frac{w_{marg}^2}{3w^2}. \tag{5.4}$$

The value of w_{marg} for the transport model depends on the ratio of perpendicular to parallel transport, while for the polarization model it depends on the ion banana orbit width.[4]

ECCD inside the magnetic island stabilizes the mode by replacing the missing bootstrap current. For a Gaussian driven current density profile, this results in a contribution to the GRE as[49]

$$r_s\Delta'_{\mathrm{CD}} = -\frac{16\mu_0 L_q r_s j_{\mathrm{BS}}}{B_p \pi}\frac{\pi^{3/2}P}{w_{dep}}\frac{j_{CD,W}}{j_{\mathrm{BS}}}F_{CD}\left(w^*, \widehat{x}_{dep}\right), \tag{5.5}$$

where P is the ECCD power, $j_{CD,W}$ the peak driven current per watt injected power and w_{dep} the full e^{-1} deposition width. The function F_{CD} describes the dependence on ECCD beam width in terms of the relative island width $w^* \equiv w/w_{dep}$ and misalignment in terms of $\widehat{x}_{dep} \equiv \frac{r_{dep}-r_s}{\max(w,w_{dep})}$, where r_{dep} is the deposition position. The fitted expressions describing the separate effects from De Lazzari and Westerhof are used.[49 50] Strictly speaking, the expressions are averages over one island rotation period and correspond to the limit of fast island rotation. A finite rotation period in combination with a finite collisional time results in an oscillation of the Δ'_{CD} term, which however only becomes important for small island widths and rotation periods below 10 Hz.[55]

In the derivation of the GRE, it is assumed that magnetic islands are small, compared to the plasma minor radius, and that the plasma is adequately described using constant local plasma parameters. In the classical stability index and the bootstrap growth term finite island width effects are negligible.[51] Degradation of the plasma equilibrium by the island (see for instance[5]) has not been included. In the present work, the islands never reach their saturated island size and remain relatively small such that finite island width corrections are negligible. The calculations are stopped either when the island is fully suppressed or when the island locks. Asymmetric

islands result in equal current drive efficiency if power is deposited on the island O-point.[18] In this representation of the GRE, the effect of magnetic field curvature, ECRH and the effect of the driven current on the classical stability index are all neglected. Magnetic field curvature results in the Glasser-Greene-Johnson (GGJ) growth term, which is a factor $(\epsilon/q)^2$ smaller than the bootstrap term.[56,42] Also ECRH is expected to have only a marginal influence on island growth in ITER.[49] The non-inductively driven current can affect the classical stability index only on a resistive diffusion time scale and may be neglected on the short time scales of up to a few seconds occurring in the present work which is mainly determined by the locking time.[51,57]

5.2.2. Rotation

The rotation model (introduced in the form as used here by La Haye *et al*) assumes that the island width is small, resulting in negligible effects on the global magnetic equilibrium.[46] The island is approximated by a rigid body. Due to viscous coupling with the bulk plasma, the equilibrium toroidal rotation frequency ω_0 in absence of an island is a balance between momentum input from and loss to the bulk plasma. The rotating magnetic island induces wall currents that slow down the mode rotation, as described by the induced wall drag model from Nave and Wesson.[47] The rate of toroidal rotation change $\frac{d\omega}{dt}$ based on the viscous coupling to the bulk and the induced wall drag is written as[46,58]

$$\frac{d\omega}{dt} = \left(\frac{\omega_0}{\tau_{E0}} - \frac{\omega}{\tau_E}\right) - \frac{1}{mC_W\tau_{A0}^2\omega\tau_w}\left(\frac{w}{a}\right)^3, \tag{5.6}$$

where ω is the toroidal rotation frequency, τ_{E0} is the energy confinement time when no island is present, C_W is a geometrical factor that determines the drag induced by the wall, τ_w is a characteristic resistive time for the wall, τ_{A0} is an Alfvèn time describing the inertia of the magnetic island and a is the plasma minor radius.

In equation 5.6, the first term between brackets is the viscous coupling term. The two parts of this term represent the equilibrium momentum input, which is assumed to result in a constant rotation frequency in the absence of an island, and the loss of momentum which incorporates degradation of the plasma equilibrium. The confinement degradation by the island is described by a first order correction of the confinement time according to the Belt or Island model by the Chang *et al* , resulting in a decreased energy confinement time τ_E in the presence of an island, described by[59]

$$\tau_E = \frac{\tau_{E0}}{1 + C_M\frac{w}{a}}, \tag{5.7}$$

where C_M allows for the confinement degrading effect of the magnetic island on the local momentum input. Strictly speaking the momentum confinement time should be used. For ITER,

currently no good estimates exist, because theoretical knowledge of ITER rotation is not yet sufficient to predict the radial rotation profile.[60] Based on extrapolations from current tokamaks, approximating the momentum confinement time with the energy confinement time could result in an underestimation of the momentum confinement time.[60] A larger momentum confinement time would increase the momentum input by viscous coupling with the bulk plasma. As a consequence, mode locking would take a longer time.

The second term in equation 5.6 is the wall induced drag term introduced by Nave and Wesson.[47] The wall interaction is assumed to be slow ($\tau_w \omega \gg m$). The scaling of the island inertia, expressed in τ_{A0}, with the island width and plasma minor radius has been explicitly expressed, resulting in a formulation where C_W is a machine independent parameter.

5.2.3. Combined model and parameter values

The GRE provides the island width as a function of time and in its current form does not dependent on the island rotation frequency. The island width calculated based on this model is used as an input for the rotation model. The models are implemented in MathWorks Simulink and solved using a variable step ordinary differential equation solver (Runge-Kutta fourth order, with fifth order error estimate). Both the island width and the rotation frequency are solved with a relative accuracy of 10^{-6}.

Table 5.1.: *Simulation parameters and values.*

		2/1	3/2
Z_{eff} [61]		1.7	1.7
r_s [42]	[m]	1.55	1.3
$j_{BS}(r_s)$ [62]	$\left[\frac{\mathrm{kA}}{\mathrm{m}^2}\right]$	73	94
$T_e(r_s)$ [42]	[keV]	5.6	7.6
$B_p(r_s)$ [42]	[T]	0.97	1.07
$L_q(r_s)$ [42]	[m]	0.87	0.88
w_{marg} [5]	[cm]	2-6	2-6
w_{sat} [5]	[cm]	32	25
w_{dep} [51]	[cm]	2.4	3.7
$j_{CD,W}$ [51]	$\left[\frac{\mathrm{A}}{\mathrm{m}^2\mathrm{W}}\right]$	$1.32{\cdot}10^{-2}$	$1.22{\cdot}10^{-2}$

The simulation parameters for ITER scenario 2 are listed in table 5.1. The values of Bertelli *et al* for the deposition width w_{dep} and the driven current $j_{CD,W}$ are the result of TORBEAM simulations.[51 63] Values by Urso (ref.[42]) originate from simulations by Polevoi *et al.*[64] A range of 2-6 cm for the marginal island width is used, in accordance with Sauter *et al.*[5] Saturated island widths, as determined by Sauter *et al* based on an evaluation of the GRE terms, are used.[5]

Values for the rotation parameters are obtained from La Haye *et al.*[58] C_W and C_M are obtained from fits to DIII-D discharges for an ITER-like plasma equilibrium resulting in ITER-relevant values.

Flux surface averaging breaks down if one rotation period is in the same order as other time scales in the model. The rotation model breaks down if $\omega\tau_w \approx 1$, occurring at a frequency ω_{BD} which is approximately 5.3 rad/s and 8 rad/s for the 2/1 and 3/2 NTM respectively. The GRE model breaks down for even smaller rotation frequencies. The simulation is stopped when the breakdown frequency ω_{BD} is reached. At such low frequencies, a finite error field should also be taken into account, which is the final cause of the locking of the mode. However, this final phase is expected to be fast in comparison the the full slowing down phase such that its neglect does no introduce a significant error in the estimated locking time.

The highest efficiency for stabilization of both the 2/1 and the 3/2 NTM is obtained with beams injected from the Lower Steering Mirrors (LSMs) of the EC Upper Port Launcher.[51] With four ECCD launchers and four beams per LSM, a total of 16 beams with a combined injected power of 13.3 MW can be focused on the NTM.[23] In the remainder of this paper, ECCD is assumed to be continuous wave and perfectly aligned on the NTM resonant flux surface, unless stated otherwise.

5.3. Results

5.3.1. Bootstrap models

The two bootstrap models and the minimum and maximum value of the marginal island width provide four different values for the island growth rate $\frac{dw}{dt}$ at a given island width w. The dependence of the island growth rate on the island width, in absence of ECCD, is plotted for these four different cases in figure 5.2a and figure 5.2b for the 2/1 and 3/2 NTM, respectively. A solid vertical line in the figures indicates where the island width equals the locking island width w_{lock}, as determined by La Haye *et al.*[58]

Fast island growth results in larger islands and consequently a decreased locking time for island widths above the locking island width w_{lock}. Therefore, the model with the largest growth rate for widths larger than the locking island width will result in the shortest locking times and, conversely, the model with the lowest growth rate results in the longest locking times. The locking time results in a limit on the maximum allowed latency between island seeding and the start of ECCD deposition. Based on this consideration and figure 5.2, the polarization model with $w_{marg} = 2$ cm results in the shortest maximum allowed latencies and the transport model

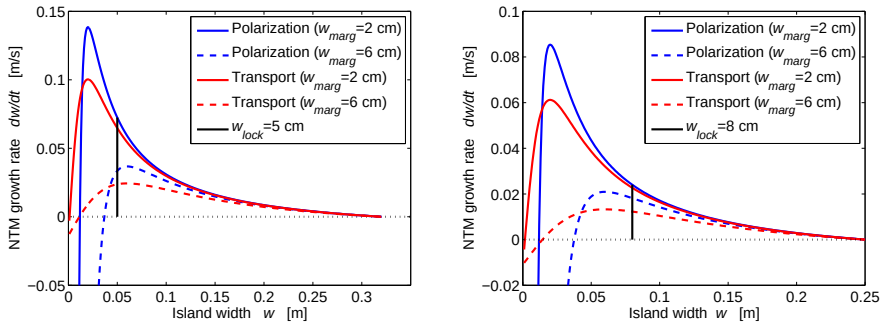

(a) 2/1 NTM **(b)** 3/2 NTM

Figure 5.2.: *Plot of the Generalized Rutherford Equation for the 2/1 and 3/2 NTM. Polarization (blue) and transport (red) models are both plotted with marginal island widths w_{marg} of 2 cm (solid lines) and 6 cm (dotted lines). The solid vertical black lines indicate locking island widths w_{lock}, which are 5 cm and 8 cm for the 2/1 and 3/2 NTM respectively.* [58]

with $w_{marg} = 6$ cm results in the longest maximum allowed latencies. The other models provide intermediate results.

As the rotation frequency drops, the locking island width decreases as well. In this case the polarization model with $w_{marg} = 2$ cm remains the hardest to stabilize for island widths larger than w_{marg}. However, for even smaller island widths the polarization model predicts island width decline without ECCD. Seed island widths smaller than 2 cm are therefore excluded from the simulations. Island widths smaller than 2 cm result in an increased maximum allowed latency for the transport models and therefore do not impose more stringent requirements on the maximum allowed latency.

The maximum allowed latency does not relate to the required energy or ECCD power for stabilization in a straightforward way. The required energy or power determines whether a rotating NTM can be stabilized (given a sufficiently short delay), while the maximum allowed latency determines whether the stabilization is fast enough to avoid mode locking.

5.3.2. Island width and rotation frequency

The island width and the rotation frequency as a function of time are shown in figure 5.3 for a 2/1 NTM. An island of 4 cm is seeded at $t = 0$ s with an equilibrium rotation frequency of 2640 rad/s and starts to grow in width and decrease in rotation frequency. Island growth is described by the polarization model with $w_{marg} = 2$ cm.

The time delay t_d between seeding and ECCD deposition start is varied in steps of 50 ms. As the delay is increased, a point is reached where the rotation frequency becomes zero before the mode is fully suppressed. When this happens the mode may lock in an unfavourable phase such

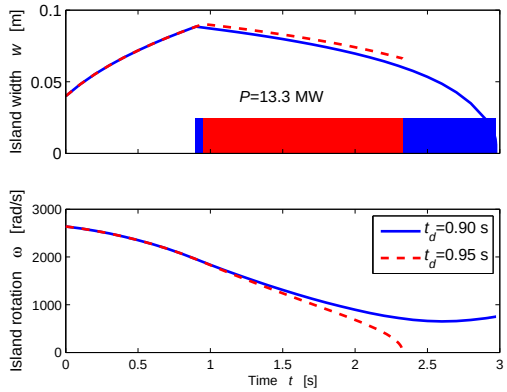

Figure 5.3.: *Simulation of the island width and rotation frequency of a 2/1 NTM with the polarization model with w_{marg} = 2 cm. At t=0 s a seed island with a width w_{seed}=4 cm is formed and starts to grow. The start of the deposition is 0.90 s and 0.95 s after island seeding, which is depicted by the solid and dashed curve respectively.*

that ECCD can no longer suppress the mode. In figure 5.3, full suppression is not possible with $t_d \geq 0.95$ s, but with a delay $t_d = 0.9$ s, the mode can be suppressed before locking. Therefore, for these settings, the total latency introduced between island seeding and the start of ECCD deposition on the mode should be smaller than or equal to 0.9 s. The longest time delay, for which a mode is suppressed without locking, is called the maximum allowed latency.

5.3.3. Maximum allowed latency and deviation in radial position

In the previous section, the maximum allowed latency is derived from time-dependent simulations of the island width and the rotation frequency. Due to the strong dependence of locking time on island width, the maximum allowed latency should be determined for all seed island widths individually. The polarization model with w_{marg} = 2 cm and the transport model with w_{marg} = 6 cm provide respectively the lower and upper limit to the maximum allowed latency. Figure 5.4 shows the maximum allowed latency for both models and both the 2/1 and 3/2 NTMs as a function of seed island width. The maximum allowed latency is determined with an accuracy of 50 ms.

The polarization and the transport model differ not only in the maximum allowed latency value, but also on the dependence of the value on the seed island width. The curve for the polarization model is flatter than the transport model curve, resulting from the localized peak in the island growth rate. The transport curve, on the other hand, is effected by the much broader peak in the island growth rate, resulting in a steeper curve.

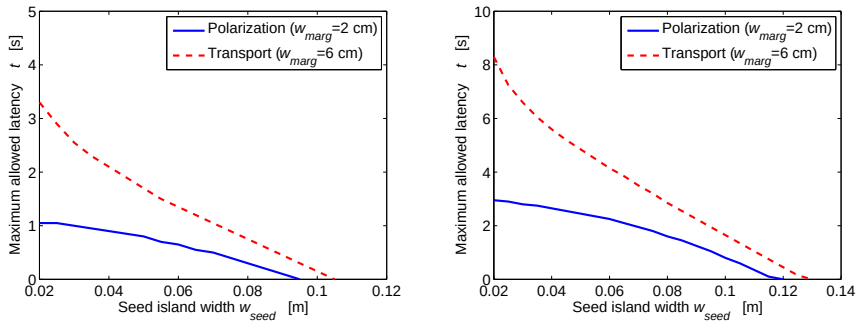

(a) 2/1 NTM **(b)** 3/2 NTM

Figure 5.4.: *Maximum allowed latency between seeding of the mode and ECCD deposition start. The plots show both the polarization (solid line) and the transport model (dashed line) with marginal island widths w_{marg} of respectively 2 cm and 6 cm for the 2/1 and 3/2 NTM.*

Figure 5.4 shows that the locking island widths w_{lock} of 5 cm and 8 cm for the 2/1 and 3/2 NTMs, as put forward by La Haye *et al*, are no absolute limits.[58] Even modes that have grown significantly larger or that are seeded at a larger island width than the locking width can still be fully suppressed before the mode locks provided that the maximum allowed latency is not exceeded. The maximum allowed latency is seen to reduce to zero for a 9.5 cm island in the case of the 2/1 mode and for a 12 cm island in the case of a 3/2 mode. Full suppression of the NTMs requires the control system latency to be well below the maximum allowed latency of 1.05 s and 2.95 s for the 2/1 and 3/2 modes, respectively, with the polarization model. Increasing the ECCD power to 20 MW, results in an increase of the maximum allowed latency by 300 ms and 800 ms for the 2/1 and 3/2 mode, respectively, for the polarization model. For both modes, the maximum allowed latency reaches zero for seed island widths 1.5 cm larger than with 13.3 MW. This improvement shows an approximately linear scaling with the available ECCD power, as expected based on the ECCD island growth rate. The effect of modulation on the maximum allowed latency is less than 100 ms and 350 ms for the 2/1 and 3/2 mode respectively.

The expressions for the ECCD efficiency as a result of misalignment from De Lazzari *et al* are used to evaluate the GRE for different misalignments $x_{dep} = r_{dep} - r_s$.[18] For full suppression of the mode, it is required that the island width growth rate is negative for all island widths. Based on this criterion, the maximum allowed deviation in the radial position is 7-10 mm for the 2/1 NTM and 5-16 mm for the 3/2 NTM. The limiting values are given by the polarization model with a marginal island width of 2 cm and the transport model with 6 cm respectively. La Haye *et al* derived values for the misalignment based on the criterion that the GRE should be negative for island widths larger than the locking width (5 cm and 8 cm for 2/1 and 3/2 resp.).[58]

This results in slightly larger estimates of the allowed misalignment (15 and 25 mm for 2/1 and 3/2 resp.), because the misalignment results in the largest reduction in ECCD efficiency for small island widths.[58] At the maximum allowable deviation, the simulations show a negligible decrease in maximum allowed latency. This is explained by the dependence of the efficiency on island widths. Only for small island widths the effect of misalignment on the ECCD efficiency becomes significant. However, for small islands the decrease in rotation frequency is small, leading to a negligible influence on the time it takes for islands to lock. Furthermore small enough islands maintain a finite rotation frequency. Consequently, the time it takes a growing island to lock, in the absence of ECCD, is unaffected by small islands, resulting in a negligible contribution on the related maximum allowed latency.

5.4. Discussion

Based on the model in which the a rotation model and the GRE are combined, the maximum allowed latency and deviation in radial position are derived for ITER scenario 2 parameters. The significance of these values depends on the chosen strategy for the NTM control system on ITER. In this section, the significance of the maximum allowed latency and radial deviation are considered for different choices of the control strategy, actuators and detectors. These three aspects of the control system, though being a necessary part of an integrated system, are treated separately in the following paragraphs.

A straightforward control strategy relies on only acting when an island is present: detect the mode, position the suppression mechanism and suppress the mode, repeating the scheme for every new occurrence of a mode. Most control schemes rely on this strategy with EC waves for mode suppression.[6 33 65 9] The maximum allowed latency and the radial deviation are derived for this strategy. However, one could also influence the plasma profile using preemptive methods, in order to prevent the formation of NTMs altogether.[5] On the opposite side of the spectrum, islands can be actively tracked and kept at a small size using continued stabilization of the mode.[29] Alternatively, one could drop the condition of suppression before mode locking and provide active or passive mechanisms to influence the mode phase.

ECCD is considered the main actuator for mode stabilization, suppression and preemptive control on ITER. Using mirrors, ECCD is deposited at the right position. Recent work by Collazos *et al* reports a steering mirror angle settling time of 2.5 s for angles equivalent to switching between different mode positions.[27] This settling time is longer than the maximum allowed latency for the 2/1 NTM. Therefore, without prior knowledge of the mode position, it is impossible to fully suppress the 2/1 mode before mode locking. This can be remedied by increasing the steering mirror performance or by making sure the required angle variation is small due to a

priori knowledge on the mode location. The control strategies based on preemptive stabilization and island tracking are not hampered by the mirror angle settling time, because they exploit a priori knowledge and require only small variations in the mirror angles, respectively.

The incorporation of a second actuator in the control loop could also drastically improve the possibilities of stabilization. If the phase of the island can be controlled, it can be changed to ensure maximum stabilization efficiency of ECCD. In this case mode locking is no longer a direct problem. Using additional magnetic fields, it should be possible to make the mode always lock in a phase that makes ECCD possible and efficient. This could be achieved either by a static error field or by active control with magnetic coils.

The radial misalignment should be smaller than the maximum allowed deviation in the radial position to guarantee full mode suppression. Radial misalignment results from uncertainty in the deposition position of ECCD and the uncertainty in the mode position as detected by a sensor. An accurate determination of the mode position is required if it is used to position the ECCD deposition. Electron Cyclotron Emission (ECE) and Mirnov coils are the main detectors for NTM presence in current experiments.[6 33 65 9] However, Mirnov coils are unable to resolve mode positions and the spatial resolution of ECE is limited by broadening effects, making it an open issue whether the mode position can be accurately determined.[24] Therefore one of both measurements needs to be supplemented with plasma equilibrium information to determine the mode position. This requires a very high accuracy of measurements used in the equilibrium reconstruction and an equally high accuracy in the equilibrium reconstruction itself. Using a different control strategy, can relax the accuracy requirements. For instance, tracking of small islands does not require full suppression and can therefore tolerate a higher radial misalignment. Experiments have also been done that use the same line-of-sight for ECE and ECCD, thereby compensating the error made in the determination of the mode position (i.e. ECE frequency of the island) by an exactly compensating error in ECCD positioning.[34] Note that detection, especially if it entails reconstruction of the plasma equilibrium, contributes to the control system latency as well.

5.5. Conclusions

In this paper, we have modelled the combined evolution of the island width and rotation frequency of NTMs in ITER from their initial seeding until their full suppression by ECCD or their locking to the wall. The main purpose of this work was to find the maximum allowed latency between the seeding of the NTM and the start of the ECCD such that the mode will be suppressed before it locks. If ECCD cannot be deposited sufficiently close to the island O-point, suppression is impossible. The ITER EC Upper Port Launchers cover only a 100° section in

toroidal angle. Suppression by ECCD of modes locked in an unfavourable position is therefore no longer possible and the locked modes will grow to a larger saturated width. In present experiments, locking of in particular the 2/1 NTM is seen to result in a disruption.[12] This is to be avoided at all cost in ITER.

The parameters used in the calculations are representative for the standard Q=10 H-mode scenario in ITER, also known as ITER scenario 2 (see table 5.1). The calculations assume an ECCD power of 13.3 MW injected into the plasma, which corresponds to the use of all 16 beam lines, from a single set of steering mirrors, at 1 MW originating from each gyrotron. The calculations show that the maximum allowed latency depends strongly on seed island width and on the marginal island width determined by the small island physics. When the seed island width exceeds 9.5 cm for the 2/1 or 12 cm for the 3/2 mode, locking becomes inevitable even when the ECCD is switch on immediately: i.e. the maximum allowed latency decreases to zero at these seed island widths. At a seed island width of only 2 cm the maximum allowed latency for the 2/1 mode is 1.05 s for the polarization model with $w_{marg} = 2$ cm. The corresponding maximum latency for the case of the 3/2 NTM is 2.95 s. The maximum allowed latency scales almost linearly with ECCD power as expected based on the ECCD growth rate. The effect of modulation on the maximum allowed latency is about 10 % for both modes.

In addition, this work has confirmed that the ECCD should be localized within about 1 cm from the radial position of the island O-point.[58] For larger deviations full mode suppression becomes impossible. A possible mismatch has, however little effect on the maximum allowed latency to prevent mode locking, which depends on the total time it takes to suppress the mode from an initial width of about 10 cm to just below the locking width (i.e. about 5 cm for the 2/1 mode). During this time a 1 cm mismatch will have little effect.

The total latency in a real-time NTM control system will consist of the sum of the times required: i) to identify the presence of a mode and its location in the plasma and ii) to calculate the appropriate steering angle to deposit the ECCD at this location and to actively steer the mirror to this required angle. Only the latter process, the steering of the ITER ECRH mirrors in the Upper Port Launchers, may take already up to 2.5 s which is more than the maximum allowed latency for the 2/1 mode in almost all of the relevant parameter space.[27]

In conclusion, mode locking has serious implications for any real-time NTM control system on ITER that aims to suppress NTMs by ECCD. The total latency in such a system should be reduced well below 1 s. Using extra actuators for control of the island phase or completely different control strategies (island tracking, preemptive stabilization) are options if the latency and radial accuracy requirements cannot be met for a control system relying on full mode suppression using ECCD.

Acknowledgments

This work, supported by the European Communities under the contract of association between EURATOM-FOM, was carried out within the framework of the European Fusion Program. The views and opinions expressed herein do not necessarily reflect those of the European Commission.

5.6. Concluding remarks for NTM sensing

In the paper, presented in this chapter, the maximum allowed latency and the required positioning accuracy are derived. The control objective is to fully suppress NTMs before mode-locking occurs. Different control strategies (such as preemptive ECCD or control of small island widths) would result in different requirements, which are not further addressed in this work. Although the power requirements for NTM suppression are highly dependent on the use of modulation, the paper shows the requirements on control latency are hardly influenced.[5] Therefore a basic control loop can do without modulated ECCD and therefore does not require detection of the island phase. As discussed in section 3.2.1, the detection of the island width can be used for more efficient power use as well. However, a basic control loop only requires the island position and a way to determine the presence of an NTM. Therefore the remainder of this work focusses only on the detection of the position of magnetic islands. A sensor that provides an accurate and timely measurement of the island location is essential for the success of a control loop for full NTM suppression. The requirements that are derived in this chapter are summarized in table 5.2.

Table 5.2.: *Requirements for NTM sensing for the 2/1 and 3/2 NTM based on the two growth models.*

		2/1	3/2
Polarization	Maximum allowed latency (2 cm)	1.05 s	2.95 s
w_{marg} = 2 cm	Required detection accuracy	7 mm	5 mm
Transport	Maximum allowed latency (2 cm)	3.3 s	8.3 s
w_{marg} = 6 cm	Required detection accuracy	10 mm	16 mm

6. ECE for NTM control on ITER[1]

H. van den Brand[1a,2], M.R. de Baar[1b,2], N.J. Lopes Cardozo[1a] and E. Westerhof[2]

[1] (a) Fusion Science and Technology Group (b) Control Systems Technology Group, Eindhoven University of Technology P.O. Box 513, 5600 MB Eindhoven, The Netherlands

[2] FOM Institute DIFFER - Dutch Institute for Fundamental Energy Research, Association EURATOM-FOM, Trilateral Euregio Cluster, P.O. Box 1207, 3430 BE Nieuwegein, The Netherlands

Abstract. ECE signals are simulated using realistic temperature profiles resulting from magnetic islands, with a time evolution of island width and rotation frequency. Using a video bandwidth of $B_v = 2$ kHz, an intermediate frequency bandwidth of $B_{IF} = 400$ MHz is required to achieve accurate detection of the island position using equatorial ECE for the 2/1 and 3/2 NTM. The detection latency is below the maximum allowed latency for seed island widths up to 11 cm and remains below 500 ms for all seed island widths. This does not take into account the time required for and accuracy of launcher positioning. ECE via the line-of-sight of the ECCD upper port launcher requires a spacing of 1 GHz for $B_v = 2$ kHz for the 2/1 and 3/2 NTM. Larger seed island widths are not detected for all angles, due to a decreased anti-correlation resulting from the detection of the flattened temperature profile inside the island. For the detected island widths, the detection latency remains below 500 ms and 1 s for the 2/1 and 3/2 NTM respectively.

[1]This chapter will be submitted as a paper to Nuclear Fusion. Appendix 6.A discusses additional algorithms not presented in the paper.

6.1. Introduction

Proving the technical viability of fusion power is the main goal of the ITER project. In order to achieve this goal the ITER tokamak (major radius $R_0 = 6.2$ m, minor radius $a = 2$ m) is being constructed near Cadarache, France.[21] Plasmas in ITER should demonstrate a fusion gain of $Q = 10$ for a period of 300 s. Achieving this goal requires control of detrimental instabilities such as the Neoclassical Tearing Mode (NTM), an MHD instability that reduces core temperature and thereby fusion yield and can result in a sudden loss of plasma (a disruption).[4] NTMs are global magnetic perturbations with poloidal and toroidal mode numbers m and n respectively, leading to a reconnection of magnetic field lines forming a magnetic island at the rational flux surface described by the safety factor $q = m/n$. A magnetic island is characterized by the full island width w, representing the amplitude of the mode, and its toroidal rotation frequency ω. The metastable NTM requires a seed island to become unstable and grows as a result of a self-enforcing lack of local bootstrap current. The current deficiency can be compensated through Electron Cyclotron Resonance Heating (ECRH) or Current Drive (ECCD).[43] Compared to other NTMs, the NTMs with mode numbers $m/n = 2/1$ and $m/n = 3/2$ will degrade the core temperature of ITER plasmas the most.[5] The presence of a magnetic island can be detected by its magnetic perturbation or the effect of the island on the temperature profile.

ITER will be equipped with four Upper Port Launchers (UPLs) which are able to suppress NTMs using ECCD.[22] Each UPL has two mirrors: the Lower Steering Mirror (LSM) and the Upper Steering Mirror (USM). The LSM has the highest efficiency for NTM suppression.[51] The Generalized Rutherford Equation (GRE), describing island growth, was used by La Haye *et al* and Van den Brand *et al* to assess the required accuracy in the ECCD deposition.[58,66] Stabilization of the mode is possible for misalignments in the order of 1 cm from the island O-point. In this paper, an accuracy of 5 mm or 7 mm for the 2/1 and 3/2 NTM respectively is required for the distance between the island O-point and the ECCD deposition position, determined from the average of the required accuracy in the equatorial plane at the low and high field side.

The maximum allowed latency is the longest time between the seeding of the mode and the start of ECCD that results in full suppression of the island before mode locking, i.e. stop of mode rotation. The latency of a complete control loop and therefore also the detection latency should remain below this value. The maximum allowed latency depends on the seed island width and the models and parameters used for island growth and island rotation. Two models for the maximum bootstrap growth rate at small island widths exist: the polarization model, describing the decreasing growth by the ion polarization current induced by the different response of ions and electrons to the island rotation, and the transport model, explaining the decreasing growth by an incomplete flattening of the pressure profile due a competition of parallel and perpendicular

transport. The maximum in the island growth rate is located at the marginal island width w_{marg}, expected between 2 and 6 cm for ITER.[5] The maximum allowed latency is smallest for the polarization model with $w_{marg} = 2$ cm and largest for the transport model with $w_{marg} = 6$ cm.[66] In the remainder of this paper, these limiting models will be referred to as the polarization and transport model respectively.

In this paper, the capabilities of Electron Cyclotron Emission (ECE) radiometry for an NTM control loop are assessed for a standard burning H-mode ITER plasma. ECE radiometry is part of the diagnostics on ITER, located in equatorial port 9.[24] The spatial dependence of the magnetic field and, consequently, the electron cyclotron frequency, allows for a spatially resolved measurements of the electron temperature.[40] The rotating magnetic island results in a periodic fluctuation of the electron temperature near the NTM rational surface, which can be detected with ECE. The required ECE radiometer settings needed to attain a localization of the island within the accuracy required for full NTM suppression are derived and used in simulations in which the detection latency is determined as a function of seed island width. Based on these settings the detection latency as a function of seed island width is determined using simulations. The measured locations require additional techniques to come to the launcher positioning required for accurate deposition. Examples are reconstruction of the magnetic equilibrium and ray tracing to determine launcher settings or detection of the deposition position using the same ECE diagnostic.[30,33] Accurate real-time determination of the mode position based on ECE measurements poses a challenging problem from a computational perspective. ECE measured along the line-of-sight of ECCD results in a straightforward relation between detected island location and deposition position. Due to the success on the TEXTOR tokamak in real-time NTM control using a line-of-sight ECE system and the implementation of a similar system in an ITER-relevant waveguide environment, it is worthwhile to assess line-of-sight ECE capabilities using the ITER UPL as well.[9,34]

The next section discusses how simulations of ECE for NTM suppression on ITER are set up and presents the detection algorithm by Berrino *et al*, that is used for the detection of the island location.[67] This section also shows how a realistic temperature perturbation is modelled based on the perturbation of the helical flux. The capabilities of ECE radiometry via the equatorial port are assessed in section 6.3. The line-of-sight ECE system is addressed in section 6.4. Limits of the simulations, possible improvements of the detection algorithm and extensions of the simulations are part of the discussion in section 6.5. The final section presents the conclusions.

6.2. Simulations and detection algorithm

This section discusses the NOn-Thermal ECE Code (NOTEC) which has been used to calculate ECE from ITER plasmas.[35] In particular, the implementation of magnetic islands in the equilibrium is discussed. Only thermal ECE is simulated throughout this paper and therefore non-thermal routines of NOTEC are not addressed, because of their negligible effect on the investigated range of ECE. Special attention is paid to the derivation of synthetic ECE measurements from the simulations. The algorithm used for detection of magnetic islands is detailed in the last subsection.

6.2.1. NOTEC

For thermal ECE, NOTEC solves the radiation transport equation

$$\frac{d}{ds}I(f) = j(f) - I(f)\frac{c^2 j(f)}{f^2 k_B T} \tag{6.1}$$

along the path of EC wave propagation in a toroidal geometry, where s is the path length, I the ECE intensity, f the ECE frequency, j the emissivity, k_B the Boltzmann constant and T the electron temperature.[19 35] The ECE path is traced back starting at the antenna to the EC emission region using the RAYS code.[36] The antenna is specified by three position coordinates X_a, Y_a, Z_a, a toroidal ϕ_a and a poloidal θ_a antenna angle, two transverse beam widths w_t and w_p, associated with the ϕ_a and θ_a directions respectively, and beam divergence in toroidal $\delta\phi$ and poloidal $\delta\theta$ direction. Up to 21 rays can be used to simulate an antenna pattern, where for every set of four rays a constant weighting is used, determined by the two-dimensional Gaussian beam intensity with widths w_t and w_p.The divergence of individual rays of a beam is given by $\Delta\phi = h/w_t\delta\phi$ and $\Delta\theta = l/w_p\delta\theta$ with h and l the toroidal and poloidal distance to the antenna centre.

The magnetic field in the poloidal plane is specified using two dimensional splines based on the ITER standard burning H-mode scenario 2.[68 64] Density and temperature are specified on the flux coordinates derived from the magnetic field topology. Equation 6.1 is solved using an emissivity j determined by iteratively solving the biquadratic equation for the refractive index using a predetermined number of harmonic and terms in the finite Larmor radius expansion.[40] NOTEC produces the ECE intensity for a set of specified ECE frequencies and can also provide the path travelled by individual rays.

6.2.2. Implementation of magnetic islands

As a result of magnetic islands, the temperature and density profiles no longer depend only on the flux coordinate, but on all three coordinates (r_c, θ, ϕ), where r_c is the plasma minor ra-

dius in cylindrical coordinates, ϕ the toroidal and θ the poloidal angle. The cylindrical radius $r_c = \sqrt{\frac{S(\psi_0,\sigma)}{\pi}}$ is determined by surface S enclosed by the equilibrium helical flux ψ_0, where σ indicates the position relative to the rational flux surface with $\sigma = -1$ for $r_c < r_{c,s}$ and $\sigma = +1$ for $r_c > r_{c,s}$, with $r_{c,s}$ the minor radius in cylindrical coordinates of the NTM rational surface. The helical flux is defined in such a way that it has a minimum at $r_{c,s}$. The presence of a magnetic island results in a perturbation of the helical flux given by

$$\widetilde{\psi} = \widetilde{\psi}(r_{c,s}) \frac{r_c^2}{r_{c,s}^2} \frac{\left(1 - \frac{r_c}{a}\right)^2}{\left(1 - \frac{r_{c,s}}{a}\right)^2} \cos\left(m\theta + n\phi + \xi_0\right), \tag{6.2}$$

with ξ_0 the phase of the NTM. Using the perturbation at the resonant surface $\widetilde{\psi}(r_{c,s})$, the extent of the mode is set to correspond with an island of width w, determined as an average of the width of the island on the low and high field side in the equatorial plane. This form of the perturbed helical flux takes into account the asymmetries in island extent and temperature perturbation at $r_c > r_{c,s}$ and $r_c < r_{c,s}$, as observed in experiments.[15 16 17] Previous analyses of the effects of NTMs on the temperature profile have neglected these asymmetries in the temperature perturbation.[33 52 69]

Density and temperature are assumed constant on the incompressible magnetic flux surfaces described by helical flux $\psi = \psi_0 + \widetilde{\psi}$ and σ. Due to the small effect of the NTM on the magnetic topology and the small density gradient in ITER, only the perturbation of the temperature has a significant effect on ECE.[64] The temperature inside the island is assumed constant due to fast transport, while transport outside the island is assumed to be unaffected, thus maintaining the equilibrium temperature gradients.

As a result of the incompressibility of the flux surfaces, the temperature can be related to the equilibrium temperature profile $T_0(r_c)$. Inside the island, the temperature T_{isl} is constant and equal to the temperature at the outer separatrix. A temperature difference ΔT results from temperature equilibration in the island. The temperature $T(r_c, \theta, \phi)$ at a position (r_c, θ, ϕ) outside the island is related to the equilibrium temperature profile by the helical flux. The temperature profile is therefore given by

$$\begin{aligned}
\psi > \psi_{sep} \text{ and } \sigma = +1 \qquad & T(r_c,\theta,\phi) = T_0\left(\sqrt{\frac{S(\psi(r_c,\theta,\phi),\sigma)}{\pi}}\right) \\
\psi < \psi_{sep} \qquad & T_{isl} = T_0\left(\sqrt{\frac{S(\psi_{sep},+1)}{\pi}}\right) \\
\psi > \psi_{sep} \text{ and } \sigma = -1 \qquad & T(r_c,\theta,\phi) = T_0\left(\sqrt{\frac{S(\psi(r_c,\theta,\phi),\sigma)}{\pi}}\right) - \Delta T \\
& \Delta T = T_0\left(\sqrt{\frac{S(\psi_{sep},-1)}{\pi}}\right) - T_0\left(\sqrt{\frac{S(\psi_{sep},+1)}{\pi}}\right)
\end{aligned}, \tag{6.3}$$

with ψ_{sep} the helical flux at the island separatrices and $S\ (\psi, \sigma)$ the enclosed area in the poloidal cross section by the flux surface defined by ψ and σ.

6.2.3. Synthetic ECE measurements

NOTEC is used to generate ECE spectra for a set of island widths and phases on a specified frequency range with steps of 50 MHz between individual points in the spectrum. The noise-free temperature oscillation due to a magnetic island is then found by subtracting the average temperature over all phases from a simulation with a specific phase. The amplitude of the temperature fluctuations associated with a 3 cm and 6 cm island are shown in figure 6.1. The radiation at the ECE frequency $f_{isl,act}$ with a minimum temperature fluctuation originates from the region around the island O-point and corresponds to the the actual island position. This position is determined from the noise-free simulations.

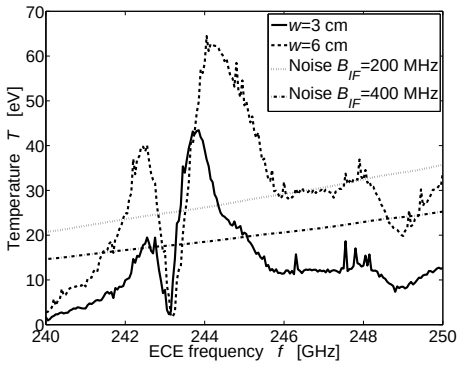

Figure 6.1.: *The temperature fluctuation as a result of 2/1 magnetic islands (3 cm solid, 6 cm dashed) and the noise level for B_v = 2 kHz (200 MHz dotted, 400 MHz dashed-dotted) for the second harmonic X-mode range 240-250 GHz.*

The thermal noise for an ECE radiometer is given by

$$\frac{\Delta T}{< T >} = \sqrt{\frac{2B_v}{B_{IF}}}, \tag{6.4}$$

where B_v is the video bandwidth and B_{IF} the intermediate frequency bandwidth.[20] The video filter limits the highest amplitude oscillation frequency available in the ECE signals and can be approximated by sampling at a fundamental step size $dt = 1/(2B_v)$. The intermediate frequency bandwidth B_{IF} determines the ECE frequency range that is measured in a single channel. The noise levels obtained with B_{IF} = 200 MHz and B_{IF} = 400 MHz are included in figure 6.1.

A synthetic measurement is obtained by combining ECE spectra of a magnetic island evolving over time with an ECE channel layout, determined by the radiometer settings B_v, B_{IF}, channels spacing and the number of channels. The model for island dynamics, including the evolution of the rotation frequency, as put forward in Van den Brand *et al* is used.[66] In this paper, the measurements at 50 MHz frequency intervals measured at frequencies f_{50} are assumed to represent the ECE signal for a frequency range $f_{50} - 25$ MHz $< f < f_{50} + 25$ MHz. At time instances t, the simulated ECE spectrum is interpolated for the island width $w(t)$ and phase $\xi_0(t) = \int_0^t n\omega(\tau)\mathrm{d}\tau$. Gaussian white noise with an amplitude specified by equation 6.4, using $B_{IF} = 50$ MHz, is added to all simulated ECE intensities for the frequencies f_{50}. The simulated ECE intensities I_{50} with thermal noise at frequencies f_{50} are added to form the channel intensity

$$I_{CH} = \int_{f_{cent}-B_{IF}/2}^{f_{cent}+B_{IF}/2} I_{50}(f)\mathrm{d}f, \tag{6.5}$$

where f_{cent} is the channel centre frequency and B_{IF} the intermediate frequency bandwidth.

6.2.4. Island position detection

As a result of the spatial dependence of the ECE frequency, magnetic measurements make it possible to map the ECE frequency to a position. Therefore in this paper, the island location is determined in terms of the ECE frequency where temperature fluctuations are minimal. The reconstruction of the actual position in (X, Y, Z)-coordinates could be avoided by the determination of the ECCD deposition location using the same ECE diagnostic.[33,34] Although providing an accurate mapping between the ECE measurements and actual position is a problem on its own, it is not further addressed in this paper. In this paper, the frequency $f_{isl,act}$ should be detected as the island location.

Location detection of magnetic islands in the ECE spectrum has been done using the anti-phase in temperature oscillations at opposite sides of the island (see for instance Hennen *et al* or Berrino *et al*) and the minimum in temperature fluctuations itself (see for instance Isayama *et al*).[9,67,70] The algorithm proposed by Berrino *et al* performed best for the ITER ECE simulations and is therefore used in the remainder of this paper.

The algorithm by Berrino *et al* calculates the second derivative to the frequency of the channel cross correlation.[67] First a moving average of N_{mov} measurements is subtracted to arrive at a temperature fluctuation

$$\delta T(t, j) = T(t, j) - \frac{1}{N_{mov}} \sum_{i=1}^{N_{mov}} T\left(t + (1 - i)dt, j\right) \tag{6.6}$$

for all channels j, where $T(t, j)$ is the measured electron temperature in channel j at time t. This fluctuation is normalized using the square root of a moving average over N_{avg} squares of the temperature fluctuation resulting in

$$\delta T_{norm}(t, j) = \frac{\delta T(t, j)}{\sqrt{\frac{1}{N_{avg}} \sum_{i=1}^{N_{avg}} \delta T^2 \left(t + (1 - i)dt, j\right)}}. \tag{6.7}$$

The correlation between the normalized fluctuation is calculated and averaged over N_{ac} measurements using

$$P(t, j) = \frac{1}{N_{ac}} \sum_{i=1}^{N_{ac}} \delta T_{norm} \left(t + (1 - i)dt, j\right) \delta T_{norm} \left(t + (1 - i)dt, j + 1\right), \tag{6.8}$$

defined at frequencies

$$f_P(j) = \frac{1}{2} \left(f_{cent}(j + 1) + f_{cent}(j)\right), \tag{6.9}$$

for $j = 1 \ldots N_{ch} - 1$ with N_{ch} the number of channels and $f_{cent}(j)$ the centre frequency of channel j. The first discrete derivative to the frequency

$$D_1(t, j) = \frac{P(t, j + 1) - P(t, j)}{f_P(j + 1) - f_P(j)} \tag{6.10}$$

is calculated for $j = 1 \ldots N_{ch} - 2$ at frequencies

$$f_{D_1}(j) = \frac{1}{2} \left(f_P(j + 1) + f_P(j)\right) \tag{6.11}$$

and used to calculate the second discrete derivative

$$D_2(t, j) = \frac{D_1(t, j + 1) - D_1(t, j)}{f_{D_1}(j + 1) - f_{D_1}(j)} \tag{6.12}$$

for $j = 1 \ldots N_{ch} - 3$. If the second difference D_2 exceeds a threshold $D_{2,thr}$, the anti-correlation indicates the presence of an island. The island is located at the zero crossing of D_1, which is found through linear interpolation using

$$f_{isl,det}(t) = \frac{D_1 \left(t, j_{max}\right) f_{D_1} \left(j_{max} + 1\right) - D_1 \left(t, j_{max} + 1\right) f_{D_1}(j_{max})}{D_1 \left(t, j_{max}\right) - D_1 \left(t, j_{max} + 1\right)}, \tag{6.13}$$

where j_{max} is the number of the largest D_2 entry.

The averages are implemented in MathWorks Simulink using digital filters $G(z) = \frac{K}{z-(1-K)}$, where $K = 1/(N+1)$ and $1/z$ is the unit delay operator. With $B_v = 2$ kHz, $N_{mov} = 40$ corresponds

to an average over 10 ms resulting in an average over an entire period for islands with a rotation frequency of 100 Hz and larger. For the normalization average and the average in the correlation, values of $N_{avg} = 80$ and $N_{ac} = 400$ are chosen. A proper choice for $D_{2,thr}$ ensures noise is not wrongly identified as an island. A value of $\frac{0.6}{(f_{cent}(2)-f_{cent}(1))^2}$ is found to yield only detection of magnetic islands.

6.3. Equatorial ECE

In this section, the detection of the location of the island using ECE radiometers in the equatorial plane is considered. The second harmonic X-mode is used, because it provides higher spatial accuracy than the first harmonic O-mode for equal noise levels. In ITER the equatorial ECE antenna is located at major radius $R = 8.5$ m and height $Z = 0.76$ m.[24] A value of 6 cm FWHM is used for both beam widths which provides an upper estimate to the expected beam width and ensures that beam divergence is negligible.[71]

Note that for a control loop for positioning based on equatorial ECE, methods that determine the deposition position set point, as well as the mirror actuator realizing the set point, should introduce no or small errors in order to achieve the required accuracy. For instance, the relativistic shift alone has a larger influence (1.1 GHz on average) than the required accuracy (200 Mhz for 2/1 NTM, see section 6.3.1) and should therefore be compensated by such methods. Delays introduced by reconstruction and ray tracing codes should also be considered. Reconstruction of the equilibrium and ray tracing or a detection of the deposition position are both considered, but have not yet been demonstrated in real-time ITER-relevant applications.[30 33] The latency and accuracy for the actual deposition to start are therefore not further addressed in this work.

First an appropriate ECE spacing is derived for both 2/1 and 3/2 magnetic islands, based on the required positioning accuracy. This spacing is used to generate synthetic ECE data, to which the detection algorithm is employed to determine the detection latency.

6.3.1. ECE spacing

A video bandwidth $B_v = 2$ kHz is used, which suffices for the detection of 3/2 and 2/1 rotating islands, based on the equilibrium toroidal plasma rotation frequency ω_0 by La Haye *et al* (420 Hz for 2/1 and 578 Hz for 3/2).[58] Larger values for B_v have been reported in literature.[69]

An accuracy Δr of 7 mm for 2/1 and 5 mm for 3/2 magnetic islands in ECCD deposition position should be achieved to ensure full NTM suppression is possible.[66] Assuming that the spatial dependence of the magnetic field $B \propto \frac{1}{R}$ results in the only unknown error contribution, the required accuracy in the ECE frequency of the island is $\Delta f = f_{rs}\frac{\Delta r}{R_s}$, with f_{rs} the ECE frequency and R_s the major radius at the rational flux surface. This results in an accuracy requirement of

200 MHz and 150 MHz for the detected ECE frequency of the 2/1 and 3/2 magnetic islands respectively. If additional errors are introduced in the process of mapping a detected ECE frequency of an island to the ECCD deposition position, more stringent accuracy requirements should be imposed on the island detection.

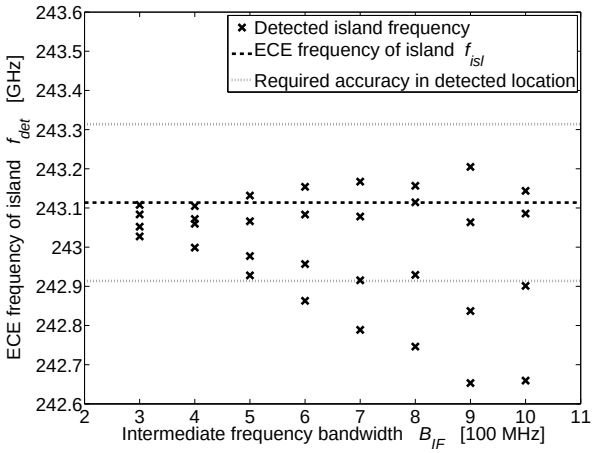

Figure 6.2.: *The detected ECE island frequency as a function of B_{IF} for a magnetic island of 3 cm rotating at 600 rad/s. The centre frequency of the first band is located at* $240\ GHz + (c + 0.5)B_{IF}$*, where c is an offset value of 0, 1/4, 1/2 or 3/4.*

Figure 6.2 shows the detected ECE frequency for a 3 cm island as a function of intermediate bandwidth B_{IF}. The channel spacing is assumed equal to B_{IF} and ECE is collected in a range from 240-250 GHz. The figure shows that at $B_{IF} = 400$ MHz the island position is detected sufficiently accurate regardless of the spacing offset. For intermediate frequency bandwidths below 300 MHz, the island is no longer detected. This is caused by the thermal noise, illustrated in figure 6.1.

The detection algorithm assumes the temperature fluctuation is the result of the rotating island. However, because the noise at ECE frequencies below 243 GHz is comparable to the temperature fluctuation of a 3 cm island, an offset towards lower ECE frequencies is observed in figure 6.2. The temperature fluctuation for larger islands is well above the noise level.

A spacing of $B_{IF} = 400$ MHz also provides satisfactory results for 3/2 magnetic islands detection. In fact, a spacing of 500 MHz would suffice as well but would require two different ECE channel layouts to detect both modes. For the 3/2 magnetic islands, no shift in the island ECE frequency is observed, due to a smaller asymmetry in the helical flux perturbation. Additional simulations indicate that a doubling of the video bandwidth to 4 kHz increases the noise level such that 3 cm islands are no longer detectable for the 2/1 NTM. If B_{IF} is also increased by a

factor 2 to maintain the noise level, detection of 3 cm islands is possible, but the required accuracy in the detected position is no longer maintained. The detection of islands of 2 cm cannot be guaranteed with the chosen 400 MHz bandwidth.

6.3.2. Island detection example

NOTEC simulations of ECE spectra as a function of island width and phase are combined with a temporal evolution of island width and island rotation following the model by Van den Brand *et al.*[66] Figure 6.3 shows the evolution of island width, island rotation, ECE signals and detected island location. A channel spacing and intermediate frequency bandwidth of 400 MHz is used, yielding channel centre frequencies ranging from 240.2 GHz to 249.8 GHz. The video bandwidth is 2 kHz. Section 6.3.1 explains the choice of ECE channel layout. Only a limited part of the channels is depicted.

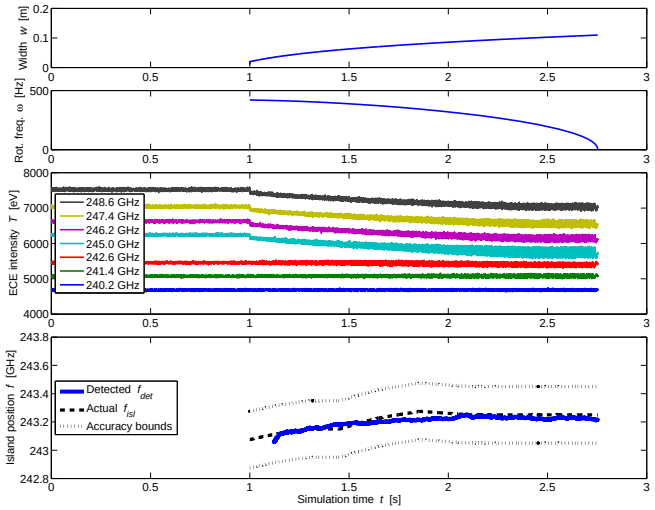

Figure 6.3.: *2/1 NTM seeded with 2 cm at 1 s, growing in accordance with the polarization model with* $w_{marg} = 2$ *cm. The simulation is stopped when the mode locks. From top to bottom, the boxes show island width, toroidal rotation frequency, simulated ECE signals and the actual and detected island position. The number of depicted ECE channels is limited to 7 of the 25 available channels to increase readability of plot.*

An island of 2 cm is seeded at $t = 1$ s. Island growth is simulated until the island locks, assuming a polarization model for the island growth. As the island grows the average temperature in the plasma core decreases and the temperature fluctuations increase in amplitude. Temperature fluctuations due to the island are larger near the island and larger at radii smaller than r_s, corre-

sponding to larger ECE frequencies. This is a result of the imposed asymmetry on the perturbed helical flux and is consist with experimental observations.

For 2/1 magnetic islands, the island location $f_{isl,act}$, indicated by a dashed black line in the bottom plot, shifts to higher frequencies as the island width increases, as is expected based on the shift of the island O-point. This difference amounts to 200 MHz, going from 2 to 9 cm island widths, and needs to be compensated, because it is on the order of the required accuracy. The accuracy of $f_{isl,act}$ is limited due to the limited frequency step size of 50 MHz in the underlying ECE spectrum simulations. The dotted lines show the upper and lower bound on the detected island position to maintain an estimate within 200 MHz, which ensures the required deposition accuracy is reachable. The ECE frequency $f_{isl,det}$ is determined using the algorithm presented in section 6.2.4. The island is detected 111 ms after seeding and the detected position remains within the accuracy bounds.

6.3.3. Detection latency with equatorial ECE

In section 6.3.1, a video bandwidth B_v of 2 kHz and an intermediate frequency bandwidth B_{IF} of 400 MHz are shown to be required for accurate detection of 2/1 and 3/2 magnetic islands. Using an ECE channel layout with centre frequency ranging from 240.2 to 249.4 GHz and 240.2 to 259.4 GHz for the 2/1 and 3/2 mode respectively, the detection latency is determined. The detection latency is defined as the time difference between island seeding and the time at which the detected island location is within the required accuracy of 200 MHz or 150 MHz for the 2/1 and 3/2 NTM respectively and remains accurate for the remainder of the simulation run. The detection latency is determined for growing islands with either the polarization model or the transport model. The seed island width is varied from 2 cm up to 11 cm for 2/1 NTMs and up to 13 cm for 3/2 NTMs. Each simulation is repeated 15 times with different random noise. The mean, minimum and maximum detection latencies as a function of seed island width are shown in figure 6.4

Figure 6.4 shows that the island position is detected within the maximum allowed latency for seed island widths up to 8.5 cm and 11 cm for the 2/1 and 3/2 NTM respectively for the polarization model. As the seed island width increases, the detection latency increases due to the reduced performance of the algorithm for larger island widths. Large islands result in regions of constant temperature leading to a decrease of temperature fluctuations in the ECE channels, which in turn decreases the highest anti-correlation between adjacent channels. For both the 2/1 and 3/2 NTM, the detection latency with the transport model is longer for small island widths. Islands of 2 cm are below the thermal noise level and need to grow in size to be detected, which takes longer for the transport model. Detection is fastest for seed island widths of 5 cm and all seed islands are detected within 500 ms.

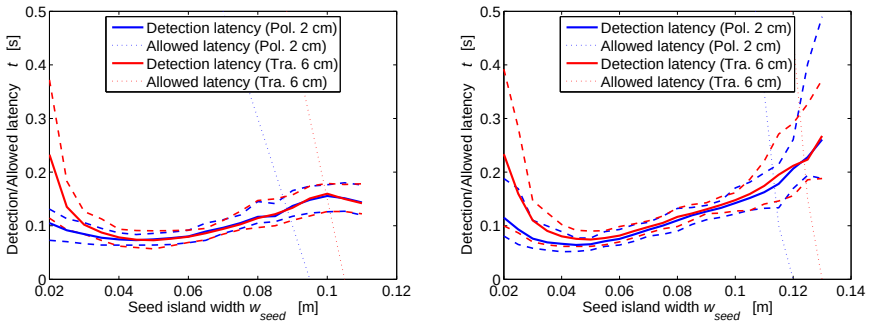

(a) 2/1 NTM **(b)** 3/2 NTM

Figure 6.4.: *Detection latency for island position using equatorial ECE. The figures show the mean detection latency (solid) and the shortest and longest detection latency (dashed) determined from 15 runs with different noise. Island growth is simulated using the polarization model (blue) and the transport model (red). The maximum allowed latency is plotted as reference (dotted).*[66]

6.4. Line-of-sight ECE

If equatorial ECE is used to determine the island position, both the relation between island ECE frequency and flux surface and the relation between the launcher angle and the flux surfaces should be accurately known. Using line-of-sight ECE, these relations are the same, i.e. for equal frequencies the ECE waves propagate along exactly the same path as the ECCD waves. In practice using exactly the same frequencies is impossible, but the paths remain nearly equal for variations of 10 GHz and larger. However, the orders of magnitude difference between ECE and ECCD power poses a technical challenge addressed for a system on ITER by Bongers *et al.*[34] Use of feedback based on an inline detection of the island ECE frequency to steer the EC mirror is demonstrated on the TEXTOR tokamak by Hennen *et al.*[9] This section investigates the capabilities of a line-of-sight ECE system for ITER.

The LSM of the UPLs are the preferred choice for a line-of-sight ECE system. The LSMs have a fixed angle $\beta = 18°$ and a variable angle α and are positioned at major radius $R = 6.9$ m and height $Z = 4.18$ m.[72] The angles α and β are related to the antenna angles θ_a and ϕ_a by $\theta_a = -\arcsin(\cos\beta \sin\alpha)$ and $\phi_a = \arctan(\tan\beta / \cos\alpha)$. The focussing of the beam is simulated using a toroidal and poloidal beam width of $w_t = 3.25$ cm and $w_p = 1.5$ cm and a toroidal convergence of 1°. The same beam settings are used by Bertelli *et al* to approximate the Gaussian beam profile near the 170 GHz EC resonance.[73] The detection capabilities of a line-of-sight ECE system on one UPL are addressed in this section.

First the relation between launcher angle α and the location of the magnetic island is determined. A channel layout is determined for the 2/1 NTM and 3/2 NTM based on a scan of multiple angles. In the final subsection, the detection latency for different seed island widths is evaluated for the 2/1 and 3/2 NTM.

6.4.1. Island position and required accuracy

For different angles α, the intersections between the ECE line-of-sight and the NTM rational flux surfaces are at different locations, associated with different magnetic field strengths and, consequently, different ECE frequencies. With a single ray simulation with NOTEC, the ECE frequency that has an emission peak at the NTM rational flux surface is determined for all angles α. Using this approach an approximate position of the rational flux surface, expressed in terms of ECE frequency, is found. However, when the full antenna pattern is taken into account the island location can also be determined from the ECE frequency at which a minimum of the temperature fluctuation is found. For a 2/1 NTM, both the location based on the minimum in the temperature fluctuation and the location of the rational flux surface from a single ray simulation are shown as a function of α in figure 6.5. An offset between the NTM rational surface and the actual island position is visible, but the dependency on launcher angle α is the same. The offset is the result of the antenna pattern and the effect of the finite island width on the temperature profile. At the optimal angle $\alpha_0 = 41.2°$ and $\alpha_0 = 50.7°$, 170 GHz is emitted from the region near the island O-point of a 2/1 and 3/2 NTM respectively and ECCD is deposited at the island O-point.

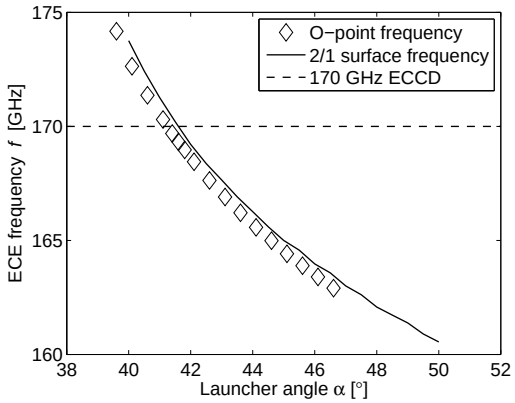

Figure 6.5.: *Island location as a function of launcher angle α. The black diamonds indicate the ECE frequency with minimum temperature fluctuation, which originates from the region near the island O-point. The black line indicates the ECE frequency at the 2/1 rational flux surface for single ray emission. For reference, the 170 GHz ECCD frequency is shown.*

A radial offset of 7 mm and 5 mm, for the 2/1 and 3/2 NTM respectively, is allowed, while maintaining full suppression capabilities.[66] The offset between the position of 170 GHz absorption and the rational surface is evaluated for angles α near the optimal angle α_0. Based on single ray simulations, it is found that an error in the launcher angle $|\Delta\alpha| < 0.4°$ results in sufficient positioning accuracy for the 2/1 NTM. For the 3/2 NTM, an accuracy of $|\Delta\alpha| < 0.15°$ is required.

Figure 6.5 indicates that if $\Delta f = 170\,\text{GHz} - f_{isl,det}$ is larger than zero $\alpha < \alpha_0$, while for Δf smaller than zero $\alpha > \alpha_0$. This indicates that based on the difference Δf the required control action for the launcher angle α for ECCD deposition in the island is discernible, based on noise-free simulations. Whether a noisy detected island location can also serve as control signal for ECCD control is assessed in the following subsections. This is tested based on *three* criteria: i) Δf is zero indicates no control action and is only allowed in the range $|\alpha - \alpha_0| < 0.4°$ and $|\alpha - \alpha_0| < 0.15°$ for the 2/1 and the 3/2 NTM, ii) a control signal Δf should exist for all angles, indicating that the island should be detected and iii) for $|\Delta\alpha|$ larger than 0.4° and 0.15° for the 2/1 and 3/2 NTM respectively a larger $|\Delta\alpha|$ should result in a larger value of $|\Delta f|$. The last condition requires every value of Δf to occur only for one specific α, therefore also imposing a derivative $\frac{\partial \Delta f}{\partial \alpha}$ with, based on figure 6.5, a negative value for all α.

6.4.2. ECE spacing

Using $B_v = 2\,\text{kHz}$, an ECE channel layout is derived that should fulfill the three conditions posed in subsection 6.4.1 A band of 1 GHz around 170 GHz is cleared. In practice, stray radiation in this range, coming from ECCD, could damage the ECE radiometers and should be suppressed. Therefore the ECE channels on opposite sides of the cleared bandwidths have centre frequencies $169.5\,\text{GHz} - B_{IF}/2$ and $170.5\,\text{GHz} + B_{IF}/2$. The channel spacing is chosen equal to the intermediate frequency bandwidth and emission from 160 GHz to 170 GHz is collected. Figure 6.6 shows the detected island position for a 3 cm island rotating at 600 rad/s. For both the 2/1 and 3/2 NTM, the detected island location, in terms of the ECE frequency, is depicted as a function of the launcher angle α for varying intermediate frequency bandwidths B_{IF}.

For the 2/1 NTM, detected island positions are shown for intermediate frequency bandwidths of 1 GHz, 1.25 GHz and 1.5 GHz. Although all three intermediate frequency bandwidths can be used, a 1 GHz bandwidth is preferred because the detected island locations show the largest dependence on the launcher angle α. This eases the design of an appropriate feedback action. For the 2/1 NTM, 2 cm islands are detectable using this channel layout

Simulations with intermediate frequency bandwidths of 900 MHz, 1 GHz and 1.5 GHz are shown for the 3/2 NTM. An intermediate frequency bandwidth of 1.5 GHz cannot be used, because at an angle $\alpha = 50.4°$ the difference Δf is zero, although the angle is not optimal. Both 900 MHz and 1 GHz are possible choices for B_{IF} that meet the conditions put forward in the

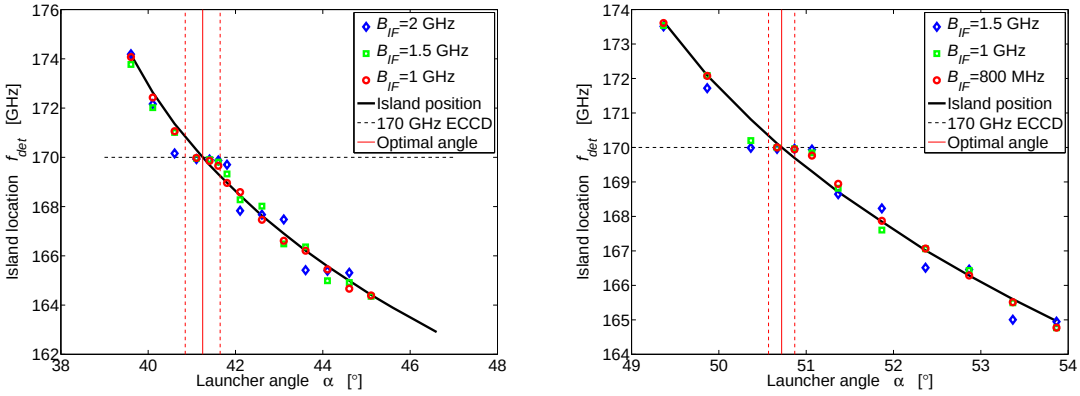

(a) 2/1 NTM **(b)** 3/2 NTM

Figure 6.6.: *Detected island frequency as a function of launcher angle α. The 2/1 NTM is shown in the left plot and the 3/2 NTM is shown right. The solid black line indicates the noise-free location of the island $_{isl,act}$, which is depicted for the 2/1 NTM with black diamonds in figure 6.5. The 170 GHz ECCD frequency is indicated using a dashed horizontal line. The optimal launcher angle α_0 and the accuracy bounds are shown as red solid and red dashed vertical lines respectively. The points correspond to detected island position as a function of α for different intermediate frequency bandwidths B_{IF}, determined from an average over 3 runs with different noise for a 3 cm rotating at 600 rad/s.*

previous subsection. An intermediate frequency bandwidth of 1 GHz is chosen, because it has a better signal-to-noise ratio and results in a similar channel layout for both NTMs. Islands of 2 cm are not detectable for all angles for the 3/2 NTM.

With $B_{IF} = 1$ GHz, a video bandwidth of 4 kHz results in detected positions that suffice the conditions for feedback control for both the 2/1 and 3/2 NTM. The bandwidth is larger than the intermediate frequency bandwidth determined for equatorial ECE, due to the tangential beam path of line-of-sight ECE that has a smaller difference in the radial position for the same frequency difference.

6.4.3. Detection latency of a line-of-sight ECE system

A channel spacing equal to the intermediate frequency bandwidth of $B_{IF} = 1$ GHz is used with a video bandwidth $B_v = 2$ kHz. As a result of the region of 1 GHz around 170 GHz in which no radiation is detected, the centre frequencies of the channels consists of a range from 161 to 169 GHz and from 171 to 179 GHz. The mean, minimum and maximum detection latency, determined from 15 runs with different noise, are shown in figure 6.7 for four fixed launcher

angles α. The island growth is modelled for different seed island widths using the polarization model.

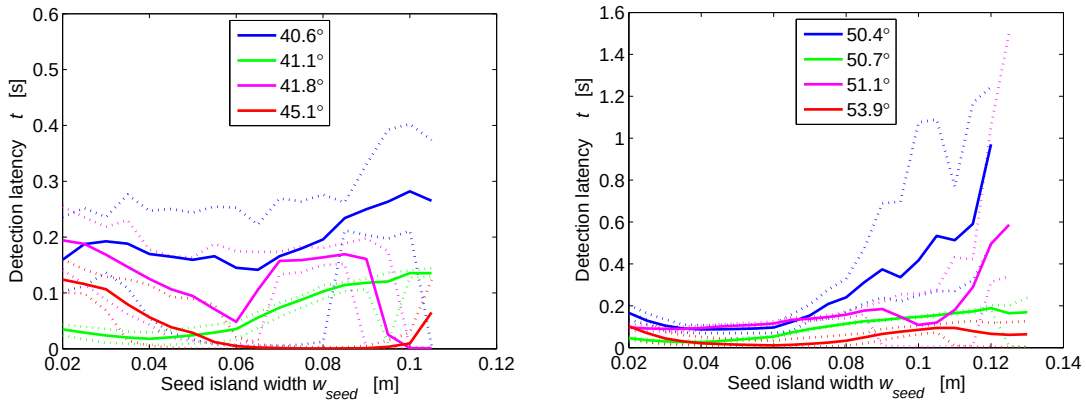

(a) 2/1 NTM **(b)** 3/2 NTM

Figure 6.7.: *Detection latency for 2/1 and 3/2 island location using line-of-sight ECE. Island growth is modelled using the polarization model. The detection latency determined for four angle is shown, with the mean detection latency (solid line) and the upper and lower limits (dotted), determined from 15 runs with different noise.*

Figure 6.7 shows that detection of all islands is not successful for angles α of 40.6° and 41.8° for the 2/1 NTM and for angles α of 50.4° and 51.1° for the 3/2 NTM. At larger island widths, anti-correlation of the ECE channel is reduced by a flattened temperature profile in vicinity of the island. For the optimal angles $\alpha_0 = 41.2°$ and $\alpha_0 = 50.7°$, for the 2/1 and 3/2 NTM respectively, this is not observed, because near the island the channels are spaced farther apart as a result of suppressed ECE in the frequency range from 169.5 GHz to 170.5 GHz. For the larger angle $\alpha = 45.1°$ for the 2/1 NTM, all islands are detected regardless of seed island width. For larger angle difference $\Delta\alpha$, the beams are less tangential to the 2/1 rational surface. This results in a larger difference in radial position for the same frequency difference, compare to a tangential beam at smaller $\Delta\alpha$, and, consequently, a larger frequency range that is located outside the island. For all widths for which the island is detected, the detection latency remains below 500 ms for the 2/1 NTM and 1 s for the 3/2 NTM.

Simulations using island growth modelled with the transport model are conducted as well. These show similar trends as the polarization model. Due to the slower growth, detection of islands up to 6 cm and 6.5 cm is possible for the 2/1 NTM with launcher angles α of 40.6° and 41.8°. For both growth models, the detected island frequencies suffice the conditions for feedback control stated in subsection 6.4.1.

6.5. Discussion

The simulations presented in this paper include what are expected to be the relevant dynamics for NTM detection using ECE. The physics that was excluded from the simulations is discussed in this section. The limitations of the island location sensor are also discussed, focussing on possible improvements of the algorithm. The last paragraph is devoted to the extension of simulations to encompass an entire ITER NTM control loop, to fully assess latency, accuracy and compatibility of the different components.

As a result of the limited validation of the Generalized Rutherford Equation at small island widths and limited knowledge on ITER rotation, no definite model for island growth and rotation on ITER exists. Therefore the simulations presented in this paper work with the limiting growth models within the expected parameter range for NTMs on ITER. As a result, the simulations are expected to give a good representation of the island growth and rotation. The required accuracy and maximum allowed latency, used throughout this paper, are also dependent on the models for NTMs on ITER. For a discussion of their relevance in the NTM control problem on ITER see Van den Brand *et al.*[66]

Throughout this paper, the same ECE channel layout is used for island growth modelled with the polarization and transport model. This layout is derived based on the accuracy requirements for the polarization model. For the transport model, the required deposition accuracy is lower, justifying a different layout, which could result in increased performance. Since current experiments are unable to distinguish which island growth model is most accurate the more stringent requirements imposed by the polarization model are used.

The used ECE channel layout is idealized, assuming that there is no overlap in ECE frequencies detected with adjacent channels. The video filter is approximated by sampling at time intervals $1/(2B_v)$ to ensure frequencies up to B_v are present in the measured ECE signals. In practice, radiometers show a lower gain for ECE frequencies and video frequencies near the edge of the band. ECE frequency overlap between neighbouring ECE channels is also observed in practice. However, these effects take place in relatively small parts of the channel ECE and video bands and would therefore not exert a large influence on the simulated signals.

Only the thermal noise by the uncorrelated ECE has been taking into account. Other noise sources such as edge density fluctuations, turbulent temperature fluctuations or transients such as sawteeth or ELMs are not incorporated. The result of these effects on the ITER equilibrium might be studied in separation by examining how they influence EC wave propagation and inferring the effect on ECE in particular. At this moment no conclusions can be drawn regarding the influence of other noise sources on island detection using ECE.

The detection algorithm showed a minimum in detection latency and increasing latencies for both smaller and larger seed island widths. The small perturbation at small islands is hard to detect in the noise background and the larger islands reduce the fluctuations due to temperature equilibration in a larger frequency range, thereby decreasing the correlation signals. Both increases of the detection latency could be counteracted by a multi-scale detection method. By using larger intermediate frequency bandwidths, the signal to noise ratio improves and small islands can be detected earlier. Larger intermediate frequency bandwidths also imply a larger channel spacing, thereby collecting less of the equilibrated temperature inside the island relative to the ECE detected outside the island. A drawback is the reduced spatial accuracy in detected position, which would still require the lower intermediate frequency bandwidth and hence incorporation of multiple intermediate frequency bandwidth scales in the algorithm. For larger island, the temperature fluctuation is bigger and could result in detection within the required accuracy for larger intermediate frequency bandwidths. A direct digitized radiometer system with a real-time tunable intermediate frequency bandwidth, as designed by Bongers *et al*, could be beneficial for multi-scale detection as well.[74]

Detection of the island position with the line-of-sight ECE system is shown for several angles. However, as soon as the position is detected the angle α should be changed to position ECCD at the island O-point. If the island position sensor could provide a signal on a timescale faster than the launcher movement, it could be used for feedback on the launcher angle α. Instability of the control loop could be the result if movement of the launcher is faster than the detection. Care should be taken to avoid this situation.

The simulations presented in this paper address only two components of a control loop for NTMs: the plasma with the island and the detector. The steering mirror, which serves as actuator, could be incorporated in a control loop simulation using the dynamics of the first prototype as described by Collazos *et al*.[27] The design of a controller is a more challenging exercise, which could entail modelling of additional diagnostics (in case of reconstruction). Based on the line-of-sight ECE system it is straightforward to define the minimization of $\left|f_{isl,det} - 170\ \mathrm{GHz}\right|$ as a control objective, but implementation of a suitable controller still requires an analysis of the system from a control perspective.

6.6. Summary and conclusions

The ray tracing and EC emission code NOTEC is used to simulate ECE coming from an ITER plasma containing a magnetic island. The perturbed temperature profile not only takes into account the flattening of the temperature inside the island, but also the perturbation of the flux surfaces caused outside the island. The flux surface perturbation as well as the temperature

perturbation itself are asymmetric around the island flux surface, thereby providing a realistic temperature perturbation that is consistent with experimental observations. Simulated ECE spectra, measured at frequencies 50 MHz apart, are combined in ECE channels and thermal noise is added based on the intermediate frequency and video bandwidths. A set of ECE spectra with varying island width and phase are combined with models for the evolution of the island width and rotation to arrive at time dependent ECE signals. The actual island location, indicated by the frequency of minimum temperature fluctuation in the noise-free spectra, should be accurately detected for NTM control. An algorithm by Berrino *et al* is used for island detection.[67]

For both equatorial ECE and a line-of-sight ECE system, the required ECE channel layout to attain a detection accuracy of 5 mm and 7 mm for the 2/1 and 3/2 NTM is investigated, which is equal to the required deposition accuracy for full suppression. A video bandwidth of 2 kHz is used which suffices for the detection of the 2/1 and 3/2 NTM based on a model for mode rotation by La Haye *et al*.[46] The detection latency is determined for seeded islands, growing in accordance with the polarization model and the transport model for the saturation of the bootstrap island growth at small island widths.

Using equatorial ECE, a sufficient detection accuracy for 3 cm islands is attained with a 400 MHz intermediate frequency bandwidth for both the 2/1 and 3/2 NTM. The channel spacing is taken equal to the intermediate frequency bandwidth. For small islands the temperature oscillation is near the noise level, while for larger islands ECE channels are located partially in the island, thereby decreasing the detected temperature oscillations. As a result, detection latency is lowest for 5 cm islands. Islands of 2 cm are not detectable with the chosen spacing as well. Use of a video bandwidth of 4 kHz no longer leads to detection of 3 cm islands. Island detection within 500 ms is possible for all seed island widths and the detection latency remains below the maximum allowed latency for seed island widths of 8.5 cm and 11 cm for the 2/1 and 3/2 NTM respectively.

For a line-of-sight ECE system, an accuracy in the launcher angle α of $|\Delta\alpha| < 0.4^\circ$ and $|\Delta\alpha| < 0.15^\circ$ is required for the 2/1 and 3/2 NTM respectively to ensure that ECCD is deposited sufficiently close to the island O-point for full suppression. The frequency difference Δf between 170 GHz and the island ECE frequency should serve as a control signal that is to be minimized. Therefore the sign and size of Δf should relate to a consistent control action for the launcher angle α, with $\Delta f = 0$ only when the launcher is positioned accurately for full NTM suppression. Based on these conditions, an intermediate frequency bandwidth of 1 GHz, which is taken equal to the channel spacing, is found for both the 2/1 and 3/2 NTM for detection of 3 cm islands. A frequency band of 1 GHz around the 170 GHz ECCD frequency is filtered to prevent detection of stray radiation. The intermediate frequency bandwidth is higher for the line-of-sight ECE system as a result of the larger tangentiality of the beam to the rational surfaces compared to equatorial

ECE. At angles near the optimal angle the detection of the location failed for islands larger than 4 cm for the 2/1 NTM. This results from the reduced anti-correlation of neighbouring ECE channels due to temperature equilibration in the island. For the detected islands, the detection latency remains below 500 ms and 1 s for the 2/1 and 3/2 NTM respectively.

The simulations indicate that, using equatorial ECE, detection of magnetic islands within 500 ms is possible. However, a trade-off exists between detection latency and detection accuracy. Using a small channel spacing, the detected position is more accurate, but the increased noise level, due to the smaller intermediate frequency bandwidth, requires a longer detection time. Although the line-of-sight ECE system achieves similar detection times if the island location is detected, detection fails for larger island widths. Therefore using the implemented detection algorithm the line-of-sight ECE system only works for small island widths. For both equatorial ECE and line-of-sight ECE implementation of a multi-scale detection technique might prove beneficial.

Acknowledgments

The work in this paper has been performed in the framework of the NWO-RFBR Centre of Excellence on Fusion Physics and Technology (grant 047.018.002). This work, supported by the European Communities under the contract of association between EURATOM-FOM, was carried out within the framework of the European Fusion Program. The views and opinions expressed herein do not necessarily reflect those of the European Commission.

6.A. Additional detection algorithms

In this chapter, the algorithm by Berrino *et al* is used. In writing the paper, the algorithms by Hennen *et al* and Isayama *et al* were also evaluated. This section aims to provide insight in the comparison of algorithms and the resulting choice for the algorithm by Berrino *at al*. The comparison is done with a channel spacing equal to the intermediate frequency bandwidth B_{IF} of 400 MHz for equatorial ECE.

There are multiple requirements for a good position detection algorithm. As the position detection is the only sensor considered, it should not only provide an accurate location, but it also should not give a location if no island is present. This might result in reduced detection capabilities to ensure noise is never interpreted as a magnetic island. Inclusion of a separate detector for island presence could therefore result in increased performance of the location sensor. Additionally the algorithms should provide a detected location with a noise smaller than the required accuracy and detection of both 2/1 and 3/2 modes with the same sensor should be possible.

The algorithm by Isayama *et al* detects the island at the channel with the minimum standard deviation.[70] For a magnetic island positioned in between two channels, the minimum in standard deviation will alternate between both channels, giving an accuracy in position of 400 MHz, which is twice as large as allowed. A channel spacing of 200 MHz could be used to arrive at an accurate detection of the position, but this in turn would increase channel noise, resulting in a longer detection time given that detection is possible. The performance of the algorithm could be improved by performing an interpolation of the minimum fluctuation by, for instance, a parabolic fit on the channel with the minimum fluctuation and the neighbouring channels.

Like the Berrino algorithm, the detection algorithm by Hennen *et al* relies on the anti-correlation at opposite sides of the island.[9] The difference with the algorithm by Berrino *et al* results from the extent in which different channels are taken into account. The algorithm by Berrino *et al* only considers the correlation between adjacent channels, while correlations of all the channels are used by the algorithm by Hennen *et al*. Although the algorithm by Hennen *et al* performed well on the TEXTOR tokamak, the weighting of all temperature oscillations does not give the best results for the asymmetric temperature profile. As a result of the influence of all channels, noise has a larger effect and can result in a fast variation of the island location, especially for small islands which cause a small temperature oscillation by themselves. An adaption of the algorithm by Hennen *et al* based on the asymmetric temperature profile proved beneficial for 2/1 mode detection, but failed for the 3/2 mode due to larger noise at ECE frequencies lower than the island ECE frequency, which resulted in an offset.

Figure 6.8 shows the detected island location for a seed island width of 2 cm, growing in accordance with the polarization model with $w_{marg} = 2$ cm. The island location is detected with

the algorithms by Hennen *et al* and Isayama *et al* and compared with the algorithm by Berrino *et al*, shown in figure 6.3. The figure clearly shows performance with the algorithm by Isayama *et al* is limited by the spacing. The algorithm by Hennen *et al* has as smaller standard deviation, but suffers from an offset towards higher ECE frequency, resulting from the asymmetric temperature profile.

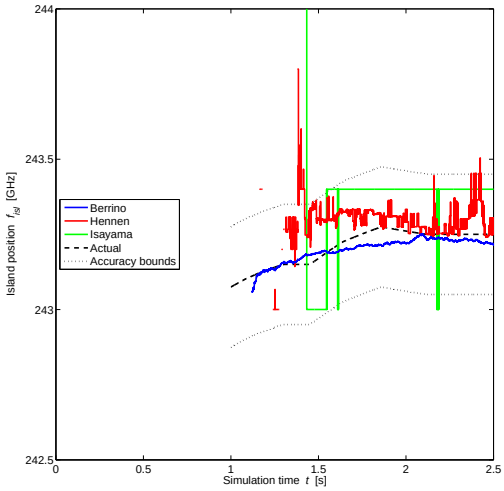

Figure 6.8.: *Island location in ECE frequency for three detection algorithms. The settings for island growth, island rotation and spacing are the same as in figure 6.3. The algorithms by Berrino et al, Hennen et al and Isayama et al are shown in blue, red and green respectively. The actual island position and required accuracy bounds are shown in black dashed and dotted lines respectively.*

7. Conclusions

NTM control on ITER is required to prevent disruptions and maintain a high core temperature for high fusion yield. The 2/1 and 3/2 NTMs have the highest impact on core temperature. Suppression of NTMs using ECCD is foreseen on ITER. In this work, the role ECE could play in an NTM control loop on ITER is investigated. Three control loops using ECE for NTM are shown as possible implementations for ITER. Based on a combined model for island growth and rotation, control requirements for full suppression of NTMs are derived. Using simulations, it is tested whether an ECE diagnostic could fulfill these requirements.

The reliance of most NTM diagnostics on magnetic island rotation, the decreased effect of ECCD on island suppression for islands with an unfavourable phase and the increased chance of a disruption motivate full NTM suppression before mode-locking occurs, i.e. stop of island rotation, as a control objective. A combined model of island growth and island rotation is used to derive the required accuracy in the deposition position and the maximum allowed latency between the seeding of the island and the start of ECCD deposition, which still results in full suppression before mode locking. The most stringent model requires accuracies of the deposition position of 7 mm and 5 mm for the 2/1 and 3/2 NTM respectively. This is mainly determined by the positioning accuracy required at small island widths to achieve full suppression. The maximum allowed latency is independent of whether ECCD is deposited continuously or in phase with the island rotation. Only the detection of the island position is a bare essential for NTM control on ITER. Note that control strategies that do not rely on full NTM suppression exist as well, but requirements are not derived for them.

The NOn-Thermal ECE Code (NOTEC) is used for simulating ECE spectra with magnetic islands for a standard burning H-mode ITER plasma. A helical flux perturbation is imposed which contains the asymmetry in island width and temperature at positions $r < r_s$ and $r < r_s$, resulting in a temperature profile consistent with experimental observations. The temperature inside the island is constant due to increased transport, while the transport outside the island is unaffected. The temperature outside the island changes due to a shift of the incompressible flux surfaces and the temperature drop over the island. A database of ECE spectra for different island widths and phases is combined with the model for island growth and rotation to derive ECE signals as a function of time. An algorithm by Berrino *et al* is used to detect the island location

in terms of the ECE frequency corresponding to the minimum temperature fluctuation. The selection of an appropriate ECE channel layout depends on the accuracy that should be achieved and the noise level. The intermediate frequency bandwidth B_{IF} should be large to decrease thermal noise, while the spatial detection accuracy requires a small channel spacing which limits the intermediate frequency bandwidth. With equatorial ECE, detection within 500 ms is possible for 2/1 and 3/2 NTMs with varying seed island widths. Detection of ECE via the line-of-sight of ECCD is possible for both the 2/1 and 3/2 NTM. Larger islands are not detectable for all angles α, but for the detected island widths, the detection latency remains below 500 ms and 1 s for the 2/1 and 3/2 NTM.

In this work, requirements for NTM control on ITER are derived and used as a guideline for ECE detection requirements. Both accurate and timely detection of magnetic islands is possible using the algorithm by Berrino *et al*. For a line-of-sight system the capabilities are limited. An expansion of the algorithm by Berrino *et al* that incorporates multiple scales could improve detection capabilities. With the capabilities of an island position detector addressed, further steps can be made to incorporate a controller and the launcher dynamics for a simulation of the full ITER NTM control loop.

8. Recommendations for further research

This work showed that ECE could serve as a sensor for position detection in an NTM control loop, which is but one step in the design of an NTM control loop for ITER. Additional knowledge of NTM physics is required, as well as proof-of-principle experiments of control, while simultaneously keeping in mind the big picture of fusion power generation. These three issues are addressed below.

The behaviour of magnetic islands at large island width is reasonable well known from experiments, but the difficulty to detect smaller islands results in a lack of knowledge of island growth in this range. An experimental effort to fill this knowledge is required, preferably using measurements on several tokamaks. The availability of more extensive models for NTM physics also offers a way to gain more insight in experiments and helps to achieve a consistent model for NTM physics on current machines that allows for more accurate extrapolations to ITER conditions.

For NTM control in particular, proof-of-principle control of NTMs should be demonstrated in ITER relevant scenarios. In turn this control might allow investigation of new parameter ranges, such as NTM physics at small island widths. Control experiments that can be extrapolated to ITER conditions serve as the key goal to ensure that NTMs pose no problem for ITER plasmas.

Control of NTMs is however but one step in the creation of a stable ITER operating regime. Experiments and simulations that give insight in consistent operating regimes dealing not only with NTMs, but with all expected issues are a goal worth pursuing. Forcing future power producing fusion devices to have only one operating regime with crystal clear and undisputable requirements, that allows for dedicated experiments to fill the gaps in the knowledge base, could prove useful in focussing and uniting fusion research.

Acknowledgements

I would like to thank everyone who contributed to this to work. Unfortunately the many interesting discussions that serve both as inspiration and a starting point are never part of the scientific results as presented in, for instance, this report. Thanks everybody at FOM Rijnhuizen and the Fusion group in Eindhoven for both new insights and a lot of fun. Verder wil ik een paar mensen nog graag in het bijzonder bedanken.

Allereest dank aan mijn beide begeleiders Egbert en Niek. Niek, we hebben weinig bij elkaar gezeten, maar altijd toonde je een sterke betrokkenheid en hield je niet alleen bezig met de inhoud maar ook met de zichtbaarheid van mijn werk. Egbert, het was erg prettig met je samen te werken. Het was erg fijn bij je binnen te kunnen lopen om even ergens over te discussiëren of wat resultaten te laten zien. Daarnaast had ik aan Marco de Baar ook nog een extra begeleider. Marco, bedankt voor jouw betrokkenheid bij het tot stand komen van de papers. Daarnaast wil ik jullie, Niek, Egbert en Marco, in het bijzonder bedanken voor de kansen die jullie mij hebben gegeven om mijn eerste papers te schrijven en werk op internationaal niveau te presenteren.

The help of Max Austin, Bircan Ayten, Waldo Bongers, Ivo Classen, Mark Henderson, Diego de Lazzari, Hans Oosterbeek, Dennis Ronden and Chris Schüller is greatly appreciated. Jan-Willem en Rob, bedankt voor de hulp met Fortan 90 en tools als Subversion en Doxygen. Ook heb ik veel gehad aan mijn mede-kelderbewoners, met in het bijzonder Joost Daniëls en Miel Stapel als klankbord.

Ook wil ik graag de mensen van de control groep uit Eindhoven nog even noemen. Jullie werk vormt een welkome toevoeging op de fusiefysica om samen de strijd aan te gaan voor een stabiele tokamak. Pieter, Bart, Gert, Menno, Matthijs en Gillis, bedankt voor interessante presentaties, goede discussies en nieuwe inzichten.

A. Derivation of ECE intensity

This appendix provides background information on the derivation of the measured ECE intensity. The effect of the spatial dependence of magnetic fields, broadening of the emission region and the refractive index of the plasma are addressed as well. This appendix is based on a discussion in a book on diagnostics by Hutchinson.[19]

In the first section, an expression for the radiation coming for a single accelerated charge is presented. Based on this expression, the radiation coming from a single electron gyrating around the magnetic field lines is derived in section A.2. The notion of emissivity is used when the single electron emission is generalized to a distribution of electrons in section A.3. In this section, the broadening of emission is also introduced as a result of averaging over a distribution of electrons. The relation between the ECE intensity, absorption of ECE and the temperature is elucidated in section A.4. Section A.5 focusses on the relation between the magnetic field and the electron cyclotron frequency, which results in a localized measurement of the electron temperature in a tokamak. In the final section the effect of the refractive index of the plasma is addressed.

A.1. Radiation from an accelerated charge

An electromagnetic wave can be described by a scalar potential ϕ and a vector potential $\vec{A}$, which satisfy the equations:[19]

$$\begin{aligned}
&\nabla \cdot \vec{A} + \frac{1}{c^2}\frac{\partial \phi}{\partial t} = 0 \\
&\vec{B} = \nabla \times \vec{A} \\
&\vec{E} = -\frac{\partial \vec{A}}{\partial t} - \nabla\phi \\
&\left(\nabla^2 - \frac{1}{c^2}\frac{\partial^2}{\partial t^2}\right)\phi = -\frac{\rho}{\epsilon_0} \\
&\left(\nabla^2 - \frac{1}{c^2}\frac{\partial^2}{\partial t^2}\right)\vec{A} = -\mu_0 \vec{j}
\end{aligned} \quad . \tag{A.1}$$

In equation A.1, c is the speed of light in vacuum, ρ is the charge density, j the current density, ϵ_0 the permittivity of free space and μ_0 the permeability of free space. A single point charge q at

position $\vec{r}(t)$ moving with velocity $\vec{v}$, gives rise to a charge density $\rho = q\delta(\vec{x} - \vec{r}(t))$ and current density $j = q\vec{v}\delta(\vec{x} - \vec{r}(t))$, where $\vec{x}$ an arbitrary position where the fields are evaluated. The Liénard-Wiechert potentials for this point charge are described by equation A.2.[75]

$$\begin{aligned} \phi &= \frac{q}{4\pi\epsilon_0} \frac{1}{\left(1 - \frac{\vec{R}\cdot\vec{v}(\vec{t}_r)}{Rc}\right)\left(\vec{x} - \vec{r}(t_r)\right)} \\ \vec{A} &= \frac{\mu_0 q}{4\pi} \frac{\vec{v}(t_r)}{\left(1 - \frac{\vec{R}\cdot\vec{v}(\vec{t}_r)}{Rc}\right)\left(\vec{x} - \vec{r}(t_r)\right)} \end{aligned} \tag{A.2}$$

In equation A.2, the retarded time is given by $t_r = t - \frac{|\vec{x} - \vec{r}(t)|}{c}$ and $\vec{R} = R\hat{R}$ is the vector from the emission point $\vec{r}(t)$ to the field point $\vec{x}$, where R is the length of the vector. The potentials can be combined with equation A.1 to form an expression for the electric field $\vec{E}$. The magnetic field $\vec{B}$ is related to the electric field $\vec{E}$ by $\vec{B} = \frac{(\vec{x} - \vec{r}(t_r)) \times \vec{E}}{c}$. The radiated energy per unit surface and unit time at the field point is given by the Poynting vector $\vec{S} = \frac{\vec{E} \times \vec{B}}{\mu_0} = \frac{|E|^2 (\vec{x} - \vec{r}(t_r))}{\mu_0 c}$. By performing a Fourier integral of the far field ($R \gg r$) component of the electric field $\vec{E}$, the power P radiated by a single moving particle at the field point $\vec{x}$ is given by equation A.3.[19]

$$\frac{d^2P}{d\Omega_s df} = \frac{q^2 f^2}{2\epsilon_0 c} \left| \int_{-\infty}^{\infty} \hat{R} \times \left(\hat{R} \times \frac{\vec{v}}{c}\right) \exp i2\pi f \left(t' - \frac{\hat{R} \cdot \vec{r}}{c}\right) \mathrm{d}t' \right|^2 \tag{A.3}$$

In equation A.3, the radiated power is expressed per unit solid angle Ω_s and per unit frequency f.

A.2. Radiation from a single gyrating electron

The motion of an electron moving in a magnetic field can be described by equation A.4.

$$\frac{d}{dt}\left(m_{r,e}\vec{v}\right) = -e\left(\vec{v} \times \vec{B}\right) \tag{A.4}$$

In equation A.4, $m_{r,e} = \gamma m_e \equiv \frac{m_e}{\sqrt{1 - \frac{|\vec{v}|^2}{c^2}}}$ is the relativistic electron mass, e the elementary charge and c the speed of light in vacuum. The magnetic field $\vec{B}$ is constant and chosen along the z axis, such that $\vec{B} = B_0\hat{z}$. The velocity and position of the electron are now given by equation A.5.

$$\begin{aligned} \vec{v} &= v_\perp \left(\hat{x}\cos\Omega_r t + \hat{y}\sin\Omega_r t\right) + v_\parallel \hat{z} \\ \vec{r} &= \frac{v_\perp}{\Omega_r} \left(\hat{x}\sin\Omega_r t - \hat{y}\cos\Omega_r t\right) + v_\parallel t\hat{z} \end{aligned} \tag{A.5}$$

In equation A.5, the velocity $v_\perp$ perpendicular to the magnetic field described a rotating motion. The frequency of this rotation is the relativistically shifted electron cyclotron frequency:

$$\Omega_r \equiv \frac{\Omega}{\gamma} = \frac{eB_0}{m_e\gamma}. \tag{A.6}$$

The irradiated power observed, looking at the particle from an angle θ between the view direction $\hat{R} = \sin\theta\hat{x} + \cos\theta\hat{z}$ and the z axis, is found by combining equation A.3 and A.5. Equation A.7 gives the resulting radiated power per frequency f and solid angle Ω_s.[19]

$$\frac{d^2P}{d\Omega_s df} = \frac{\pi e^2 f^2}{\epsilon_0 c}\sum_{m=1}^{\infty}\left\{\left[\left(\frac{\cos\theta + \frac{v_\parallel}{c}}{\sin\theta}\right)^2 J_m^2(\zeta) + \frac{v_\perp^2}{c^2}J_m'^2(\zeta)\right]\frac{\delta\left(\left\{1 - \frac{v_\parallel}{c}\cos\theta\right\}2\pi f - m\Omega_r\right)}{1 - \frac{v_\parallel}{c}\cos\theta}\right\}$$
$$\text{with } \zeta = \frac{2\pi f}{\Omega_r}\frac{v_\perp}{c}\sin\theta \text{ and } \exp\{-i\zeta\sin\Omega_r t\} = \sum_{-\infty}^{\infty}\exp\{-im\Omega_r t\}J_m(\zeta) \tag{A.7}$$

In equation A.7, the Bessel functions $J_m(\zeta)$ and dirac delta function $\delta(x)$ are used. The equation shows that a single gyrating electron emits radiation, at fixed frequencies, near the relativistic cyclotron frequency Ω_r and at higher harmonics given by $m > 1$. A Doppler shift results from the movement of the particle in the direction parallel to the magnetic field projected on the viewing direction. The frequency $f_m = \frac{m\Omega}{2\pi}\frac{\sqrt{1-\frac{v^2}{c^2}}}{1-\frac{v_\parallel}{c}\cos\theta}$ expresses the effect of the relativistic mass, in the numerator, and the Doppler shift, in the denominator.

A.3. Emissivity and broadening

The ECE radiation originates from an ensemble of particles having different velocities. The number of particles having a velocity $v_\perp$ and $v_\parallel$ is given by $g(v_\perp, v_\parallel)2\pi v_\perp dv_\perp dv_\parallel$, where $g(v_\perp, v_\parallel)$ is the electron velocity distribution function. The power emitted per unit volume per unit frequency and per unit solid angle is called the emissivity j. It is different from the power that is observed by a factor $1 - \frac{v_\parallel}{c}\cos\theta$.[19] Equation A.8 gives an expression for the emissivity in a tenuous plasma, based on equation A.7.

$$j(f,\theta) = \int \frac{d^2P}{d\Omega_s df}\left(1 - \frac{v_\parallel}{c}\cos\theta\right)g(v_\perp, v_\parallel)2\pi v_\perp dv_\perp dv_\parallel \tag{A.8}$$

As a result of the integration over the velocity distribution, the emitted radiation is broadened due to the relativistic mass and the Doppler shift of the radiation emitted by a single particle. The relative importance of the broadening effects can be evaluated by looking at the radiation frequency f_m of a single particle. Natural broadening, due to finite lifetime of a quantum state, and collision broadening, due to disturbance of the wave train by collisions, are usually negligible.[19] The Doppler shift will be larger than the relativistic shift if $\frac{v_\parallel}{c}\cos\theta > \frac{v^2}{c^2}$. Therefore

relativistic broadening is the main broadening effect for radiation perpendicular to the magnetic field.

If the emission is predominantly around $f_m = \frac{m\Omega}{2\pi}$ and sufficiently narrow to prevent overlap, the emissivity can be approximated by the emissivity of the peak j_m combined with a shape function $\phi(f - f_m)$ that gives the shape of the broadening, resulting in the following expression for the emissivity: $j(f) = j_m\phi(f - f_m)$.

A.4. Absorption, radiation intensity and temperature

The intensity $I(f)$ of ECE with frequency f is a combination of emission and absorption. This balance is expressed in equation A.9, in which s is the distance along a ray and $\alpha(f)$ is the absorption coefficient.

$$\frac{d}{ds}I(f) = j(f) - I(f)\alpha(f) \tag{A.9}$$

Equation A.10 defines the optical depth. This notion can be used in an integration of equation A.9, which yields equation A.11, assuming constant $j(f)$ and $\alpha(f)$ between s_1 and s_2.

$$\tau \equiv \int^{s} \alpha(f)ds \tag{A.10}$$

$$\begin{aligned} I(f, s_2) &= I(f, s_1)\exp\{-(\tau_2 - \tau_1)\} + \int_{s_1}^{s_2} j(f)\exp\{\tau - \tau_2\}\,ds \\ &= I(f, s_1)\exp\{-(\tau_2 - \tau_1)\} + \int_{\tau_1}^{\tau_2} \frac{j(f)}{\alpha(f)}\exp\{\tau - \tau_2\}\,d\tau \\ &= I(f, s_1)\exp\{-(\tau_2 - \tau_1)\} + \frac{j(f)}{\alpha(f)}\left[1 - \exp\{-(\tau_2 - \tau_1)\}\right] \end{aligned} \tag{A.11}$$

Equation A.11 describes the radiated intensity $I(f, s_2)$ as a result of incoming radiation $I(s_1)$, which is partially absorbed, and emitted radiation, resulting from the integration. If $\tau_2 \gg \tau_1 \gg 1$, the plasma is optically thick between s_1 and s_2 and the intensity at s_2 is $I(s_2) = \frac{j(f)}{\alpha(f)}$.

If there is local thermal equilibrium, the local absorption coefficient and local emissivity are related to the blackbody intensity via Kirchof's law, given in equation A.12.

$$\frac{j(f)}{\alpha(f)} = B(f) = \frac{f^2}{c^2}\frac{hf}{e^{\frac{hf}{k_BT}} - 1} \overset{hf \ll k_BT}{=} \frac{f^2 k_B T}{c^2} \tag{A.12}$$

In equation A.12, the first expression for $B(f)$ is Plank's radiation formula, which simplifies to the classical Rayleigh-Jeans approximation when $hf \ll k_BT$, which holds for most tokamak plasmas. Consequences of Kirchof's law are the similarity in shape of the equations for $j(f)$

and $\alpha(f)$ which differ only in a factor $\frac{f^2 k_B T}{c^2}$ and the direct proportionality between the electron temperature and the intensity from an optically thick plasma layer.

A.5. Scaling with magnetic field

The electron cyclotron frequency varies with the magnetic field. In a tokamak, the magnetic field is, to a first approximation, inversely proportional to the major radius, resulting in an equal proportionality for the electron cyclotron frequency. Neglecting broadening, the emissivity $j(f_0)$ at a frequency $f_0 = \frac{eB_0R_0}{2\pi m_e(R_0+s_0)}$ is peaked and therefore the intensity $I(f_0)$ solely represents information about s_0. In practice, the broadened emissivity necessitates an evaluation of the optical thickness to determine the origin of the radiation at frequency f_0.

The intensity of radiation at a frequency f_0 is found by integrating equation A.9, assuming no incident light and a slow varying magnetic field compared to the radiation wavelength, resulting in equation A.13.

$$\begin{aligned} I(f) &= \int_{s_1}^{s_2} j(f,s)\exp\{\tau-\tau_2\}\,ds \\ &= \int_{\tau_1}^{\tau_2} \frac{j(f,s(\tau))}{\alpha(f,s(\tau))}\exp\{\tau-\tau_2\}\,d\tau \\ &= \frac{f_0^2 k_B T(s_0)}{c^2}\left(1-\mathrm{e}^{-\tau_0}\right) \\ &\text{with } \tau_0 = \int_{s_1}^{s_2}\alpha(f_0,s)ds = \int_{s_1}^{s_2}\alpha(f_0,s_0)\phi(s-s_0)ds \end{aligned} \tag{A.13}$$

In equation A.13, local temperature equilibrium is assumed between s_1 and s_2 and $\phi(s - s_0)$ is a shape function, describing the relative absorption of around the point s_0 of maximum absorption. A narrow region that has a local temperature equilibrium and a high optical depth ($\tau_0 \gg 1$) provides a localized measurement of the temperature. The width of this region can be smaller than the width of the region that emits radiation at the detected frequency, because of the absorption of light. However, if the optical depth is small, the detected radiation contains not only ECE from the plasma, but also reflections on walls. This could make measurements of optically thin harmonic frequencies unreliable and therefore measurement of optical thick harmonic frequencies is preferred.

A.6. Refractive index of the plasma

All previous sections assumed a tenuous plasma and neglected the refractive index of the plasma. Propagation of ECE is affected by the refractive characteristics of the plasma, which depend on

wave polarization, angle between the wave direction and the magnetic field, plasma density and magnetic field magnitude.

The refractive index of a cold plasma is expressed by the Appleton-Hartree equation (equation A.14), for which $X = \frac{\omega_p^2}{(2\pi f)^2}$, $Y = \frac{\Omega}{2\pi f}$ and the refractive index $N = \frac{kc}{\omega}$.[19 76] k is the wave vector, θ the angle between the wave vector and the magnetic field (similar to the definition in section A.2), Ω the electron cyclotron frequency (described in equation A.6) and the plasma frequency is given by $\omega_p = \sqrt{\frac{n_e e^2}{\epsilon_0 m_e}}$, where n_e is the electron density.

$$N^2 = 1 - \frac{X(1-X)}{1 - X - \frac{1}{2}Y^2 \sin^2\theta \pm \sqrt{\left(\frac{1}{2}Y^2 \sin^2\theta\right)^2 + (1-X)^2 Y^2 \cos^2\theta}} \tag{A.14}$$

For both parallel ($\theta = 0°$) and perpendicular ($\theta = 90°$) propagation, there are two solutions to the Appleton-Hartree equation with different polarizations. These are left and right circulating polarized light for parallel propagation and the ordinary and extraordinary mode for perpendicular propagation. In the ordinary mode the polarization is parallel to the magnetic field, while in extraordinary mode the polarization is perpendicular to it. In a tokamak, the magnetic field lines are closed. This requires that ECE propagates perpendicular to the magnetic field. If the angle θ is varied from 0° to 90°, the left polarization changes into the ordinary mode and the right polarization changes into the extraordinary mode.

Resonances ($N = \infty$) and cut-offs ($N = 0$) in the Appleton-Hartree equation limit what frequencies of ECE arrive at the plasma boundary.[77] Cut-offs result in reflection of the wave and dissipation of wave energy occurs at resonances, thus both mechanisms limit the radiation that is detectable. The ordinary mode (O-mode) only has a cut-off at the plasma frequency ω_p. The extraordinary mode (X-mode) is limited by reflection at the lower and upper cut-off and resonance at the upper hybrid frequency. Radiation at frequencies between the lower cut-off and the upper hybrid and above the upper cut-off can propagate in the plasma. Equation A.15 gives expressions for the lower cut-off frequency ω_{lc}, upper cut-off frequencies ω_{uc} and the upper hybrid frequency ω_{uh}.[77] The evaluation of the the cut-offs and resonances gives a first approximation to what harmonics could be used for ECE. Overlap of harmonic modes and the spatial accuracy pose other constraints on the measurable regions.

$$\begin{aligned} \omega_{lc} &= \frac{1}{2}\left(-\Omega + \sqrt{\Omega^2 + \omega_p^2}\right) \\ \omega_{uc} &= \omega_{lc} + \Omega = \frac{1}{2}\left(\Omega + \sqrt{\Omega^2 + \omega_p^2}\right) \\ \omega_{uh} &= \sqrt{\Omega^2 + \omega_p^2} \end{aligned} \tag{A.15}$$

Whether a particular polarization mode and harmonic frequency is useful for measurements also depends on the emissivity and absorption of a mode, which differs between polarizations.

This is expressed by writing the emissivity $j_m^{\pm} = j_m \eta_m^{\pm}$ and absorption coefficient $\alpha_m^{\pm} = \alpha_m \eta_m^{\pm}$ as a polarization independent quantity (resp. j_m and α_m) and a polarization dependent correction $\eta_m^{\pm}$, where, for $\theta = 90°$, + refers to O-mode and − to X-mode and $\eta^+ + \eta^- = 1$. Expressions for the coefficient $\eta_m^{\pm}$ differ significantly between $m = 1$ and $m > 1$ and between perpendicular ($\theta = 90°$) and oblique ($0 < \theta < 90°$) propagation. The review article by Bornatici *et al* summarizes the theory on emissivity and provides analytical expressions for absorption coefficients including, among other, polarization and finite density effects.[40]

B. NTM control in current tokamaks

The expected occurrence of NTMs on ITER is an important motivation for the study of NTM physics and control in current tokamaks. NTM physics and control are studied for ITER on ASDEX Upgrade, DIII-D, FT-U, HL-2A, JET, JT-60U/SA, NSTX, TEXTOR and TCV within the MHD, Disruptions and Magnetic Control joint experiments on Current Drive Prevention/Stabilization of NTMs (MDC-8), part of the International Tokamak Physics Activity (ITPA).[78] NTM control on ASDEX Upgrade, DIII-D, JT-60 and TEXTOR is discussed in the this appendix. These experiments all use ECCD/ECRH for NTM suppression and give an overview of control strategies under consideration.

B.1. ASDEX Upgrade

ASDEX Upgrade (AUG) is a German tokamak with a major plasma radius of 1.65 m, a minor radius of 0.5 m and an elongation of 1.8, resulting in a plasma volume of 14 m^3. NTMs have been a known phenomenon in AUG for more than a decade.[79] AUG ranks as the largest European tokamak that has Electron Cyclotron Current Drive (ECCD) and Resonant Heating (ECRH) capability. This makes it the main European set-up for NTM suppression experiments. Figure B.1 shows the effect of a NTM on an AUG plasma.

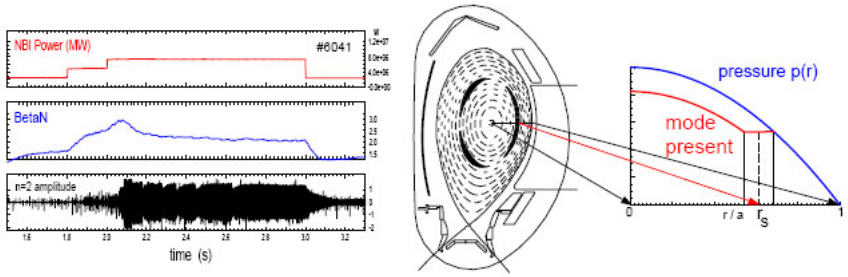

Figure B.1.: *The effect of a $q = 3/2$ NTM on an AUG plasma. On the left an AUG shot is shown in which a NTM is triggered by increasing β_N through Neutral Beam Injection (NBI). A schematic picture showing the effect of the NTM on the flux surfaces and the pressure profile is shown on the left. Picture from Urso*[42]

A combination of diagnostics has been tested for magnetic island detection.[33] A 60 channel Electron Cyclotron Emission (ECE) system has been used, capable of measuring temperature fluctuations in a horizontal (near-equatorial) plane with an spatial resolution of 1-2 cm.[80] Magnetic islands result in an anti-phase of ECE perturbation on different sides of the magnetic island. A second detection method relies on a measurement of two Mirnov coils 180° apart in toroidal angle, measuring the magnetic perturbation resulting from the island. The radial position is determined using reconstruction of the q-profile based on Motional Stark Effect (MSE) measurements.[19]

ECCD and ECRH both contribute in stabilizing the NTM.[49] The flux surface on which ECCD/ECRH is deposited is varied either by changing the toroidal magnetic field, which shifts the position of the Electron Cyclotron resonance radially, or by using launcher mirrors, changing the vertical deposition position.[30] Ray tracing calculations, with TORBEAM, or low power modulated ECCD/ECRH deposition, detected by ECE, allow a determination of the deposition position.[33] Modulation of ECCD/ECRH showed substantially higher suppression efficiency for small island sizes, where the modulation frequency is provided by a digital phase-locked loop connected to an ECE channel close to the magnetic island.[44]

Next steps on AUG are showing the viability of real-time control loops. Based on the current ECE and ECCD/ECRH configuration, a system can rely on measurements or on reconstruction of flux surfaces and deposition position. The ECCD/ECRH deposition position can either be measured using ECE or calculated using ray tracing, which relies on a measured density profile. The island position can be measured directly using ECE or calculated from a q-profile inferred from MSE measurements. The phase always needs to be measured using either ECE or Mirnov coils. Preliminary investigations show all tasks can be performed within the 100 ms growth time of NTMs in AUG.[30] However, calculation of the deposition position could take up to 70 ms and using ECCD/ECRH deposition position measurement could provide an unwanted disturbance of the plasma.

A control design using ECRH/ECCD deposition and ECE measurement along the same sightline is a possible alternative, which is investigated for use on AUG, following its successful results on TEXTOR (see sect. B.4).[34]

B.2. DIII-D

DIII-D is a tokamak in the United States, which has a major radius of 1.66 m, a minor radius of 0.67 m and an elongation κ of up to 2.[81] This makes it the largest operating tokamak with an ECCD/ECRH installation. Magnetic islands in DIII-D have been observed and studied for more than two decades.[82] Control strategy identification is an important part of NTM experiments.

Two diagnostics are used for magnetic island detection. The signal amplitude of a combination of Mirnov coils serves as an uncalibrated island width measurement.[65] The frequency of the rotation of the magnetic island is also determined by Mirnov coils. Oblique ECE is a second measurement technique.[8] It relies on a 2-channel radiometer, which has a similar sightline as the ECCD/ECRH launcher, the only difference being a 2° toroidal angle ϕ offset. Assuming that the mirror for the oblique ECE and ECCD/ECRH move in exactly the same way, positioning of the two ECE channels symmetrically around the magnetic island results in a deposition of ECCD/ECRH at the island. Oblique ECE does not require a separation of a low power signal from a higher power signal, as is the case for the TEXTOR set-up (see sect. B.4). It is however cumbersome to compensate for fluctuations on either the ECE or ECCD/ECRH mirror, thus making it impossible to guarantee enough coherence between the measurement and deposition position.

The ECCD/ECRH deposition position is changed by variation of the plasma position or toroidal magnetic field. The deposition position is not directly measured, but inferred from the effect it has on the island width. Implementation of a ray tracing routine is considered as an alternative.[65]

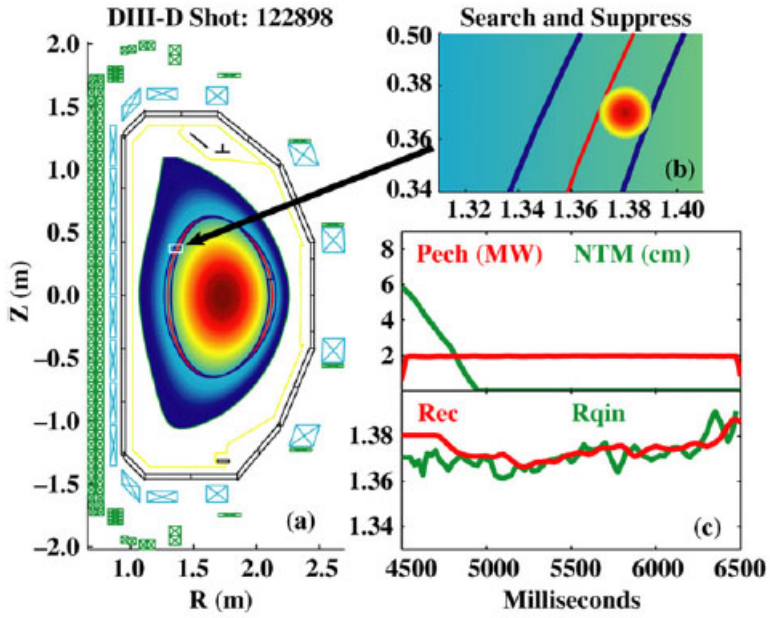

Figure B.2.: *The search and suppress algorithm used in a DIII-D shot. The effect of the NTM on the flux surface is shown on the left. EC injection is varied to achieve a good radial alignment to the island position (bottom-right). The resulting alignment of the position is shown, in a close-up, in the top-right graph. The middle-right graph shows the suppression of the island by EC power. Picture from Humphreys et. al.*[83]

Three control strategies are used in DIII-D.[65] Search and suppress (depicted in figure B.2) varies the plasma position in a stepwise manner. The response of the Mirnov coil is measured to determine when the alignment leads to island suppression. The dwell time between two steps is an important parameter for the success of this strategy. The target lock strategy performs a sweep over the plasma and relates the measured growth rate to the growth rate calculated from the GRE. The maximum likelihood location for optimal deposition is determined based on this measurement. Active tracking, the third strategy, is used in absence of a magnetic island. The q-profile is calculated from MSE measurements and the deposition is changed in such a way that alignment with a specific q-value is maintained. This requires initial alignment on that specific q-value and refraction of the ECCD/ECRH beam should have a minor influence if the deposition position is changed. Ray tracing is required if this cannot be assured.

B.3. JT-60

JT-60 is a Japanese tokamak with a major radius of 3.4 m, a minor radius of 0.9 m and an elongation of 2, resulting in a plasma volume of nearly 100 m^3.[84] It is currently the largest in Asia and is being upgraded from its current version (JT-60U) to a new version (JT-60SC), which is suitable for high normalized beta operation. JT-60U was in operation until 2008. An important research goal on JT-60 is the study of stable high β plasma discharges, which also requires experiments on the effect of NTMs on such discharges.

The stabilizing effect of EC waves at the first harmonic O-mode and the second harmonic X-mode on the q=2/1 and q=3/2 NTMs is examined.[6] Experiments were conducted in which EC power was modulated with the same frequency as the island rotation frequency, showing that island width decreases with a time constant three times faster than for unmodulated EC power. The effect of phase differences between power modulation and the island frequency was examined. Phase difference of 50° result in a doubling of the time constant for the island width decay. Larger phase differences have either no effect (90°) or even increase island growth (180°). The rotation frequency is determined from the magnetic perturbations, measured with Mirnov coils.

The mode position is determined from the channel with the minimum perturbation of the ECE radiometer in the equatorial plane.[70] Theoretically, the perturbation is zero at the O-point of the magnetic island. Variation of the poloidal angle of the EC launcher ensures the misalignment of the EC deposition with the island O-point is kept small. This method requires a mapping from the ECE radiometer measurement positions to the EC launcher angles, required to deposit on a specific surface. This mapping is probably obtained using a look-up table, calculated using a

ray-tracing and Fokker-Planck code. Figure B.3 shows the real-time control of the EC mirror angle to track the NTM position.

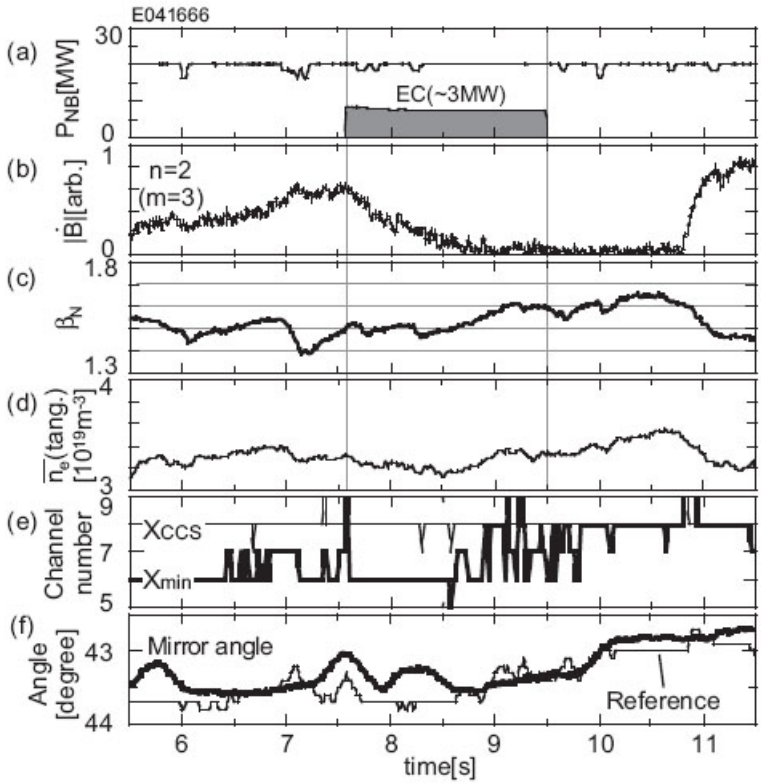

Figure B.3.: *Real-time mirror angle control in JT-60U. The deposited power (NBI and EC) is shown in box (a). The island width is related to the magnetic perturbation signal, shown in box (b). β_N and the average electron density are shown in box (c) and box (d) respectively. In box (e), the ECE channel with the minimum perturbation (X_{MIN}) and the ECE channel which would contain the mode based on a boundary reconstruction (X_{CCS}) are shown. Box (f) shows the mirror angle and the reference. Box (b) shows a NTM onset and the stabilization of the island. Box (f) shows that the angle reference is followed within half a degree accuracy. Picture from Isayama et. al.*[70]

B.4. TEXTOR

TEXTOR is a German tokamak with a circular cross section, a major radius of 1.75 m and a minor radius of 0.46 m.[85] A main research field of TEXTOR is plasma surface interaction. For this purpose a magnetic coil geometry, the Dynamic Ergodic Divertor (DED), is used to tune the interaction of the plasma with the wall.[86] The magnetic field created by the DED coils can

also reinforce tearing modes. Therefore, although TEXTOR is stable to tearing modes, the DED coils make it a good set-up for the controlled creation and investigation of tearing modes.[87]

The main diagnostics on TEXTOR for the detection of magnetic islands are Mirnov coils and ECE. A radiometer, with 11 channels covering a range of 60 cm in the equatorial plane, is assisted by a 2D ECE Imaging measurement, which measures 16 horizontal view lines with 8 channels each.[14] ECRH is the main actuator for tearing mode stabilization.

A combination of ECE radiometry and ECRH along the same line-of-sight is a unique experiment conducted on TEXTOR.[88] A 6-channel radiometer detects the nW-level ECE emission in a kW ECRH power background signal, symmetrically around the ECRH frequency. This set-up guarantees the ECE and ECRH deposition follow the same optical path. Using two dielectric plates and a notch filter, the amplitude of the ECRH radiation, which is reflected or scattered back, is suppressed by 125 dB. Therefore by placing the ECE channels symmetrically around a magnetic island, the ECRH power is deposited on the magnetic island. The angle of the launcher mirror controls the ECE measurement and ECRH deposition position simultaneously.

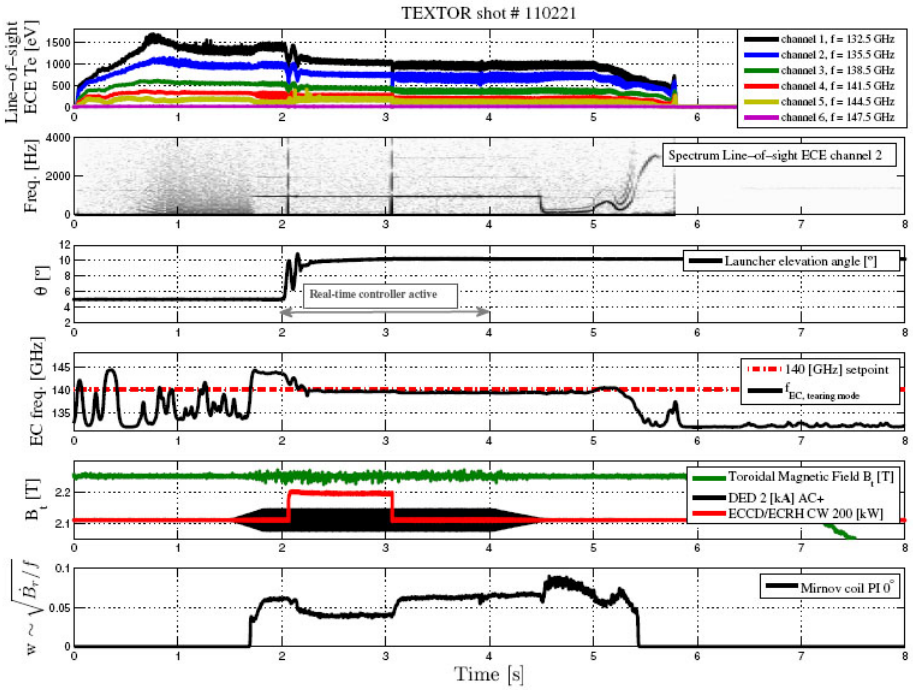

Figure B.4.: *Real-time control of the EC launcher angle based on ECE measurements. When the real-time control is started, the launcher moves in such a way to make the EC frequency of the island O-point match with the gyrotron frequency of 140 GHz. The mirnov coils show that the island width decreases as a result of the ECCD/ECRH radiation. Picture from Hennen et. al.*[9]

After initial tests in which the mirror angle and ECRH power and modulation were varied manually, the system was implemented using a controller.[9] The position of the magnetic island is determined from the anti-phase in temperature oscillations, averaged over a period of 2.56 ms. The frequency of the electron cyclotron emission at the centre of the island is calculated from the correlations and a PID controller changes the launcher angle to ensure the frequency of the ECRH and the magnetic island coincide. Using a phase-locked loop on an ECE channel near the island, the ECRH power is modulated. Using the controller, complete alignment is reached in 160 ms. The controller is able to track the magnetic island when the plasma position is varied. The slowest element of the set-up is the launcher mirror, which can be moved from -30° to +30° in 100 ms, and apart from the feedback by the controller also requires an additional, feed-forward, input to compensate for friction. Figure B.4 shows that, using real-time control, the EC launcher is correctly aimed at the NTM.

Bibliography

[1] BP Global. BP Energy Outlook 2030, January 2011.

[2] J D Lawson. Some Criteria for a Power Producing Thermonuclear Reactor. *Proceedings of the Physical Society. Section B*, 70(1):6, 1957.

[3] G. McCracken and P. Stott. *Fusion, The Energy of the Universe*. Elsevier Academic Press, Burlington, Massachusetts, 2005.

[4] R. J. La Haye. Neoclassical tearing modes and their control. *Physics of Plasmas*, 13(5):055501, 2006.

[5] O Sauter, M A Henderson, G Ramponi, H Zohm, and C Zucca. On the requirements to control neoclassical tearing modes in burning plasmas. *Plasma Physics and Controlled Fusion*, 52(2):025002, 2010.

[6] A. Isayama, G. Matsunaga, T. Kobayashi, S. Moriyama, N. Oyama, Y. Sakamoto, T. Suzuki, H. Urano, N. Hayashi, Y. Kamada, T. Ozeki, Y. Hirano, L. Urso, H. Zohm, M. Maraschek, J. Hobirk, K. Nagasaki, and the JT-60 team. Neoclassical tearing mode control using electron cyclotron current drive and magnetic island evolution in jt-60u. *Nuclear Fusion*, 49(5):055006, 2009.

[7] S Cirant, J Berrino, F Gandini, G Granucci, F Iannone, E Lazzaro, G D'Antona, D Farina, K Koppenburg, S Nowak, and G Ramponi. Crucial issues of multi-beam feed-back control with ech/eccd in fusion plasmas. *Journal of Physics: Conference Series*, 25(1):223, 2005.

[8] F. A. G. Volpe, M. E. Austin, R. J. La Haye, J. Lohr, R. Prater, E. J. Strait, and A. S. Welander. Advanced techniques for neoclassical tearing mode control in DIII-D. *Physics of Plasmas*, 16(10):102502, 2009.

[9] B A Hennen, E Westerhof, P W J M Nuij, J W Oosterbeek, M R de Baar, W A Bongers, A Bürger, D J Thoen, M Steinbuch, and the TEXTOR Team. Real-time control of tearing modes using a line-of-sight electron cyclotron emission diagnostic. *Plasma Physics and Controlled Fusion*, 52(10):104006, 2010.

[10] INTERNATIONAL ATOMIC ENERGY AGENCY. ITER-FEAT OUTLINE DESIGN REPORT. Vienna, March 2001.

[11] J. Wesson. *Tokamaks*. CLARENDON PRESS - OXFORD, Third edition, 2004.

[12] O. Sauter, R. J. La Haye, Z. Chang, D. A. Gates, Y. Kamada, H. Zohm, A. Bondeson, D. Boucher, J. D. Callen, M. S. Chu, T. A. Gianakon, O. Gruber, R. W. Harvey, C. C. Hegna, L. L. Lao, D. A. Monticello, F. Perkins, A. Pletzer, A. H. Reiman, M. Rosenbluth, E. J. Strait, T. S. Taylor, A. D. Turnbull, F. Waelbroeck, J. C. Wesley, H. R. Wilson, and R. Yoshino. Beta limits in long-pulse tokamak discharges. *Physics of Plasmas*, 4(5):1654–1664, 1997.

[13] I.G.J. Classen. *Imaging and Control of Magnetic Islands in Tokamaks*. PhD thesis, Eindhoven University of Technology, 2007.

[14] J.W. Oosterbeek. *Towards a self-aiming microwave antenna to stabilise fusion plasmas*. PhD thesis, Eindhoven University of Technology, 2009.

[15] J P Meskat, H Zohm, G Gantenbein, S Günter, M Maraschek, W Suttrop, Q Yu, and ASDEX Upgrade Team. Analysis of the structure of neoclassical tearing modes in ASDEX Upgrade. *Plasma Physics and Controlled Fusion*, 43(10):1325, 2001.

[16] V.S. Udintsev, B.Ph. van Milligen, F.C. Schüller, A. Krämer-Flecken, A.J.H. Donné, J.C. van Gorkom, C.W. Domier, and the TEXTOR-team. Plasma transport properties in the presence of MHD modes studied by ECE at TEXTOR. *Nuclear Fusion*, 43(11):1424, 2003.

[17] L. Urso, H. Zohm, A. Isayama, M. Maraschek, E. Poli, ASDEX Upgrade Team, and JT-60 Team. ASDEX Upgrade-JT-60U comparison and ECRH power requirements for NTM stabilization in ITER. *Nuclear Fusion*, 50(2):025010, 2010.

[18] D De Lazzari and E Westerhof. The role of asymmetries in the growth and suppression of neoclassical tearing modes. *Plasma Physics and Controlled Fusion*, 53(3):035020, 2011.

[19] I.H. Hutchinson. *Principles of Plasma Diagnostics*. Cambridge University Press, Cambridge, United Kingdom, second edition, 2002.

[20] H J Hartfuss, T Geist, and M Hirsch. Heterodyne methods in millimetre wave plasma diagnostics with applications to ece, interferometry and reflectometry. *Plasma Physics and Controlled Fusion*, 39(11):1693, 1997.

[21] M. Shimada, D.J. Campbell, V. Mukhovatov, M. Fujiwara, N. Kirneva, K. Lackner, M. Nagami, V.D. Pustovitov, N. Uckan, J. Wesley, N. Asakura, A.E. Costley, A.J.H. Donné, E.J. Doyle, A. Fasoli, C. Gormezano, Y. Gribov, O. Gruber, T.C. Hender, W. Houlberg, S. Ide, Y. Kamada, A. Leonard, B. Lipschultz, A. Loarte, K. Miyamoto, V. Mukhovatov, T.H. Osborne, A. Polevoi, and A.C.C. Sips. Chapter 1: Overview and summary. *Nuclear Fusion*, 47(6):S1, 2007.

[22] ITER Organisation. Project Integration Document (ITER_D_2234RH) Version 3.0, January 2007.

[23] M.A. Henderson, R. Heidinger, D. Strauss, R. Bertizzolo, A. Bruschi, R. Chavan, E. Ciattaglia, S. Cirant, A. Collazos, I. Danilov, F. Dolizy, J. Duron, D. Farina, U. Fischer, G. Gantenbein, G. Hailfinger, W. Kasparek, K. Kleefeldt, J.-D. Landis, A. Meier, A. Moro, P. Platania, B. Plaum, E. Poli, G. Ramponi, G. Saibene, F. Sanchez, O. Sauter, A. Serikov, H. Shidara, C. Sozzi, P. Spaeh, V.S. Udintsev, H. Zohm, and C. Zucca. Overview of the iter ec upper launcher. *Nuclear Fusion*, 48(5):054013, 2008.

[24] M.E. Austin, P.E. Phillips, W.L. Rowan, J. beno, H-P. Liu, A. Ouroua, R.F. Ellis, R.W. Harvey, A.E. Hubbard, G. Taylor and D.W. Johnson. ITER ECE: Plans and Challenges. In *EC-15 Joint workshop on ECE and ECRH*, page P2.170, 2008.

[25] Manfred Thumm. MW gyrotron development for fusion plasma applications. *Plasma Physics and Controlled Fusion*, 45(12A):A143, 2003.

[26] J.-D. Landis et al. Manufacturing of steering mechanism - 1st prototype. MM18, CRPP - EPFL, Lausanne, Switserland, November 2009. Internal Report.

[27] A. Collazos, R. Bertizzolo, R. Chavan, F. Dolizy, F. Felici, T.P. Goodman, M.A. Henderson, J.-D. Landis, and F. Sanchez. Progress on the iter h&cd ec upper launcher steering-mirror control system. *Plasma Science, IEEE Transactions on*, 38(3):441 –447, 2010.

[28] M. E. Austin, 2011. Personal correspondence.

[29] B.A. Hennen, E. Westerhof, P.W.J.M. Nuij, M.R. de Baar and M. Steinbuch. Systematic design of a tearing mode controller for TEXTOR, submitted to Nuclear Fusion special issue on control of burning plasmas. Submitted to: *Nuclear Fusion (special issue on control of burning plasmas)*.

[30] M. Reich, K. Behler, L. Giannone, A. Mlynek, J. Stober, W. Treutterer and ASDEX Upgrade team. ECCD-based NTM control using the ASDEX Upgrade real-time system. In *37th EPS Conference on Plasma Physics*, page P2.189, 2010.

[31] L.L. Lao, H. St. John, R.D. Stambaugh, A.G. Kellman, and W. Pfeiffer. Reconstruction of current profile parameters and plasma shapes in tokamaks. *Nuclear Fusion*, 25(11):1611, 1985.

[32] L.L. Lao, J.R. Ferron, R.J. Groebner, W. Howl, H. St. John, E.J. Strait, and T.S. Taylor. Equilibrium analysis of current profiles in tokamaks. *Nuclear Fusion*, 30(6):1035, 1990.

[33] A. Manini and J. Berrino and S. Cirant and G. D'Antona and F. Gandini and G. Grünwald and F. Leuterer and M. Maraschek and F. Monaco and G. Neu and G. Raupp and D. Sormani and J. Stober and W. Suttrop and W. Treutterer and D. Wagner and H. Zohm. Development of a feedback system to control mhd instabilities in asdex upgrade. *Fusion Engineering and Design*, 82(5-14):995 – 1001, 2007. Proceedings of the 24th Symposium on Fusion Technology - SOFT-24.

[34] W. A. Bongers, A. P. H. Goede, E. Westerhof, J. W. Oosterbeek, N. J. Doelman, F. C. Schuller, M. R. De Baar, W. Kasparek, W. Wubie, D. Wagner, J. Stober, and TEXTOR Team. MAGNETIC ISLAND LOCALIZATION FOR NTM CONTROL BY ECE VIEWED ALONG THE SAME OPTICAL PATH OF THE ECCD BEAM. *FUSION SCIENCE AND TECHNOLOGY*, 55(2):188–203, FEB 2009.

[35] R.M.J. Sillen, M.A.F. Allaart, W.J. Goedheer and A. Kattenberg. NOTEC: A CODE TO SIMULATE ELECTRON CYCLOTRON EMISSION SPECTRA OF PLASMAS WHICH INCLUDE NON-THERMAL POPULATIONS. Rijnhuizen Report 86-165, FOM-INSTITUUT VOOR PLASMAFYSICA, Nieuwegein, The Netherlands, 1987.

[36] D. B. Batchelor, R. C. Goldfinger, and H. Weitzner. Ray tracing near the electron cyclotron frequency with application to ebt. *Plasma Science, IEEE Transactions on*, 8(2):78 –89, june 1980.

[37] E. Westerhof. IMPLEMENTATION OF TORAY AT JET. Rijnhuizen Report 89-183, FOM-INSTITUUT VOOR PLASMAFYSICA, Nieuwegein, The Netherlands, 1989.

[38] E. Westerhof, A.G. Peeters and W.L. Schippers. RELAX: A COMPUTER CODE FOR THE STUDY OF COLLISIONAL AND WAVE DRIVEN RELAXATION OF THE ELECTRON DISTRIBUTION FUNCTION IN TOROIDAL GEOMETRY. Rijnhuizen Report 92-211, FOM-INSTITUUT VOOR PLASMAFYSICA, Nieuwegein, The Netherlands, 1992.

[39] Dimitri van Heesch. Doxygen, October 2011. `http://www.doxygen.org`.

[40] M. Bornatici, R. Cano, O. De Barbieri, and F. Engelmann. Electron cyclotron emission and absorption in fusion plasmas. *Nuclear Fusion*, 23(9):1153, 1983.

[41] M Sato, N Isei, S Ishida, and A Isayama. Effects of relativistic frequency down-shift and optical thickness on measurements of electron temperature profile from electron cyclotron emission in medium temperature tokamak plasmas. *JOURNAL OF THE PHYSICAL SOCIETY OF JAPAN*, 67(9):3090–3099, SEP 1998.

[42] L. Urso. *Modelling and experiments on NTM stabilisation at ASDEX Upgrade*. PhD thesis, Ludwig-Maximilians-Universität München, 2009.

[43] R. Prater. Heating and current drive by electron cyclotron waves. *Physics of Plasmas*, 11(5):2349–2376, 2004.

[44] M. Maraschek, G. Gantenbein, Q. Yu, H. Zohm, S. Günter, F. Leuterer, and A. Manini. Enhancement of the Stabilization Efficiency of a Neoclassical Magnetic Island by Modulated Electron Cyclotron Current Drive in the ASDEX Upgrade Tokamak. *Phys. Rev. Lett.*, 98(2):025005, Jan 2007.

[45] C. C. Hegna and J. D. Callen. On the stabilization of neoclassical magnetohydrodynamic tearing modes using localized current drive or heating. *Physics of Plasmas*, 4(8):2940–2946, 1997.

[46] R.J. La Haye, R. Prater, R.J. Buttery, N. Hayashi, A. Isayama, M.E. Maraschek, L. Urso, and H. Zohm. Cross-machine benchmarking for ITER of neoclassical tearing mode stabilization by electron cyclotron current drive. *Nuclear Fusion*, 46(4):451, 2006.

[47] M.F.F. Nave and J.A. Wesson. Mode locking in tokamaks. *Nuclear Fusion*, 30(12):2575, 1990.

[48] P. H. Rutherford. Nonlinear growth of the tearing mode. *Physics of Fluids*, 16(11):1903–1908, 1973.

[49] D. De Lazzari and E. Westerhof. On the merits of heating and current drive for tearing mode stabilization. *Nuclear Fusion*, 49(7):075002, 2009.

[50] D. De Lazzari and E. Westerhof. On the merits of heating and current drive for tearing mode stabilization. *Nuclear Fusion*, 50(7):079801, 2010.

[51] N. Bertelli, D. De Lazzari, and E. Westerhof. Requirements on localized current drive for the suppression of neoclassical tearing modes. *Nuclear Fusion*, 51(10):103007, 2011.

[52] Richard Fitzpatrick. Helical temperature perturbations associated with tearing modes in tokamak plasmas. *Physics of Plasmas*, 2(3):825–838, 1995.

[53] F. L. Waelbroeck, J. W. Connor, and H. R. Wilson. Finite larmor-radius theory of magnetic island evolution. *Phys. Rev. Lett.*, 87(21):215003, Nov 2001.

[54] H. R. Wilson, J. W. Connor, R. J. Hastie, and C. C. Hegna. Threshold for neoclassical magnetic islands in a low collision frequency tokamak. *Physics of Plasmas*, 3(1):248–265, 1996.

[55] B. Ayten, 2011. Private Communication.

[56] A. H. Glasser, J. M. Greene, and J. L. Johnson. Resistive instabilities in a tokamak. *Physics of Fluids*, 19(4):567–574, 1976.

[57] E. Westerhof. Tearing mode stabilization by local current density perturbations. *Nuclear Fusion*, 30(6):1143, 1990.

[58] R.J. La Haye, J.R. Ferron, D.A. Humphreys, T.C. Luce, C.C. Petty, R. Prater, E.J. Strait, and A.S. Welander. Requirements for alignment of electron cyclotron current drive for neoclassical tearing mode stabilization in iter. *Nuclear Fusion*, 48(5):054004, 2008.

[59] Z. Chang and J.D. Callen. Global energy confinement degradation due to macroscopic phenomena in tokamaks. *Nuclear Fusion*, 30(2):219, 1990.

[60] T Tala, K Crombé, P C de Vries, J Ferreira, P Mantica, A G Peeters, Y Andrew, R Budny, G Corrigan, A Eriksson, X Garbet, C Giroud, M-D Hua, H Nordman, V Naulin, M F F Nave, V Parail, K Rantamäki, B D Scott, P Strand, G Tardini, A Thyagaraja, J Weiland, K-D Zastrow, and JET-EFDA Contributors. Toroidal and poloidal momentum transport studies in tokamaks. *Plasma Physics and Controlled Fusion*, 49(12B):B291, 2007.

[61] M. Shimada, A. Chudnovskii, A. Costley, K. Ebisawa, G. Federici, N. Fujisawa, Y. Gribov, Y. Igitkhanov, G. Janeschitz, A. Kukushkin, H. Matsumoto, V. Mukhovatov, Y. Murakami, M. Sugihara, G. Vayakis, ITER JCT, and Home Teams. Physics Design of ITER-FEAT. *Journal of Plasma and Fusion Research SERIES*, 3:77–83, 2000.

[62] G. Ramponi, D. Farina, M.A. Henderson, E. Poli, O. Sauter, G. Saibene, H. Zohm, and C. Zucca. Physics analysis of the iter ecw system for optimized performance. *Nuclear Fusion*, 48(5):054012, 2008.

[63] E Poli, AG Peeters, and GV Pereverzev. TORBEAM, a beam tracing code for electron-cyclotron waves in tokamak plasmas. *COMPUTER PHYSICS COMMUNICATIONS*, 136(1-2):90–104, MAY 1 2001.

[64] A.R. Polevoi, S.Y. Medvedev, V.S. Mukhovatov, A.S. Kukushkin, Y. Murakami, M. Shimada, and A.A. Ivanov. ITER Confinement and Stability Modelling. *Journal of Plasma and Fusion Research SERIES*, 5:82–87, 2002.

[65] D. A. Humphreys, J. R. Ferron, R. J. La Haye, T. C. Luce, C. C. Petty, R. Prater, and A. S. Welander. Active control for stabilization of neoclassical tearing modes. *Physics of Plasmas*, 13(5):056113, 2006.

[66] H. van den Brand, M.R. de Baar, N.J. Lopes Cardozo, and E. Westerhof. Integrated modelling of island growth, stabilization and mode locking: consequences for NTM control on ITER. Submitted to: *Plasma Physics and Controlled Fusion*, included in chapter 5 of this thesis.

[67] J. Berrino, E. Lazzaro, S. Cirant, G. D'Antona, F. Gandini, E. Minardi, and G. Granucci. Electron cyclotron emission temperature fluctuations associated with magnetic islands and real-time identification and control system. *Nuclear Fusion*, 45(11):1350, 2005.

[68] R. Prater, D. Farina, Yu. Gribov, R.W. Harvey, A.K. Ram, Y.-R. Lin-Liu, E. Poli, A.P. Smirnov, F. Volpe, E. Westerhof, A. Zvonkov, and the ITPA Steady State Operation Topical Group. Benchmarking of codes for electron cyclotron heating and electron cyclotron current drive under iter conditions. *Nuclear Fusion*, 48(3):035006, 2008.

[69] M. E. Austin. RESOLUTION OF ELECTRON CYCLOTRON EMISSION MEASUREMENTS OF MAGNETOHYDRODYNAMIC MODES IN ITER. *FUSION SCIENCE AND TECHNOLOGY*, 59(4):647–650, MAY 2011. 16th Joint Workshop on Electron Cyclotron Emission and Electron Cyclotron Resonance Heating (EC-16), Inst Plasma Phys Chinese Acad Sci, Sanya, PEOPLES R CHINA, APR 12-15, 2010.

[70] A. Isayama, Y. Kamada, N. Hayashi, T. Suzuki, T. Oikawa, T. Fujita, T. Fukuda, S. Ide, H. Takenaga, K. Ushigusa, T. Ozeki, Y. Ikeda, N. Umeda, H. Yamada, M. Isobe, Y. Narushima, K. Ikeda, S. Sakakibara, K. Yamazaki, K. Nagasaki, and the JT-60 Team. Achievement of high fusion triple product, steady-state sustainment and real-time ntm stabilization in high-β_p elmy h-mode discharges in jt-60u. *Nuclear Fusion*, 43(10):1272, 2003.

[71] A.A. Balakin, M.A. Balakina, and E. Westerhof. Ecrh power deposition from a quasi-optical point of view. *Nuclear Fusion*, 48(6):065003, 2008.

[72] G. Ramponi, D. Farina, M. A. Henderson, E. Poli, G. Saibene, and H. Zohm. ITER ECRH-ECCD system capabilities for extended physics applications. *FUSION SCIENCE AND TECHNOLOGY*, 52(2):193–201, AUG 2007.

[73] N. Bertelli, A.A. Balakin, E. Westerhof, and M.N. Buyanova. Eccd calculations in iter by means of the quasi-optical code. *Nuclear Fusion*, 50(11):115008, 2010.

[74] W. A. Bongers, V. van Beveren, D. J. Thoen, P. J. W. M. Nuij, M. R. de Baar, A. J. H. Donne, E. Westerhof, A. P. H. Goede, B. Krijger, M. A. van den Berg, M. Kantor, M. F. Graswinckel, B. A. Hennen, and F. C. Schuller. Intermediate frequency band digitized high dynamic range radiometer system for plasma diagnostics and real-time tokamak control. *Review of Scientific Instruments*, 82(6):063508, 2011.

[75] D.J. Griffiths. *Introduction to Electrodynamics*. Pearson Benjamin Cummings, San Francisco, California, 2008.

[76] E.V. Appleton. Wireless studies of the ionosphere. *Wireless Section, Institution of Electrical Engineers - Proceedings of the*, 7(21):257 –265, september 1932.

[77] J.A. Bittencourt. *Fundamentals of Plasma Physics*. Springer-Verlag, New York, third edition, 2004.

[78] Ted Strait. ITPA - Topical Group on MHD Stability. Presentation, 16th Workshop on MHD Stability Control, San Diego, United States, November 2011. `https://fusion.gat.com/conferences/mhd11`.

[79] H Zohm, D A Gates, H R Wilson, G Gantenbein, O Gruber, S Günter, M Maraschek, A W Morris, M Sokoll, D Wagner, ASDEX Upgrade Team, and COMPASS-D Team. Neoclassical MHD in ASDEX Upgrade and COMPASS-D. *Plasma Physics and Controlled Fusion*, 39(12B):B237, 1997.

[80] N. K. HICKS, W. SUTTROP, K. BEHLER, L. GIANNONE, A. MANINI, M. MARASCHEK, G. RAUPP, M. REICH, A. C. C. SIPS, J. STOBER, W. TREUTTERER, THE ASDEX UPGRADE TEAM and S. CIRANT. UPGRADES AND REAL TIME NTM CONTROL APPLICATION OF THE ECE RADIOMETER ON ASDEX UPGRADE. In *EC-15 Joint workshop on ECE and ECRH*, page P2.238, 2008.

[81] J.L. Luxon. A design retrospective of the DIII-D tokamak. *Nuclear Fusion*, 42(5):614, 2002.

[82] E. J. Strait, L. Lao, A. G. Kellman, T. H. Osborne, R. Snider, R. D. Stambaugh, and T. S. Taylor. MHD instabilities near the β limit in the doublet III-D tokamak. *Phys. Rev. Lett.*, 62(11):1282–1285, Mar 1989.

[83] D.A. Humphreys, J.R. Ferron, M. Bakhtiari, J.A. Blair, Y. In, G.L. Jackson, H. Jhang, R.D. Johnson, J.S. Kim, R.J. LaHaye, J.A. Leuer, B.G. Penaflor, E. Schuster, M.L. Walker, H. Wang, A.S. Welander, and D.G. Whyte. Development of iter-relevant plasma control solutions at diii-d. *Nuclear Fusion*, 47(8):943, 2007.

[84] S. Ishida and the JT-60 Team. Recent Results and Future Plan on JT-60U. In *19th IEEE/NPSS Symposium on Fusion Engineering (SOFE)*, 2002.

[85] O Neubauer, G Czymek, B Giesen, PW Huttemann, M Sauer, W Schalt, and J Schruff. Design features of the Tokamak TEXTOR. *FUSION SCIENCE AND TECHNOLOGY*, 47(2):76–86, FEB 2005.

[86] KH Finken, SS Abdullaev, MFM De Bock, B Giesen, M Von Hellermann, GMD Hogeweij, M Jakubowski, R Jaspers, M Kobayashi, HR Koslowski, M Lehnen, G Matsunaga, O Neubauer, A Pospieszczyk, U Samm, B Schweer, and R Wolf. Background and initial experiments with the dynamic ergodic divertor on TEXTOR. *FUSION SCIENCE AND TECHNOLOGY*, 47(2):87–96, FEB 2005.

[87] M. de Bock. *Understanding and controlling plasma rotation in tokamaks*. PhD thesis, Eindhoven University of Technology, 2007.

[88] J. W. Oosterbeek, A. Bürger, E. Westerhof, M. R. de Baar, M. A. van den Berg, W. A. Bongers, M. F. Graswinckel, B. A. Hennen, O. G. Kruijt, J. Thoen, R. Heidinger, S. B. Korsholm, F. Leipold, and S. K. Nielsen. A line-of-sight electron cyclotron emission receiver for electron cyclotron resonance heating feedback control of tearing modes. *Review of Scientific Instruments*, 79(9):093503, 2008.